2012

Los Alamos Space Weather Summer School
Research Reports

Josef Koller, J. Russell Terry, Robin D. Gurule *(Editors)*

2012

Los Alamos Space Weather Summer School Research Reports

Josef Koller, J. Russell Terry, Robin D. Gurule *(Editors)*

2012

Los Alamos Space Weather Summer School Research Reports

Preface

The Los Alamos National Laboratory Space Weather Summer School, with support from the Institute of Geophysics and Planetary Physics, the Center for Information Science and Technology, the Laboratory Directed Research and Development office, and the Principle Associate Directorate for Science, Technology, and Engineering, held its inaugural session in the summer of 2011. The summer school returned for a second session, hosting a new class of seven students from various U.S. research institutions from June 4th – July 27th, 2012. The summer school format includes a series of structured didactic lectures as well as mentored research and practicum opportunities. Lecture topics include a range of general and specialized topics in the field of space weather given by a number of active researchers affiliated with LANL.

In addition to structured lectures, students had the opportunity to engage in research projects at the lab through a mentored practicum experience. Each student is paired with a LANL-affiliated mentor to execute a collaborative research project, typically strongly linked with a larger on-going research effort at LANL. This model provides valuable experience and expertise to the student while developing the opportunity for future collaboration.

This report includes a summary of the research efforts fostered and facilitated by the Space Weather Summer School. These reports should be viewed as work-in-progress as the short session again typically only offers sufficient time for preliminary results. At the close of each summer school session, students present a summary of their research efforts, and a panel honors the best presenter with an all-expenses-paid trip to the Fall Meeting of the American Geophysics Union held in San Francisco. This year's winner is Erik Hogan on "Modeling the Expansion of a Contactor Plasma." Congratulations!

This program continues to enjoy success through career development opportunities for students and opportunities for collaboration between students and mentors. Through continued support from a number of laboratory organizations, foremost IGPP, the summer school will continue to be hosted at LANL, and plans are already underway for commencement of a 2013 session to be held this summer.

Los Alamos, NM
January 2013

Dr. Josef Koller
Summer School Director

2012

Los Alamos Space Weather Summer School Research Reports

Students

Ashar Ali	*University of Colorado at Boulder*
Erik A. Hogan	*University of Colorado at Boulder*
Andrew Liang	*University of California at Santa Cruz*
Richard Linares	*University of Buffalo*
Piyush M. Mehta	*University of Kansas*
Quintin Schiller	*University of Colorado at Boulder*
Chao Yue	*University of California, Los Angeles*

Lectures

- Python for Space Science .... *Jon Niehof*
- Statistics for Space Science I: Exploratory Data Analysis .... *Steve Morley*
- Statistics for Space Science II: Inferential Statistics .... *Steve Morley*
- Measurement Techniques in Space Plasma .... *Brian Larsen*
- Adiabatic Particle Motion .... *Mike Henderson*
- Space Debris .... *Mike Shoemaker*
- A Magnetospheric Overview .... *Geoff Reeves*
- Geomagnetic Storms .... *Vania Jordanova*
- IBEX Mission .... *Eberhard Moebius*
- Data Assimilation .... *Humberto Godinez*
- Detecting High Energy Particles .... *John Sullivan*
- Plasma Sheet .... *Sorin Zaharia*
- Substorms .... *Sorin Zaharia*
- Radial Diffusion .... *Weichao Tu*
- Pitch-Angle/Momentum Diffusion .... *Greg Cunningham*
- Space Data and Pitfalls .... *Reiner Friedel*
- Precision Relative Motion Astrodynamics .... *Alan Lovell*
- Plasma Waves .... *Peter Gary*
- Plasma Instabilities .... *Peter Gary*

2012

Los Alamos Space Weather Summer School Research Reports

Pictures

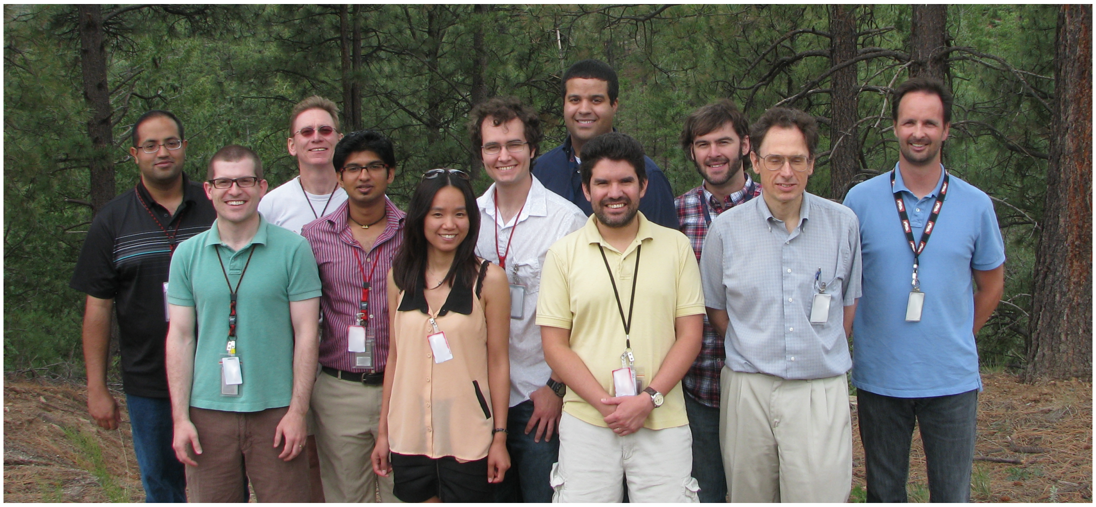

Class of 2012:
(left to right) Ashar Ali, Michael Shoemaker, Reiner Friedel, Piyush M. Mehta, Chao Yue, Eric Hogan, Richard Linares, Humberto Godinez, Quintin Schiller, David Palmer, Josef Koller (not shown Andrew Liang)

LOS ALAMOS
SPACE WEATHER
SUMMER SCHOOL

2012

Los Alamos Space Weather Summer School Research Reports

Sponsors

- Institute of Geophysics and Planetary Physics
- Center for Information Science and Technology
- Laboratory Directed Research and Development

Contact Information

Dr. Josef Koller
Los Alamos Space Weather Summer School
P.O. Box 1663, MS D466
Los Alamos National Lab, NM 87545

http://SpaceWeatherSchool.org

Publication Release

LA-UR 13-23748
ISBN 978-0-9850208-2-8

2012

Los Alamos Space Weather Summer School
Research Reports

Project Reports

Estimating magnetic field power spectrum using CRRES magnetometer data

Ashar Ali

Laboratory for Atmospheric and Space Physics, University of Colorado at Boulder

Reiner Friedel

Space Science and Applications Group, Los Alamos National Laboratory

Scot Elkington

Laboratory for Atmospheric and Space Physics, University of Colorado at Boulder

---

Abstract

We use the magnetic field measurements from the Combined Release and Radiation Effects Satellite (CRRES) to estimate the Pc5 magnetic field power. These power spectra are computed as a function of radial distance L, intensity of the magnetic activity Kp, and magnetic local time. Evidence such as results of hypothesis testing are presented to quantify the relationships between these parameters.

Keywords: radial diffusion, magnetic field PSD, Pc5 waves, CRRES

---

1. Introduction

It is well known that radial diffusion is one of the mechanisms responsible for populating and depleting the van Allen radiation belts with high energy charged particles. Since its initial formulation (Fälthammar, 1965) radial diffusion has been considered important to the study of acceleration mechanisms of charged particles in the geomagnetic environment. The initial formulation has been extended to include for example, drift-resonance interactions between electrons and ULF toroidal (Elkington et al., 1999) and poloidal (Elkington et al., 2003) waves.

Initial estimates of the diffusion coefficients assumed a fixed value of $D_{LL} = D_{LL}^{E} + D_{LL}^{M}$ due to both the electric and magnetic fluctuations. Brautigam and Albert (2000) have shown that in order to model storm time behavior of relativistic electrons it is necessary for the diffusion coefficients to be dependent on Kp. Using CRRES electric field measurement data Brautigam et al. (2005) determined the electric field power spectral densities as a function of L and Kp covering frequencies between 0.2mHz and 15.9mHz. They assume a purely electrostatic field and compute the Kp dependent electrostatic component of the radial diffusion coefficient D_{LL}^{E}. They then conclude that high activity (Kp=6) causes the average value of the coefficients to be one to two orders of magnitudes higher than for low activity (Kp=1). Following the work of Brautigam et al. (2005) we will estimate the magnetic field power spectral density which can then be used to compute the electromagnetic component of the radial diffusion coefficient D_{LL}^{M}. We will then study its dependence on L, Kp, and MLT.

2. Data Collection and Preparation

CRRES mission was launched on July 25, 1990 into a geosynchronous transfer orbit with an inclination of 18°, perigee of 350 km, and apogee of 3600 km. With an orbit of around 9.5 hours, the apogee precessed from near 0600

Email addresses: `ashar.ali@lasp.colorado.edu` (Ashar Ali), `rfriedel@lanl.gov` (Reiner Friedel), `scot.elkington@lasp.colorado.edu` (Scot Elkington)

Los Alamos Space Weather Summer School 2012

MLT through local midnight to around 1330 MLT at a rate of 2.5 minutes per day. CRRES orbit was set up to cover all local times in about 19 months but due to an on board battery failure the mission ended in less than 15 months. This introduces a bias against data from high L-shells on the dayside.

The stabilized spin period was 30 seconds (2 rpm) with the spacecraft spin axis aligned about 9° away from the earth-sun line. There were sophisticated instruments on board to measure both the electric and magnetic field. The fluxgate magnetometer (Singer et al., 1992) was located at the end of a boom and measured the full magnetic field vector every 2.05 seconds. The data provided was spin-fitted and converted from local spacecraft coordinates into a modified GSE coordinate system where the x-axis points along the CRRES spin axis, almost parallel to the x-axis in GSE.

The 30 seconds resolution magnetic field data used for this study starts at orbit 190 on October 11, 1990 and ends on orbit 1062 on October 10, 1991 with orbits 360 to 409 removed. The data was visually inspected for any unusual spikes or missing data. For small gaps the data was interpolated. Few other orbits, with large data gaps or incomplete data were eliminated from this study. In additioon, orbits with low Bz while the apogee was near the noon sector were also eliminated in case there were any magnetopause crossings. After all the clean up, we had considerably more usable data available to us from the CRRES magnetometer than Brautigam et al. (2005) had from the electric field instruments.

3. Fourier Analysis and Binning

Since we cannot compute the diffusion coefficient as a continuous function of L, Kp, and MLT, it is necessary to discretize the parameter space and create bins. The bins were created in a manner similar to what Brautigam et al. (2005) used. The bins in L are centered at $L = 3.0, 3.5, 4.0, 4.5, 5.0, 5.5, 6.0, 6.5, 7.0$. So for example, the bin $L = 5.0$ contains data from $L = 4.75$ to $L = 5.25$. Since we will have poor statistics for $L < 3$ and $L > 9$ as well as off-equatorial effects, we bin the data with $L < 3$ into the $L = 3$ bin and bin $L > 7$ data into the $L = 7$ bin. This then causes statistical confounding so the two extremes bins $L = 3$ and $L = 7$ are later discarded. Along the Kp axis, we bin using

Q = Quiet = {0, 0+, 1-, 1, 1+}
L = Low Activity = {2-, 2, 2+, 3-, 3, 3+}
M = Moderate Activity = {4-, 4, 4+, 5-, 5, 5+}
H = High Activity = {6-, 6, 6+, 7-, 7, 7+}
E = Extreme Activity = {8-, 8, 8+, 9-, 9}

and along the MLT axis, we use MLT = 0, 6, 12, and 18 hours as the bin centers. These additional bins in local time were created because we wish to investigate how the power in the magnetic field changes with respect to local time. Because of this binning in MLT, it was necessary to coarsen the Kp grid. Otherwise we would have very poor statistics in all of the bins. Kp = E bin is also discarded because of the small sample size. Using ephemeris information it was determined that CRRES spends about 20 minutes in each L-bin so we work with running data segments 20 minutes long.

The data is first detrended using a cubic smoothing spline. The cubic smoothing spline depends on a smoothing parameter p which can take any value between zero and one. For $p = 0$ the smoothing spline gives us the ordinary least squares fitted straight line. For $p = 1$ we get the cubic spline with natural boundary conditions which goes through all of the data points. As p varies from zero to one continuously, the smoothing spline becomes a better and better approximation of the data. Setting the smoothing parameter at $p = 0.00125$ the smoothing spline acted essentially as a low pass filter which is then subtracted to remove power from the zero channel.

Then for each 20 minute segment, the power spectral density is estimated using the multi-tapered method using seven discrete prolate spheroidal sequences as data tapers. The PSDs are then binned according the L, Kp, and MLT

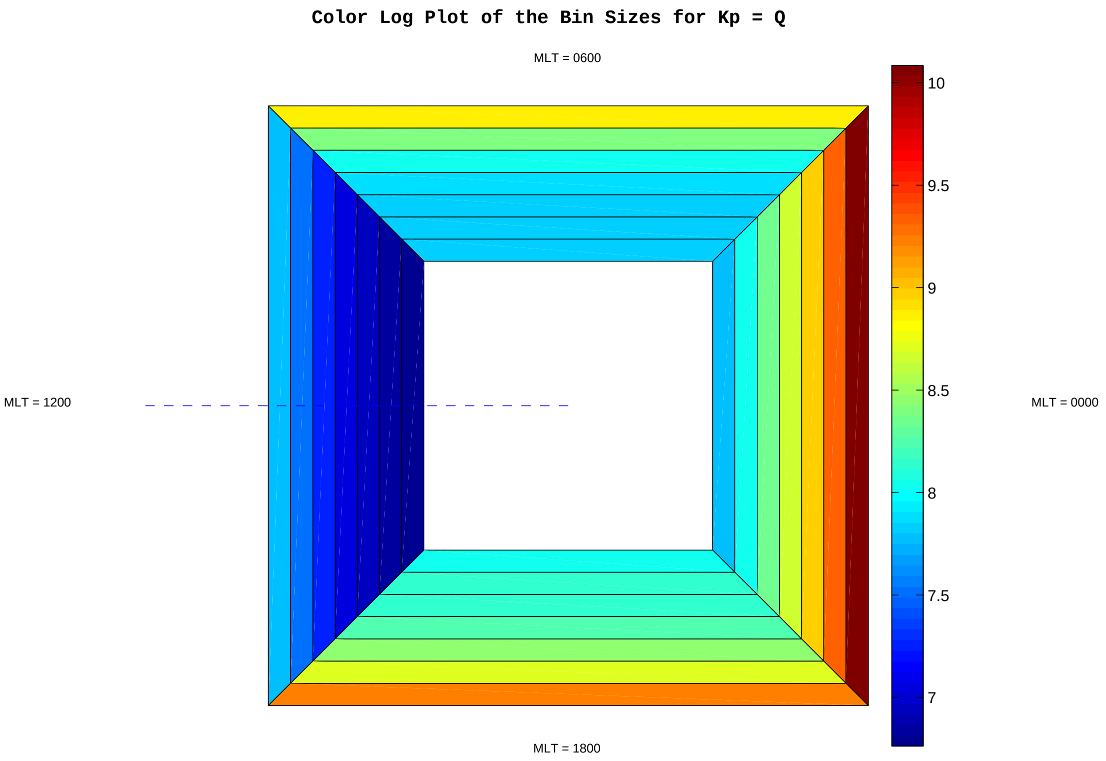

Figure 1: A color log plot summarizing the number of data segments in all of the L and MLT bins if Kp = Q is fixed. The L-bins start at $L = 3.5$ and increase radially outward until $L = 6.5$. Notice the severity of the positive bias at high L-shells around midnight as well as the negative bias around noon.

value at the center of the data segment. After all of the data is binned, we looked at the size of the bins to see how many data segments are in each bin. Almost all of the bins contains thousands of segments while while a few are on the order of hundreds or even tens. $L = 3.5, Kp = H, MLT = 6$ is the only bin which is completely empty. Figure 1 shows a color plot comparing some of the bin sizes.

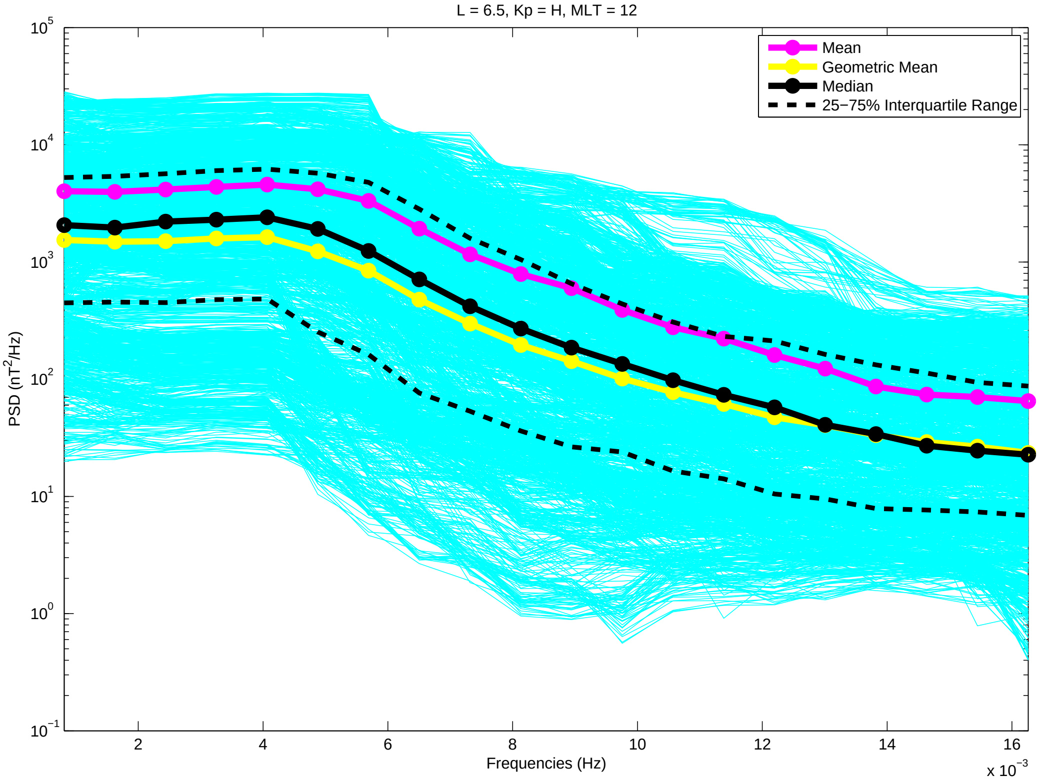

Figure 2: This particular bin contains 2151 data segments all of which are plotted on a log scale along with their arithmetic mean, geometric mean, and median. Since the median is a more robust measure of central tendency, especially in the presence of outliers, median is the most appropriate statistic here as a representative of the data in a bin. The median is plotted here along with 25% − 75% inter-quartile range to give an idea of the spread of the data.

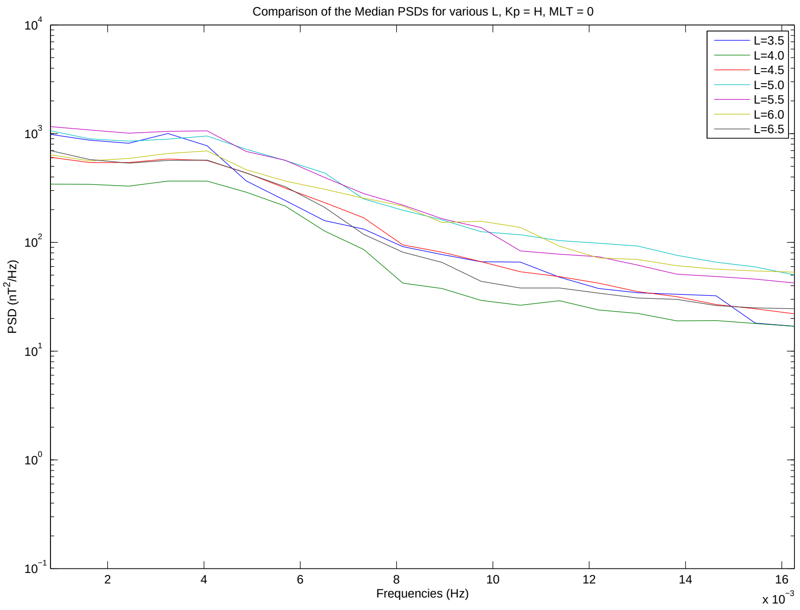

Figure 3: Median PSDs for various L's when $Kp = H$ and $MLT = 0$ are fixed.

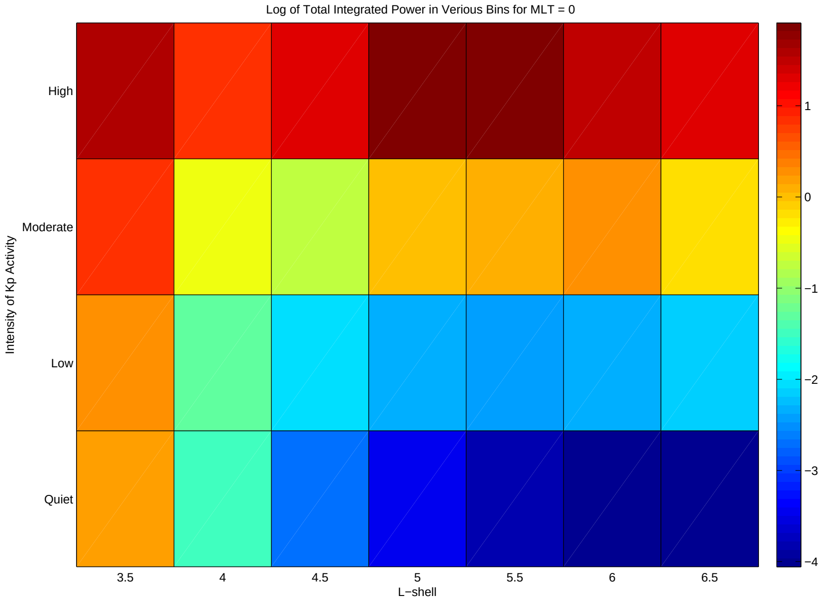

Figure 4: Total power in various bins for $MLT = 0$.

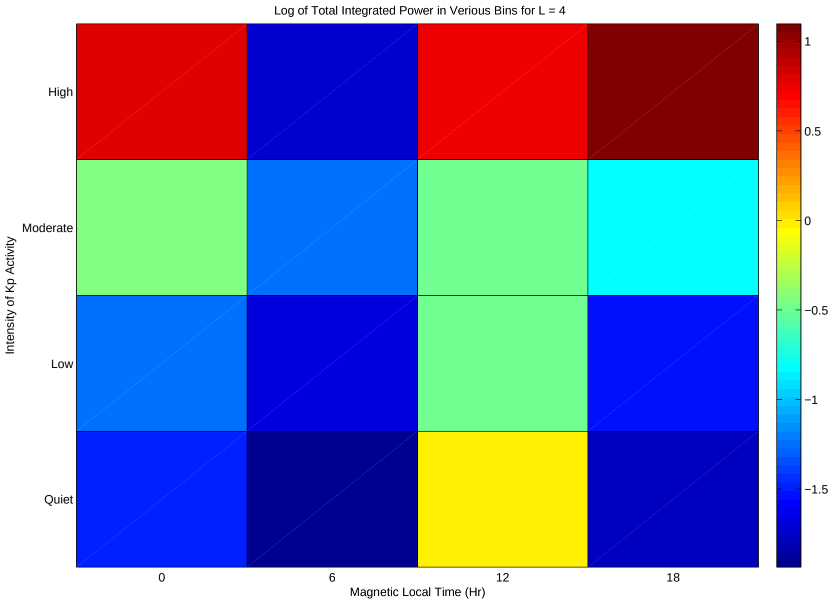

Figure 5: Total power in various bins for $L = 4$.

4. Statistics

After all of the data has been binned, it became necessary to pick a representative data segment from each bin. As figure 2 shows, the median is a robust measure of central tendency when compared with the arithmetic mean or even the geometric mean, especially in the presence of outliers. The mean is very sensitive to outliers and since in our bins outliers may exist a few orders of magnitudes away, the mean is a particularly bad choice for us. Therefore, we pick the median PSD from each bin as a representative of that bin. Figure 3 compares the median PSDs for various L with a high Kp activity at midnight.

In order to determine if the difference in power at various local times is statistically significant, we performed hypothesis testing by applying the (right-tailed) rank sum test comparing bins pairwise in local time. For this comparison, the grid in L and Kp was coarsened to low activity, high activity, inner magnetosphere, and outer magnetosphere. The rank sum test tests the null hypothesis $Median(X) = Median(Y)$ against the alternate hypothesis $Median(X) > Median(Y)$. We use the significance level of $\alpha = 0.05$. The results of all the comparisons are presented in tables 1, 2, 3, and 4.

5. Discussion

We see from figure 1 that we have fewer statistics around noon time than compared with other local times. Figure 2 shows that PSDs from a single bin can vary up to 2-3 orders of magnitude. The power is nearly flat from 0.81 mHz to 4.1 mHz at which there is a very weak maximum peak at which is observed in almost all of the bins. Figure 3 also shows that the power seems to be independent of L. As frequency changes, the ranking of powers at different L also changes as the curves cross each other.

Figures 3 and 3 verify the fact that high Kp activity results in higher power than power at quieter times (Takahashi and Anderson, 1992) but we also see that towards midnight, higher power occurs close to $L = 5, 5.5$. They also show that at $L = 4$ power is at maximum on the dusk side. The results of the statistical comparison let us decide if such differences are significant or not. They provide us with a quantification as well as a concise summary of all of the comparisons. From tables 1 and 2, we see that during quiet times the only thing we can say for sure is that noon has higher power than at other times. For the outer magnetosphere we also have additional weak evidence that there is more power at dusk than dawn. From tables 3 and 4 we see that during high activity the dominance of power at noon is not so clear anymore. At low L-shell values noon and midnight both have higher powers than at dawn-side. At higher L-shells all three sectors have more power than dawn-side. For all other comparisons we don't have enough statistical evidence to conclude anything.

We are primarily concerned with Pc5 waves and (Takahashi and Ukhorskiy, 2007) has shown that they have a strong dependence on solar wind. Hence solar wind velocity is another parameter which should be explored but during the lifetime of the CRRES mission, the only data available is from IMP 8 which has a resolution too low to be of any use to us. As demonstrated (partially due to incomplete observations) there are quite a few uncertainties which impede us. The interquartile range is intended to give an example of how varied the power (and hence the diffusion coefficients themselves) can be. But despite the fact that we have only single point measurements we have established some facts with strong evidence for them. Clearly, more investigation is needed to explore this parameter space and comprehend the individual acceleration mechanisms as well as their interactions with each other.

6. Acknowledgment

We would like to acknowledge the Virtual Magnetospheric Observatory, Institute of Geophysics and Planetary Physics, University of California, Los Angeles for providing access to the data used in this study. In addition, we would like to thank our colleagues at Space Science and Applications Group, part of Los Alamos National Laboratory for providing us with invaluable assistance along with stimulating discussions in the course of this study. Partial funding was provided by the Los Alamos Space Weather Summer School 2012.

References

Brautigam and Albert (2000), "Radial diffusion analysis of outer radiation belt electrons during October 9, 1990 magnetic storm", J. Geophys. Res., 105, 291-309.

Brautigam et al. (2005), "CRRES electric field power spectra and radial diffusion coefficients", J. Geophys. Res., 110, A02214.

Elkington, Hudson, and Chan (1999), "Acceleration of relativistic electrons via drif-resonance interaction with toroidal-mode PC-5 ULF oscillation", Geophys. Res. Lett., 26, 3273-3276.

Elkington, Hudson, and Chan (2003), "Resonant acceleration and diffusion of outer zone electrons in an asymmetric geomagnetic field", J. Geophys. Res., 108(A3), 1116.

Fälthammar (1965), "Effects of time-dependent electric fields on geomagnetically trapped radiation", J. Geophys. Res., 70, 2503-2516.

Singer, Sullivan, Anderson, Mozer, Harvey, and Wygant (1992), "Fluxgate magnetometer instrument on CRRES", J. Spacecr. Rockets, 29, 599-601.

Takahashi and Anderson (1992), "Distribution of ULF enerfy (f is less than 80 mHz) in the inner magnetosphere: A statistical analysis of AMPTE CCE magnetic field data", J. Geophys. Res., 97, 10751-10773.

Takahashi and Ukhorskiy (2007), "Solar wind control of Pc5 pulsation power at geosynchronous orbit", J. Geophys. Res., 112, A11205.

		MLT - Y			
		0	6	12	18
MLT - X	0	-	0.4947	0.9988	0.3590
	6	0.5160	-	0.9993	0.3792
	12	0.0013	0.008	-	0.0015
	18	0.6510	0.6310	0.9987	-

Table 1: Low Kp activity in the inner magnetosphere

		MLT - Y			
		0	6	12	18
MLT - X	0	-	0.2225	0.9812	0.8156
	6	0.7855	-	0.9987	0.9619
	12	0.0201	0.0015	-	0.0230
	18	0.1917	0.0405	0.9785	-

Table 2: Low Kp activity in the outer magnetosphere

		MLT - Y			
		0	6	12	18
MLT - X	0	-	0.0028	0.3894	0.1157
	6	0.9974	-	0.9923	0.9214
	12	0.6208	0.0084	-	0.2068
	18	0.8895	0.0827	0.8008	-

Table 3: High Kp activity in the inner magnetosphere

		MLT - Y			
		0	6	12	18
MLT - X	0	-	0.0019	0.7266	0.8733
	6	0.9982	-	0.9987	0.9998
	12	0.2824	0.0015	-	0.7527
	18	0.1324	0.0002	0.2558	-

Table 4: High Kp activity in the outer magnetosphere

Modeling the Expansion of a Contactor Plasma

Erik A. Hogan

University of Colorado at Boulder, Boulder, CO 80309

Gian Luca Delzanno

Los Alamos National Laboratory, Los Alamos, NM

Abstract

Plasma contactor technology is widely used on board spacecraft to keep spacecraft charging levels under control. On the International Space Station, for instance, it is used to prevent high current discharges between differently charged surfaces. It consists of emitting a neutral plasma to create a plasma reservoir near the spacecraft in order to balance the currents collected by the spacecraft from the magnetospheric environment. One approach to modeling the contactor plasma plume applies a self-similar solution in order to gain insight into the plume dynamics without requiring expensive numerical simulations. Typically, hydrodynamic fluid equations are used to model the plasma behavior. In this paper, a comparison of two self-similar plume expansion models is presented. Approximate analytic models are obtained for plasma plume expansion into vacuum.

Keywords: plasma plume modeling, self-similar expansion, contactor plasma

---

1. Introduction

In earth orbit, spacecraft experience several types of natural charging. One type of charging that occurs can be attributed to the presence of a plasma environment around the spacecraft. The interaction between the charged particles in the plasma and conducting surfaces on a spacecraft can result in charging on the order of 10's of kiloVolts. The use of plasma contactor technology is important for spacecraft applications where dangerous charging is an issue. A neutral plasma, often Xenon, is emitted from a spacecraft into the surrounding environment to create a plasma reservoir which is used to balance out the charging from the natural environment. On the international space station (ISS), for instance, a large charge differential may develop between the tips of the solar panels and the hull (Gabdullin et al., 2008). Left unchecked, the charge differential results in a discharge current between the different parts of the ISS. This may be damaging to onboard electronics or dangerous to astronauts on a spacewalk.

In order to study applications of a contactor plasma, a method is needed to model the expansion of the emitted plasma plume into the surrounding environment. One way to accomplish this is through the use of particle-in-cell (PIC) simulations, which provide an accurate first principle description of plasma behavior at the expense of computation time. For a large contactor plasma plume (~1 km), the use of PIC simulations presents serious challenges. For a PIC simulation to be stable and accurate, the simulation domain needs to resolve both the smallest time and length scales of the problem. Typical contactor plumes have a plasma temperature in the 1-5 eV range and an ion injection velocity of a few km/s. With a typical emission of 10^{18} particles per second, the Debye length of the plasma may be on the order of millimeters. For a plasma plume with an overall size on the order of a kilometer, there is a difference in scale of six orders of magnitude. The computational burden for such a scenario is immense, and impossible with typical PIC codes even on today's supercomputers.

To circumvent this problem, analytic solutions for plume expansion are desired. In this paper, two analytic plume models are considered (Korsun, 1995; Merino et al., 2011). Both of them apply the method of self-similarity to plasma

---

Email addresses: `erik.hogan@colorado.edu` (Erik A. Hogan), `delzanno@lanl.gov` (Gian Luca Delzanno)

Los Alamos Space Weather Summer School 2012

fluid equations to arrive at an analytic solution for a plasma plume expanding into a vacuum. While the respective plume models are similar in their solution procedure, slightly different fluid equations are used to model the plasma behavior.

The paper is structured as follows. First, an overview of the fluid equations used to describe the plasma behavior is presented. Next, the self-similar solution procedure in Korsun (1995) is reproduced, resulting in an approximate, analytic plume model. Lastly, the developments in Merino et al. (2011) are reproduced. Three solution treatments are considered, and the corresponding analytic plume models are presented.

2. Background

In this paper, two different plume models are considered. Both models start from the two-fluid equations for a plasma of electrons and ions. The models include a continuity equation for the plasma (quasi-neutrality holds), momentum equations and an equation of state for pressure. The equations are written in cylindrical geometry with azimuthal symmetry and a steady-state solution is sought.

2.1. *Fluid Equations in Korsun (1995)*

The first plume model under consideration is developed in Korsun (1995). Here, a detailed replication of the self-similar plume model is presented. The solution is obtained after consideration of the fluid equations at steady state:

$$\frac{\partial nu}{\partial x} + \frac{1}{r}\frac{\partial(rnv)}{\partial r} = 0 \tag{1a}$$

$$mn\left(u\frac{\partial u}{\partial x} + v\frac{\partial u}{\partial r}\right) = -\frac{\partial nT}{\partial x} \tag{1b}$$

$$mn\left(u\frac{\partial v}{\partial x} + v\frac{\partial v}{\partial r}\right) = -\frac{\partial nT}{\partial r} \tag{1c}$$

$$\frac{n}{\gamma - 1}\left(u\frac{\partial T}{\partial x} + v\frac{\partial T}{\partial r}\right) + nT\left(\frac{\partial u}{\partial x} + \frac{1}{r}\frac{\partial rv}{\partial r}\right) = \nabla \cdot \vec{q}, \tag{1d}$$

where m is the ion mass, $\vec{V} = (u, v)$ is the velocity field, n is the plasma density, T is the plasma temperature, γ is the adiabatic index, and $\vec{q}$ is the heat flux. These fluid equations are expressed in cylindrical coordinates. Here, x is along the axis of the jet and r is the radial direction, normal to the jet axis. The velocity in the x direction is denoted as u, and v is the velocity in the r direction. Axial symmetry of the jet is assumed for this problem.

2.2. *Fluid Equations in Merino et al. (2011)*

The second plume model considered is developed in Merino et al. (2011). The fluid equations used to obtain a self-similar solution are somewhat different than before. Rather than including an equation for temperature, a polytropic equation of state is used. In this case, the set of fluid equations is

$$\frac{\partial nu}{\partial x} + \frac{1}{r}\frac{\partial(rnv)}{\partial r} = 0 \tag{2a}$$

$$u\frac{\partial u}{\partial x} + v\frac{\partial u}{\partial r} + \frac{e}{m_i}\frac{\partial \phi}{\partial x} = 0 \tag{2b}$$

$$u\frac{\partial v}{\partial x} + v\frac{\partial v}{\partial r} + \frac{e}{m_i}\frac{\partial \phi}{\partial r} = 0 \tag{2c}$$

$$\frac{1}{n}\nabla(nT_e) - e\nabla\phi = 0, \tag{2d}$$

where ϕ is the electric potential of the plume and e is the elementary charge. The subscripts e and i refer to electrons and ions, respectively. Equations (2b) and (2c) are the ion momentum equations, while Eq. (2d) stems from the electron momentum equation after neglecting electron inertia.[1] The above set of equations, taken alone, will not yield a solution as there are more unknowns than equations. In order to remedy this issue, the polytropic relation

$$nT_e = T_{e0}\frac{n^\gamma}{n_0^{\gamma-1}} \tag{3}$$

is introduced. In this model, the electron temperature is assumed to be constant throughout the plume ($T_e = T_{e0}$). Combined with the fluid equations above, this relation allows for a self-similar solution for the plume expansion.

3. Self-Similar Solution in Korsun (1995)

Here, we proceed through the solution procedure outlined in Korsun (1995). The streamlines of the plume are assumed to expand according to

$$r(x) = r_0 a(x), \tag{4}$$

where $a(x)$ is a function whose form will be obtained from the self-similar solution procedure. Furthermore, the scaled coordinate

$$\eta = \frac{r}{a(x)} \tag{5}$$

is introduced.

It is assumed that the plume solution will separate as functions of x and η. To obtain a self-similar solution, the self-similar form

$$u = u_c(x)y(\eta) \tag{6a}$$

$$v = u\eta a' \tag{6b}$$

$$T = T_c(x)\tau(\eta) \tag{6c}$$

$$nu = \frac{\dot{N}\lambda}{\pi a^2} f(\eta) \tag{6d}$$

is used. The constants $\dot{N}$ and λ are plume characteristics formally defined as

$$\dot{N} = \int_0^\infty nu2\pi r\mathrm{d}r$$

$$\lambda^{-1} = \int_0^\infty f2\eta\mathrm{d}\eta.$$

Note that $\tau(0) = y(0) = f(0) = 1$. For compactness of notation, $()'$ is used to denote a derivative with respect to the independent variable. For example, $u_c' = \frac{\partial u_c}{\partial x}$.

3.1. Continuity Equation

Korsun (1995) claims that with this self-similar solution form, Eq. (1a) reduces to an identity. The proof follows. First, we compute the following derivatives. Let $nu = \beta(a)f(\eta)$, where $\beta = \frac{\dot{N}\lambda}{\pi a^2}$. Then

$$\frac{\partial nu}{\partial x} = -2f\frac{\beta}{a}a' - \beta\frac{\eta}{a}a'f' \tag{8}$$

and

$$nv = nua'\eta \tag{9a}$$

$$\frac{1}{r}\frac{\partial rnv}{\partial r} = 2f\frac{\beta}{a}a' + \beta\frac{\eta}{a}a'f' \tag{9b}$$

Combining Eqs. (8) and (9b) in the continuity equation clearly reduces to identity.

---

[1] From Eq. (2d) we have $\frac{\nabla(nT_e)}{n} = e\nabla\phi$, which implies that Eqs. (2b) and (2c) are in fact formally equivalent to Eqs. (1b) and (1c).

3.2. Momentum Equation for v (radial component)

We will begin with an analysis of Eq. (1c). Note the following identities

$$\frac{\partial v}{\partial x} = y\eta a' u_c' - u_c \frac{\eta^2}{a} (a')^2 y' - u_c y \frac{\eta}{a} (a')^2 + u_c y \eta a'' \tag{10a}$$

$$\frac{\partial v}{\partial r} = u_c \frac{\eta}{a} a' y' + u_c \frac{y}{a} a' \tag{10b}$$

$$\frac{\partial nT}{\partial r} = T_c \tau n \left(\frac{1}{fa} f' - \frac{1}{ya} y' \right) + n \left(\frac{T_c}{a} \tau' \right). \tag{10c}$$

The above identities are used in Eq. (1c) to yield (after some reduction)

$$m u_c y^2 \eta \left(a' u_c' + u_c a'' \right) = \frac{\tau T_c}{a} \left(\frac{y'}{y} - \frac{f'}{f} - \frac{\tau'}{\tau} \right).$$

The goal here is a separation of variables, where all terms dependent on x are on one side of the equation and those depending on η are on the other. With some minor rearranging this is achieved, resulting in

$$\frac{m a u_c}{T_c} \left(a' u_c' + u_c a'' \right) = \frac{\tau}{y^2 \eta} \left(\frac{y'}{y} - \frac{f'}{f} - \frac{\tau'}{\tau} \right) = C_1, \tag{11}$$

where C_1 is the constant of variable separation. There is one further simplification that may be made, noting that

$$\left(a' u_c' + u_c a'' \right) = \left(u_c a' \right)'.$$

We have thus obtained the same relation as Reference 3, namely

$$\boxed{\frac{m a u_c}{T_c} \left(u_c a' \right)' = C_1.} \tag{12}$$

The right-hand side of Eq. (11) will be left for use later on.

3.3. Momentum Equation for u (axial component)

Here, Eq. (1b) is considered. As before, the following useful identities are defined

$$\frac{\partial u}{\partial x} = y u_c' - u_c \frac{\eta}{a} a' y' \tag{13a}$$

$$\frac{\partial u}{\partial r} = \frac{u_c}{a} y' \tag{13b}$$

$$\frac{\partial nT}{\partial x} = -2 \frac{n T_c \tau}{a} a' + n\tau \left(T_c' - \frac{T_c}{u_c} u_c' \right) + \frac{n \eta \tau}{a} a' \left(\frac{1}{y} y' - \frac{1}{f} f' - \frac{1}{\tau} \tau' \right) \tag{13c}$$

Insertion of the above into Eq. (1b) and performing some minor simplifications yields

$$-2 \frac{T_c}{a^3 u_c} a' + \frac{1}{a^2 u_c} T_c' - \frac{T_c}{a^2 u_c^2} u_c' + \frac{m y^2}{a^2 \tau} u_c' + \frac{T_c \eta}{a^2 u_c} \frac{1}{a} a' \left(\frac{1}{y} y' - \frac{1}{f} f' - \frac{1}{\tau} \tau' \right) = 0.$$

This equation can be simplified further by noting that

$$-2 \frac{T_c}{a^3 u_c} a' + \frac{1}{a^2 u_c} T_c' - \frac{T_c}{a^2 u_c^2} u_c' = \frac{\partial}{\partial x} \left(\frac{T_c}{u_c a^2} \right).$$

With this simplification, the momentum equation for u is

$$\frac{\mathrm{d}}{\mathrm{d}x} \left(\frac{T_c}{u_c a^2} \right) + \frac{m y^2}{a^2 \tau} u_c' + \frac{T_c \eta}{a^3 u_c} a' \left(\frac{1}{y} y' - \frac{1}{f} f' - \frac{1}{\tau} \tau' \right) = 0. \tag{14}$$

Lastly, using Eq. (11) yields

$$\frac{\mathrm{d}}{\mathrm{d}x}\left(\frac{T_c}{u_c a^2}\right) + \frac{my^2}{a^2\tau}u_c' + \frac{T_c}{a^3 u_c}a'\left(\frac{y^2\eta^2}{\tau}C_1\right) = 0. \tag{15}$$

This equation is not separable. However, by imposing an additional constraint on the system, a separable form may be obtained. First, let

$$\frac{\tau}{y^2} = 1 + \psi(\eta), \tag{16}$$

which is convenient because $\tau(0)/y(0) = 1$. Inserting this into the above equation results in

$$\frac{mu_c'}{a^2} + \left(\frac{T_c}{u_c a^2}\right)' = -\left(\frac{T_c}{u_c a^2}\right)'\psi + \frac{a' T_c}{a^3 u_c}(-C_1\eta^2), \tag{17}$$

which can be separated if

$$\boxed{\frac{mu_c'}{a^2} + \left(\frac{T_c}{u_c a^2}\right)' = 0.} \tag{18}$$

By imposing this constraint on the solution, it follows that

$$\frac{\psi}{C_1\eta^2} = -\frac{\frac{a'}{a^3}\frac{T_c}{u_c}}{\left(\frac{T_c}{u_c a^2}\right)'} = \frac{1}{C_2}, \tag{19}$$

where C_2 is a constant of separation. After a few steps of simplification and manipulation, the two relationships

$$\boxed{\frac{\tau}{y^2} = 1 + \frac{C_1}{C_2}\eta^2} \tag{20}$$

and

$$\boxed{\frac{T_c}{T_{c0}} = \frac{u_c}{u_{c0}}\left(\frac{a}{a_0}\right)^{2-C_2}} \tag{21}$$

are obtained. Note that the subscript 0 refers to the values of the corresponding quantities at the origin, e.g. $T_{c0} = T_c(0)$. Now, we return to the right hand side of Eq. (11), rewriting it as

$$\frac{\tau}{y^2\eta}\left(\frac{\partial \ln y}{\partial\eta} - \frac{\partial \ln f}{\partial\eta} - \frac{\partial \ln\tau}{\partial\eta}\right) = C_1$$

Substituting in the relationship for τ/y^2 and separating the variables,

$$d\left(\ln\left(\frac{y}{f\tau}\right)\right) = \frac{C_1\eta}{1 + \frac{C_1}{C_2}\eta^2}d\eta. \tag{22}$$

Integrating and employing Eq. (20) once more yields the relation

$$\boxed{yf = \left(1 + \frac{C_1}{C_2}\eta^2\right)^{-1-C_2/2}} \tag{23}$$

3.4. Temperature Equation

Lastly, Eq. (1d) is considered. Plugging in the self similar solution and simplifying results in

$$\boxed{\frac{\dot{N}\lambda}{\pi a^2}T_c f\tau\frac{\mathrm{d}}{\mathrm{d}x}\left[\ln\left(T_c^{1/(\gamma-1)}u_c a^2\right)\right] = \nabla\cdot\vec{q}.} \tag{24}$$

This equation may be reduced further if the assumption $\nabla q = 0$ is made. For this condition, the above simplifies as

$$T_c^{1/(\gamma-1)} u_c a^2 = \text{const.} \tag{25}$$

Combining this with Eq. (18) results in the condition

$$\frac{m u_c^2}{2} + \frac{\gamma}{\gamma - 1} T_c = \text{const.} \tag{26}$$

.

3.5. Plume Solution

For the three x-dependent variables u_c, T_c, and a four equations result from the self-similar solution procedure:

$$\frac{m a u_c}{T_c} (u_c a')' = C_1 \tag{27a}$$

$$T_c^{1/(\gamma-1)} u_c a^2 = T_0^{1/(\gamma-1)} u_{c0} a_0^2 \tag{27b}$$

$$\frac{T_c}{u_c a^{2-C_2}} = \frac{T_0}{u_{c0} a_0^{2-C_2}} \tag{27c}$$

$$m \frac{u_c^2}{2} + \frac{\gamma}{\gamma - 1} T_c = m \frac{u_{c0}^2}{2} + \frac{\gamma}{\gamma - 1} T_0. \tag{27d}$$

This situation is problematic because the problem is over-determined. The only solution which satisfies all four of these equation simultaneously is the case of constant T_c, u_c, and a. To circumvent this problem, Reference 3 chooses to set $u_c^2 = u_0^2 \left[1 + 2M_0^{-2}(\gamma - 1)^{-1}\right] = \text{const}$ and neglect satisfaction of Eq. (27d). Correspondingly, it is easily shown that $C_2 = 2\gamma$ in order to satisfy Eqs (27b) and (27c). Lastly, the separation constant C_1 is simply chosen as equal to C_2. With these assumptions, the flow parameters are found to evolve along the flow axis as

$$T_c a^{2(\gamma-1)} = T_{c0} a_0^{2(\gamma-1)} \tag{28a}$$

$$m a u_c^2 a'' = 2\gamma T_{c0} \left(\frac{a_0}{a}\right)^{2(\gamma-1)}, \tag{28b}$$

the latter of which may be solved to yield the function $a(x)$.

For the η-dependent terms, we are left with the two equations

$$f y = \left(1 + \eta^2\right)^{-\gamma-1} \tag{29a}$$

$$\frac{\tau}{y^2} = 1 + \eta^2. \tag{29b}$$

Here, as in Reference 3, the case of $\tau = 1$ is chosen, which corresponds to uniform temperature in the flow cross section, i.e. $dT/dr = 0$, is considered. For this condition, note that $y = (1 + \eta^2)^{-1/2}$ and $f = (1 + \eta^2)^{-\gamma}$. Inserting these into the self-similar solution yields

$$n = \frac{\dot{N}(\gamma - 1/2)}{\pi a^2 u_c} \frac{1}{(1 + r^2/a^2)^{\gamma}} \tag{30a}$$

$$u = u_c \frac{1}{(1 + r^2/a^2)^{1/2}} \tag{30b}$$

$$v = u \frac{r}{a} a' \tag{30c}$$

$$T = T_{c0} \left(\frac{a_0}{a}\right)^{2(\gamma-1)}. \tag{30d}$$

Thus, the plume model solution has been obtained.

It is important to point out that this plume solution does **not** satisfy the fluid equations (1a)-(1d). The reason for this lies in the fact that, to obtain a solution, an assumption is made that u_c is constant. Furthermore, the condition in Eq. (27d), required for satisfaction of the u-momentum equation, is ignored. Effectively, this means that Eq. (1b) is not satisfied by the plume solution. An estimate of the error can be obtained by evaluating the momentum equation. While the error will not be zero, it may be small enough that the solution is still a valid approximation of the plasma expansion.

4. Self-Similar Solution in Merino et al. (2011)

Next, we consider the self-similar plume expansion solution derived in Merino et al. (2011). Here, the fluid equations are normalized using T_{e0}, m_i, e, n_0 and a characteristic length R_0. To arrive at the normalized form, note that $\hat{n} = n/n_0$, $\hat{\phi} = e\phi/T_{e0}$, $\hat{u} = u/\sqrt{T_{e0}/m_i}$, and $\hat{v} = v/\sqrt{T_{e0}/m_i}$. Dimensionless variables are denoted with a hat, e.g. $\hat{\phi} = e\phi/T_{e0}$. The self-similar solution is assumed to have the form

$$\hat{u} = u_c(\hat{x})u_t(\eta) \tag{31a}$$

$$\hat{v} = \hat{u}\eta a'(\hat{x}) \tag{31b}$$

$$\hat{n} = n_c(\hat{x})n_t(\eta), \tag{31c}$$

where $\eta = \hat{r}/a$. While appearing in the fluid equations, the electric potential, ϕ, is not explicitly needed to arrive at a solution; it can be obtained by postprocessing the electron momentum equation. The self-similar quantities have the boundary conditions $u_c(0) = \sqrt{\gamma}M_0$, $u_t(0) = 1$, $a(0) = 1$, $n_c(0) = 1$, and $n_t(0) = 1$. Note that M_0 is the flow mach number at the point of plume emission (x=0).

4.1. Continuity Equation

Inserting the self-similar solution into the continuity equation yields

$$2n_c u_c a' + a(u_c n_c' + n_c u_c') = 0, \tag{32}$$

which, after a few steps, reduces to

$$(a^2 n_c u_c)' = 0. \tag{33}$$

Integrating this expression yields

$$\boxed{a^2 n_c u_c = \text{const} = \sqrt{\gamma}M_0.} \tag{34}$$

4.2. Momentum Equation for v (radial component)

Once again, the momentum equation for the radial velocity component is considered first. Normalizing the fluid equations and plugging in the self-similar solution yields

$$\frac{\gamma(n_c n_t)^\gamma n_t'}{n_c n_t^2} + \eta a u_c u_t^2(a' u_c' + u_c a'') = 0. \tag{35}$$

Making note of the minor simplification $(u_c a')' = a'u_c' + u_c a''$, the preceding equation may be separated as

$$\boxed{\frac{u_c a}{n_c^{\gamma-1}}(u_c a')' = -\frac{\gamma n_t^{\gamma-2} n_t'}{\eta u_t^2} = \gamma C,} \tag{36}$$

where C is a constant of separation.

4.3. *Momentum Equation for u*

Next, the momentum equation for u is considered. Again, normalizing and plugging in the self-similar solution yields (after some simplification)

$$\gamma(n_c n_t)^{\gamma-2}(n_t n_c' - \frac{a'}{a}\eta n_c n_t') + u_c u_t^2 u_c' = 0, \tag{37}$$

which is unfortunately not separable. However, if an appropriate assumption is made, then the derivative of Eq. (37) with respect to η is separable. Similar to the developments in Korsun (1995), the solution is assumed to satisfy

$$\gamma n_c^{\gamma-2} n_c' + u_c u_c' = 0. \tag{38}$$

This condition is equivalent to satisfying the momentum equation for u along the center line ($\hat{r} = 0$), and can be integrated to yield

$$\boxed{\frac{1}{2}u_c^2 + \frac{\gamma}{\gamma-1}n_c^{\gamma-1} = \text{const} = \frac{1}{2}\gamma M_0^2 + \frac{\gamma}{\gamma-1}.} \tag{39}$$

Imposing this constraint on the solution and taking the η derivative of Eq. (37), the result ultimately separates as

$$\frac{n_c'}{n_c}\frac{a}{a'} = -\frac{2n_t'}{2n_t u_t'/u_t - (\gamma-1)n_t'} = D. \tag{40}$$

Integrating the left hand side of this equation yields

$$\boxed{n_c = a^D.} \tag{41}$$

Likewise, integrating the η dependent terms results in

$$\boxed{n_t^{2-D(\gamma-1)} = u_t^{-2D}.} \tag{42}$$

4.4. *Electric Potential*

From the self-similar solution procedure, an analytic expression for the normalized density ($\hat{n}$) is obtained. In returning to the fluid equations used to generate a solution, a relationship between $\hat{n}$ and $\hat{\phi}$, the potential, is found. From the electron momentum equation (neglecting electron inertia),

$$\frac{1}{n}\nabla(nT_e) = e\nabla\phi, \tag{43}$$

where T_e is the electron temperature. After normalizing, this equation reduces to

$$\frac{1}{\hat{n}}\nabla\hat{n} = \nabla\hat{\phi}, \tag{44}$$

the solution to which is the Boltzmann relation

$$\hat{n} = \kappa e^{\hat{\phi}}. \tag{45}$$

where κ is a constant of integration. Noting that potential is measured relative to some arbitrary reference, the constant κ is set to 1 without loss of generality, leading to $\hat{n} = e^{\hat{\phi}}$.

4.5. *Plume Solution*

For the $\hat{x}$-dependent terms u_c, n_c and a, four relationships exist:

$$a^2 n_c u_c = \sqrt{\gamma}M_0 \tag{46a}$$

$$\frac{u_c a}{n_c^{\gamma-1}}(u_c a')' = \gamma C \tag{46b}$$

$$\frac{1}{2}u_c^2 + \frac{\gamma}{\gamma-1}n_c^{\gamma-1} = \frac{1}{2}\gamma M_0^2 + \frac{\gamma}{\gamma-1} \tag{46c}$$

$$n_c = a^D. \tag{46d}$$

Again, the over-determined nature of the problem ultimately prevents a full solution from being obtained. Satisfying all four of these conditions simultaneously requires a non-real solution. This problem will be addressed shortly.

For the η-dependent terms n_t and u_t, two relationships result:

$$1)\; n_t^{2-D(\gamma-1)} = u_t^{-2D} \tag{47a}$$

$$2)\; -\frac{\gamma n_t^{\gamma-2} n_t'}{\eta u_t^2} = \gamma C. \tag{47b}$$

In order to arrive at a solution, an assumption for the u velocity component is made. Three different models are considered here; all assume a constant $u_c = \sqrt{\gamma} M_0$. The difference between them lies in how u_t is chosen. By simply choosing a velocity profile for u, the momentum equation for u is ignored. This means the conditions in Eqs. (46c), (46d), and (47a) no longer apply to our solution. The error in the solution may be evaluated using this neglected momentum equation.

First, let us consider the implications of a constant u_c. Immediately, the two remaining conditions for the x dependent terms become

$$n_c = \frac{1}{a^2} \tag{48}$$

and

$$a'' = a^{1-2\gamma} \frac{C}{M_0^2}. \tag{49}$$

It is worth noting the similarities between these developments and those in Korsun (1995). Fundamentally, they are the same, with the differences being attributed to the normalized quantities used here. Next, Eq. (47b) is integrated to yield

$$n_t^{\gamma-1} = 1 - (\gamma-1) C \int \eta u_t^2 \mathrm{d}\eta. \tag{50}$$

Now, two different models are considered. The first is the Parks and Katz (PK) model (Parks and Katz, 1979) . The PK model makes the simple assumption of $u_t = 1$. This merely implies that velocity is constant in a flow cross-section. Plugging this into Eq. (50) yields

$$n_t^{\gamma-1} = 1 - \frac{1}{2}(\gamma-1) C \eta^2. \tag{51}$$

The second model is the Ashkenazy and Fruchtman (AF) model (Ashkenazy and Fruchtman, 2001). Here, a conical velocity profile is assumed, with

$$u_t = \left(1 + (a')^2 \eta^2\right)^{-1/2}. \tag{52}$$

As the plume diverges from the centerline, the velocity is assumed to drop off. Using this velocity profile in Eq. (50) yields

$$n_t^{\gamma-1} = 1 - (\gamma-1) \frac{C}{2(a')^2} \ln\left(1 + (a')^2 \eta^2\right) \tag{53}$$

Once again, it is important to point out that the PK and AF plume models do not satisfy the momentum equation for u, due to the assumptions made about the velocity profile used to gain a solution. The relative local error may be evaluated using

$$\epsilon = \left(\hat{u}\frac{\partial \hat{u}}{\partial \hat{x}} + \hat{v}\frac{\partial \hat{u}}{\partial r} + \gamma \hat{n}^{\gamma-2}\frac{\partial \hat{n}}{\partial \hat{x}}\right) / \hat{u}^2, \tag{54}$$

which is essentially a normalized evaluation of the axial momentum equation. For the assumed constant u_c, this equation reduces to

$$\epsilon = \frac{1}{M_0^2}\left(\frac{n_c'}{n_c} - \eta \frac{a'}{a}\frac{n_t'}{n_t}\right). \tag{55}$$

Being inversely proportional to the flow mach number, this error will be relatively small for actual thruster plumes where M_0 can be greater than 20.

5. Plume Profiles

To illustrate the plume models, density profiles are plotted for the Korsun (1995) and Ashkenazy and Fruchtman (2001) plume models. The Parks and Katz (1979) model is not plotted due to its similarity with the AF model. For the sake of comparison, the density profile in Eq. (30a) is normalized in the same manner used to obtain the AF model density. The adiabatic index is set to $\gamma = 5/3$ for both plume models, and the flow mach number is assumed to be $M_0 = 20$.

To compute the density profile for the AF model, the separation constant C must be defined. It is computed such that 95% of the flow lies within the $\eta = 1$ streamline, which corresponds to a value of $C = 2.64$. The initial slope of the streamline expansion function is defined as $a'(0) = 0.2$. The resulting plume density profile is shown in Figure 1(a). To compute the relative local error, Eq. (55) is used. The error in the AF plume model is shown in Figure 2(a). The worst errors are seen near $x = 0$, in the region outside the plume. There are, however, zero-error streamlines where the axial momentum equation is satisfied.

To compute the density profile for the Korsun model, $a'(0) = 0$ is used. The resulting plume density is shown in Figure 1(b). To compute the relative local error, the axial momentum equation is normalized using the same procedure as Merino et al. (2011). For the Korsun model, the error is computed as

$$\epsilon_K = \left(\hat{u}\frac{\partial \hat{u}}{\partial \hat{x}} + \hat{v}\frac{\partial \hat{u}}{\partial \hat{r}} + \frac{1}{\hat{n}}\frac{\partial \hat{n}\hat{T}}{\partial \hat{x}} \right) / \hat{u}^2. \tag{56}$$

This error is plotted in Figure 2(b). Unlike the AF model, there are no zero-error streamlines in the KT model. Once again, the largest errors occur in the region of $x = 0$.

6. Conclusion

In this paper, a self-similar solution procedure is used to gain an approximate, analytic solution for the expansion of a plasma plume into a vacuum. A detailed reproduction of developments in literature is performed. The first paper considered is Korsun (1995), where a plume solution is derived assuming a separable solution form. Ultimately, an exactly valid analytic solution is unobtainable, with an approximate analytic solution resulting. The second paper considered is that of Merino et al. (2011). Once again, efforts to obtain an analytic solution for the plume expansion are thwarted due to the over-determined nature of the problem. Two different approaches are considered to circumvent the issue and arrive at an approximate solution.

References

Ashkenazy, J., Fruchtman, A., 2001. Plasma plume far field analysis, in: 27th International Electric Propulsion Conference, Fairview Park, OH.

Gabdullin, F.F., Korsun, A., Tverdokhlebova, E.M., 2008. The plasma plume emitted onboard the international space station under the effect of the geomagnetic field. IEEE Transactions on Plasma Science 36, 2207.

Korsun, A., 1995. Transverse expansion of plasma plumes and plasmoids ijected from electric thrusters, in: 24th International Electric Propulsions Conference, Moscow, Russia.

Merino, M., Ahedo, E., Bombardelli, C., Urrutxua, H., Pelaez, J., 2011. Hypersonic plasma plume expansion in space, in: 32nd International Electric Propulsion Conference, Wiesbaden, Germany.

Parks, D., Katz, I., 1979. A preliminary model of ion beam neutralization, in: 14th International Electric Propulsion Conference, Fairview Park, OH.

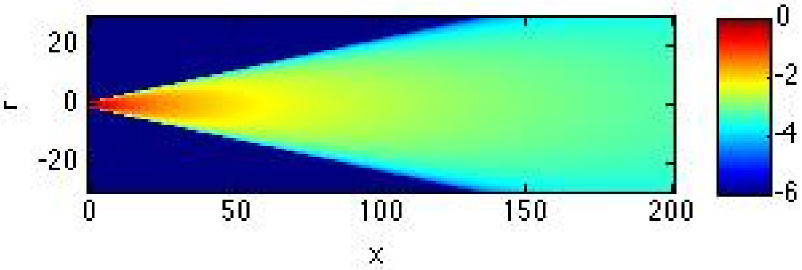

(a) $Log(\hat{n})$- AF Model

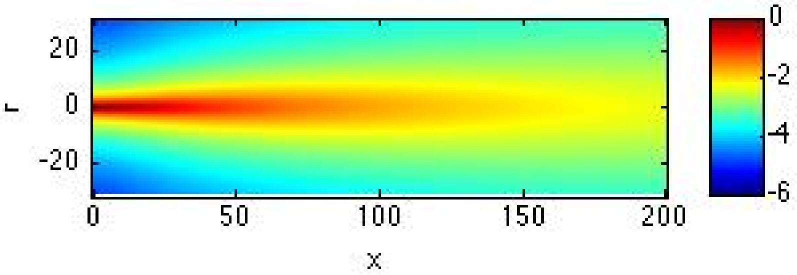

(b) $Log(\hat{n})$- Korsun Model

Figure 1: Density profiles for a) AF model and b) Korsun model

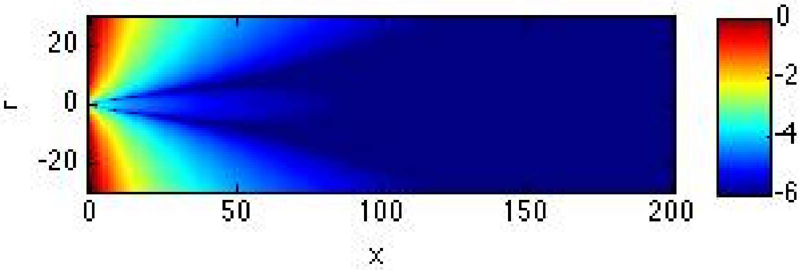

(a) $Log(\epsilon)$- AF Model

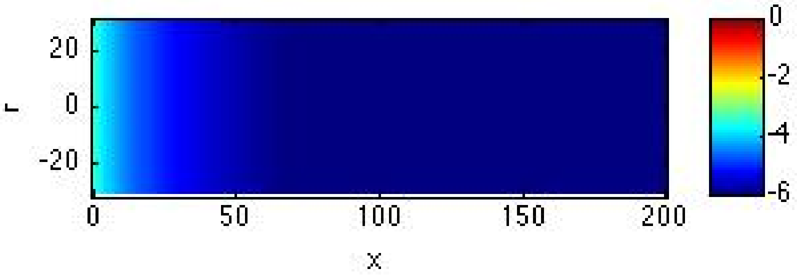

(b) $Log(\epsilon_K)$- Korsun Model

Figure 2: Relative local errors for a) AF model and b) Korsun model

Energy Measurements For A Two Element Detector Using GEANT4 Simulations

Andrew Liang, UCSC
Mentor: Jane Burward-Hoy

Acknowledgements

My deepest gratitude to Los Alamos Space Weather Summer School, especially my Mentor, Jane Burward-Hoy for her kindness and optimism. Eight weeks working in Los Alamos was such an experience that expand my perspective of science, scientists and life.

Abstract

Monte Carlo simulation methods in GEANT4 are used to determine energy measurements and particle identification for a two element detector. Detectors of various thickness and sizes include silicon and YSO materials. Different types of energetic particle sources are incident onto the detectors and the deposited energies are calculated. These simulations are performed under LANL's General Response Simulation System(GRESS). GRESS uses a Monte Carlo simulation to determine the response of an instrument to known photo or particle radiation fields. The system records energy deposits within a given detector and it can apply any desired calibration effects for an instrument design. The GRESS package has several external dependencies: it requires the GEANT4 Monte Carlo simulation toolkit and the ROOT data analysis package, originating from the high energy particle physics simulation toolkit as used by CERN. In addition, the Geometry Description Markup Language (GDML) is used to define the simulation mass models. Our simulation results and post-processing data analysis presented here, will be combined with existing calibrations from energetic particle data from beam labs to determine energetic particle instrument responses for space weather data product delivery.

---

1. Introduction

Since Van Allen's discovery of the radiation belts and many of the subsequent discoveries, particle detection has been fundamental to space science. To provide accurate information about particle distributions, the particle detectors need to be thoroughly calibrated before they are lunched to the space. There are basically two ways for calibrations: experimentally using existing high energy particle beam facilities to radiate onto the particle detectors, from the known particle sources to calibrate the instruments; Using powerful computer simulations to determine the instrument response and compare to the experimental data. For our purpose, we use LANL's in house simulation package - The General Response Simulation System (GRESS). GRESS is based upon GEANT4 code by CERN, developed specially for space science applications and has been successfully implemented for particle instrument calibration. In this project we use GRESS to calibrate a two element detector for space particle energy measurements and particle identification.

2. Methodology

GRESS uses Monte Carlo simulation to determine the response of an instrument to known photon or particle radiation fields. The system records energy deposits within the detector and applies calibration effects to the data. It is designed to provide flexibility in the choice of source position and input energy distribution.

2.1 Simulation Tools

The general architecture of the GRESS code is shown in Figure 1 below. The system is based on a two-step simulation process—one computation-intensive step to generate the ideal physical response of an instrument, and another (faster) step to incorporate non-ideal instrument-specific effects into the response function. Separating these steps allows changing instrumental parameters without regenerating the costly physical response data. Data between these steps is captured in large files using the “root” package from CERN. The standard end products of GRESS are files that contain a spectrum or a detector response matrix. In practical use, a collection of DRMs is required to describe the full instrument response as a function of variables such as angle, position, operating mode, etc. These collections could be used to form a DRM database, which is accessed by auxiliary data analysis systems that require knowledge of the instrument response.

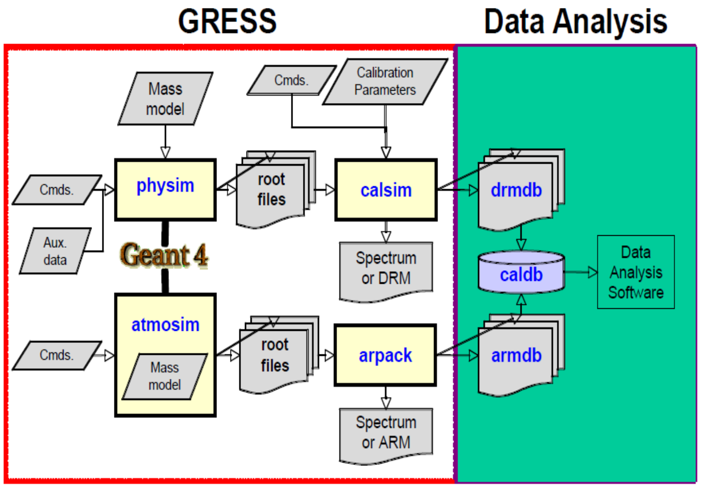

Figure 1- Architecture of the GRESS code.

In our simulations we use program Physim(“physical simulator”). Physim is a program to model and simulate the ideal physical response of arbitrary instruments. It uses the GEANT4 Monte Carlo radiation transport modeling and simulation toolkit with GRESS-specific augmentation. Inputs consist of interactive or stored commands along with could be used to form a DRM database, which is accessed by auxiliary data analysis systems that require knowledge of the instrument response.

2.2 Simulation Setup

The particle detectors simulated is designed into two groups, low energy detectors(LD) and high energy detectors(HD). LD consist of 2 pieces of silicon(Figure 2), each measured 80um and 3500um thick; HD consist of one 300um thick silicon, one YSO crystal with radius of 2.3cm.

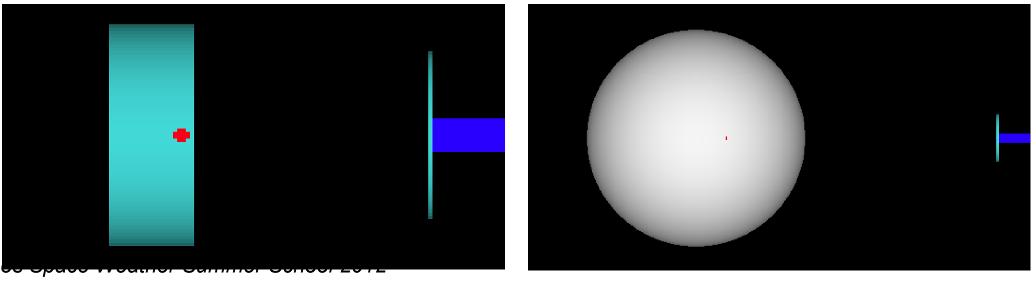

Figure 2. Schematics of low energy detector(left) and high energy detector(right).

LD is designed to measure the stopping power based on the following equation:

$$-dE/dx= (4Z2mec2/\beta\ 2)\bullet C\bullet\rho\bullet[\ln\{2mec2\beta\ 2/(I(1-\beta\ 2))\} -\beta\ 2] \qquad (1)$$

where **mec2** is the electron rest energy, **c** is the speed of light, **β** is ***v*/c**, *v* is the particle speed, **C = πNoe4(*z*/*m*)/(me2c4)**, ***z***, ***m***, **ρ** are the average nuclear charge, nuclear mass and mass density, respectively of the material, and **I** (~13.5*z*eV) is the average ionization potential of electrons in the material.

Dividing both sides of equation (1) by ρ, and substituting the numerical values for **C = 0.150(*z*/*m*) cm2** and **mec2= 0.511 MeV**, gives for the energy loss by ionization expressed in **MeV per g/cm2** units

$$-dE/(\rho dx)= -dE/d\xi=0.307(Z2/\beta\ 2)\bullet(z/m)\bullet[\ln\{2mec2\beta\ 2/(I(1-\beta\ 2))\} -\beta\ 2] \qquad (2)$$

For non-relativistic particles (**β<< 1**) the stopping power for protons (***Z*= 1**) reduces to

$$-dE/d\xi=0.153(mpc2/E)\bullet(z/m)\bullet[11.93 -\ln(z) -\ln(mpc2/E)] \qquad (3)$$

Figure 3 shows a plot of equation (3) for protons traversing Si (z =14) with a curve based on experimental stopping power data.

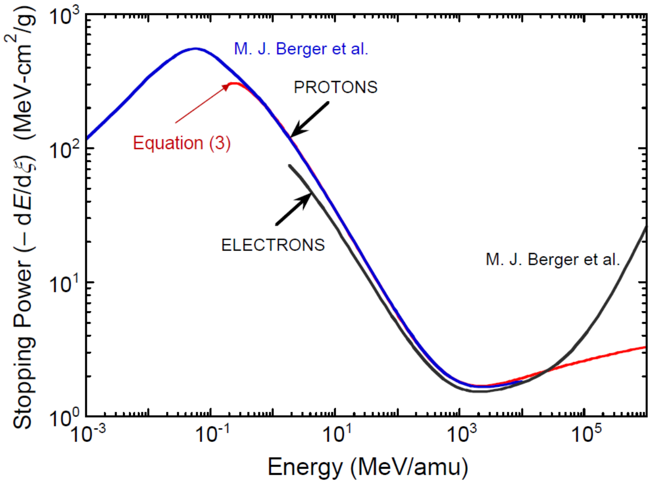

Figure 3 – Proton/Electron Stopping power in Silicon.

HD is a scintillation detector. An energetic particle passing through a *scintillator* material excites atoms that then emit light as they decay to their ground states, the light is then converted to an electrical signal that is amplified and recorded(Figure 4).

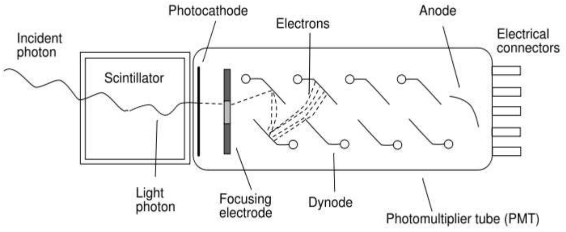

Figure 4 – Schematics of scintillation counter.

The beam input is critical to simulate the instrument response. we can vary the input beam type, energy, shape, size, pointing angle, beam angle to simulate different environments. For this project we are focusing on energy response for proton and electron, so the input beam's shape, size, angles are kept constant while sweep the energy range and particle type as the simulations input. Here is one sample beam input :

```
/gps/particle proton
/gps/pos/shape Circle
/gps/pos/radius 0.05 cm
/gps/ang/type beam2d
/gps/pos/srcdistance 5.0 cm
/gps/pos/srctheta 0. deg
gps/pos/srcphi 0. deg
/gps/ene/mono 100 MeV
```

3. Simulation Results

The energy range a detector can measure is limited by its energy deposition. There is no lower limit as the particle energy will be deposited in the front silicon piece; for upper limit, once the energetic particle “punch through” the back detector materials, the stopping power and scintillation method are no longer valid. Based on the simulation data, energy range for input proton is 10Mev – 150Mev, energy range for input electron is 500Kev to 15Mev. Figure 5 – 8 show the simulations for Proton/electron beam shot onto LD/HD detectors, blue lines are proton trajectory, green lines are generated photons, red lines are electron traces.

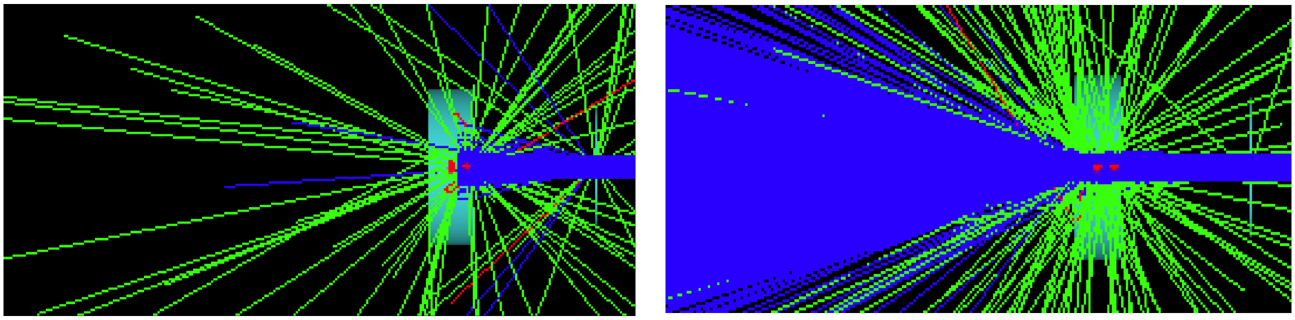

Figure 5 - LD1/LD2 Proton Simulation, left: Proton Parallel 18Mev; right: proton parallel 32Mev.

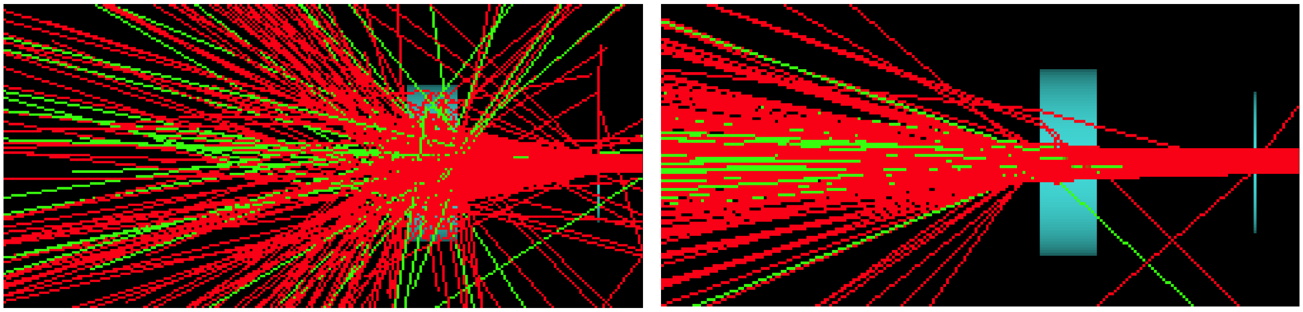

Figure 6 - LD1/LD2 Electron simulation, left: Electron parallel 3 MeV; right: electron parallel 15 MeV.

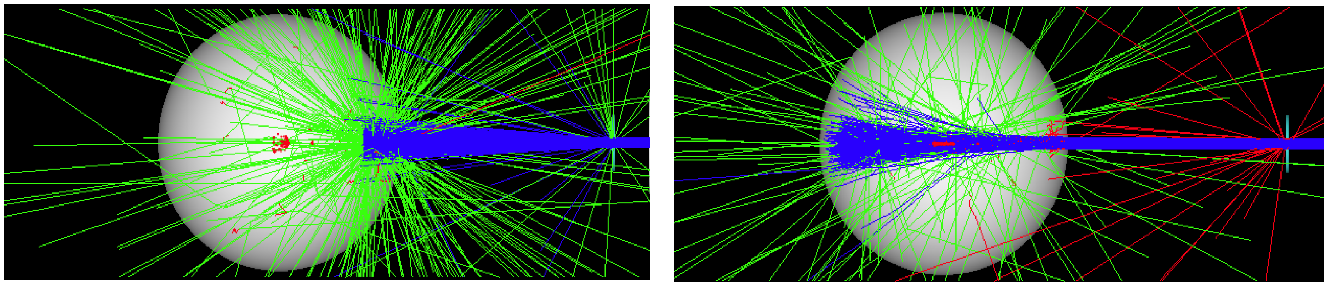

Figure 7 - HD1/HD2 Proton Simulations, left: Proton parallel 40 MeV. Right: Proton parallel 142 MeV.

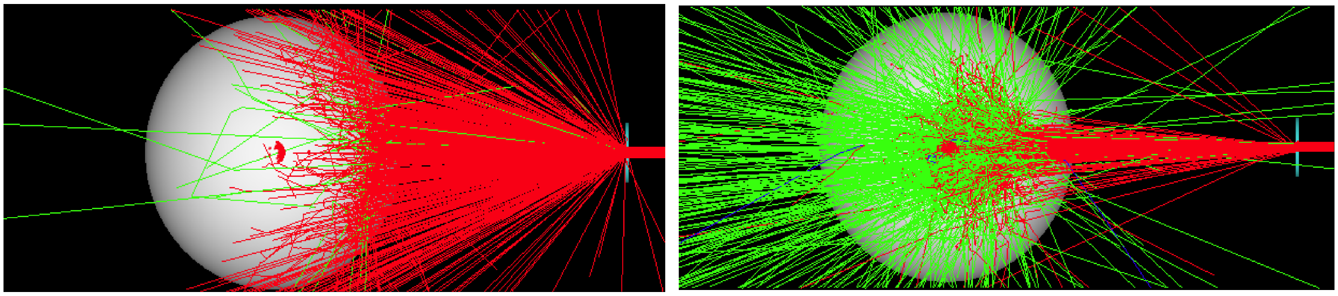

Figure 8 - HD1/HD2 electron simulation, left: Electron 2 Mev; right: Electron 15 Mev.

Geant4 also kept records of the interaction statistics, Figure 9 – 12 show the interaction statistics corresponding to different input particle energy.

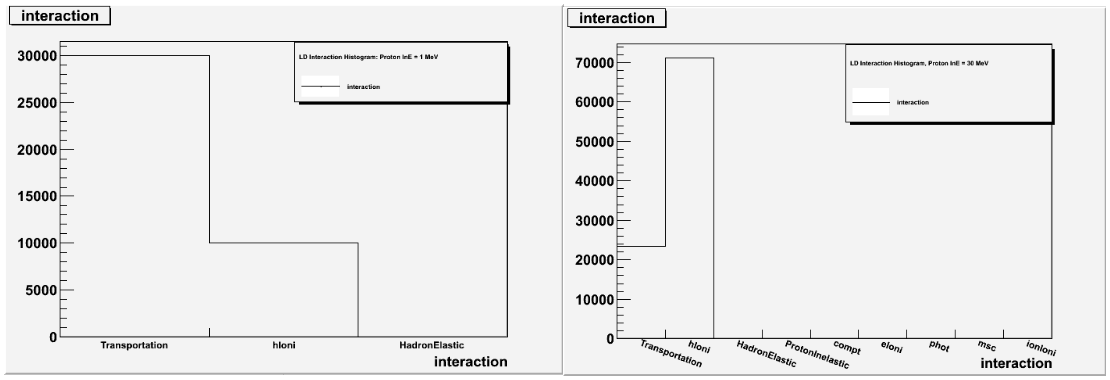

Figure 9 - LD interaction histogram Proton left: Ein=1Mev, right: Ein=30Mev

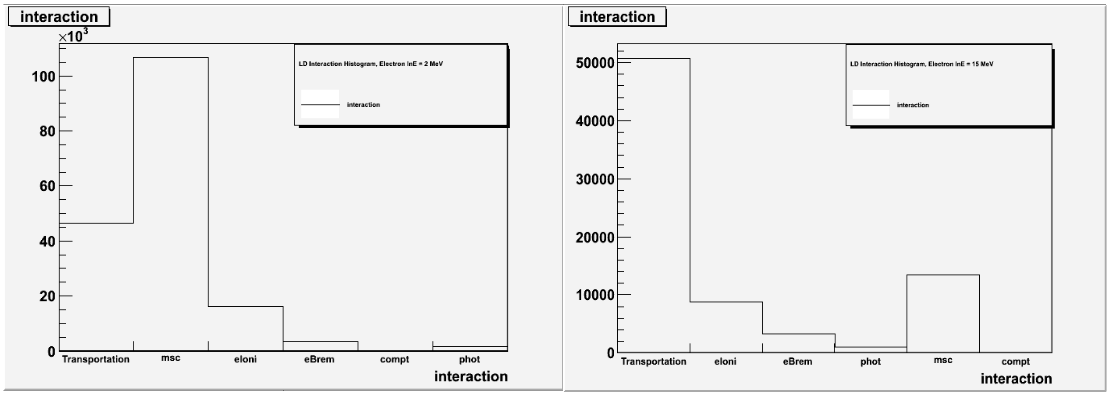

Figure 10 - LD interaction histogram electron left: Ein=2Mev, right: Ein=15Mev.

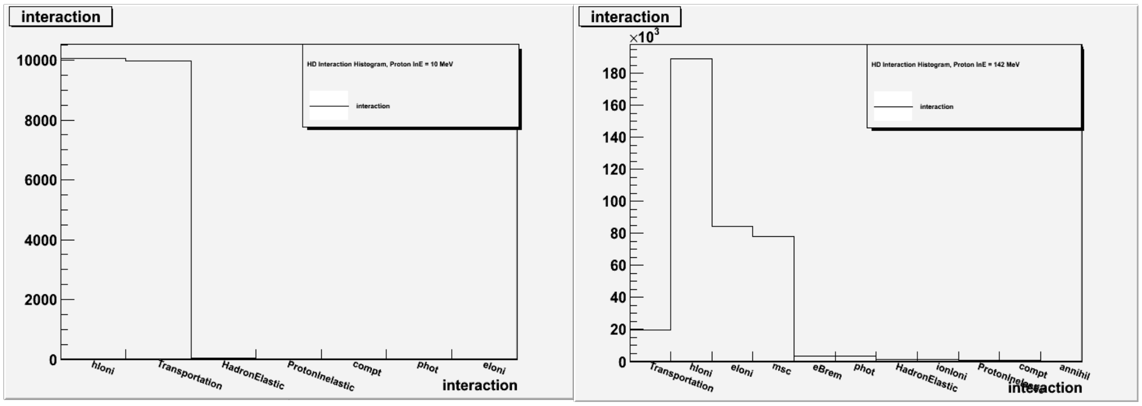

Figure 11 - HD interaction histogram Proton left: Ein=10Mev, right: Ein=142Mev.

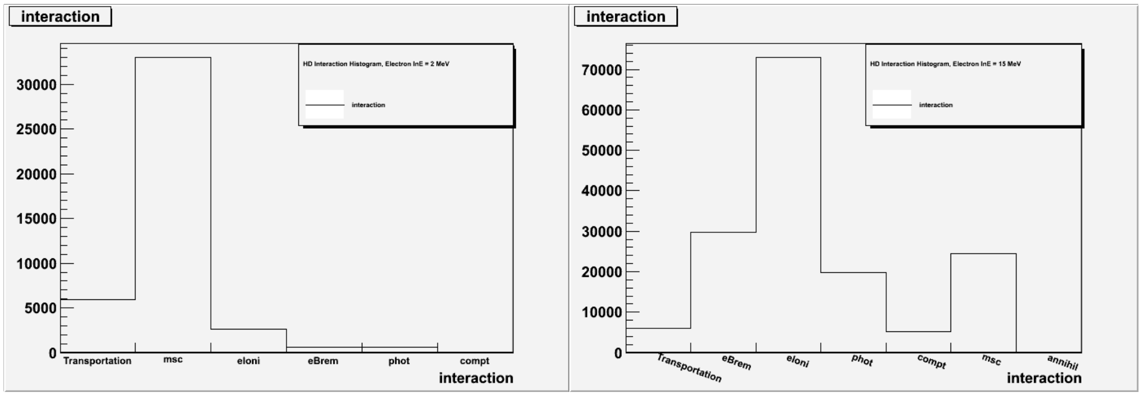

Figure 12 - HD interaction histogram electron left: Ein=2Mev, right: Ein=15Mev.

4. Conclusion and Future Work

From simulations the LD/HD detector energy response is calculated(Figure 13).

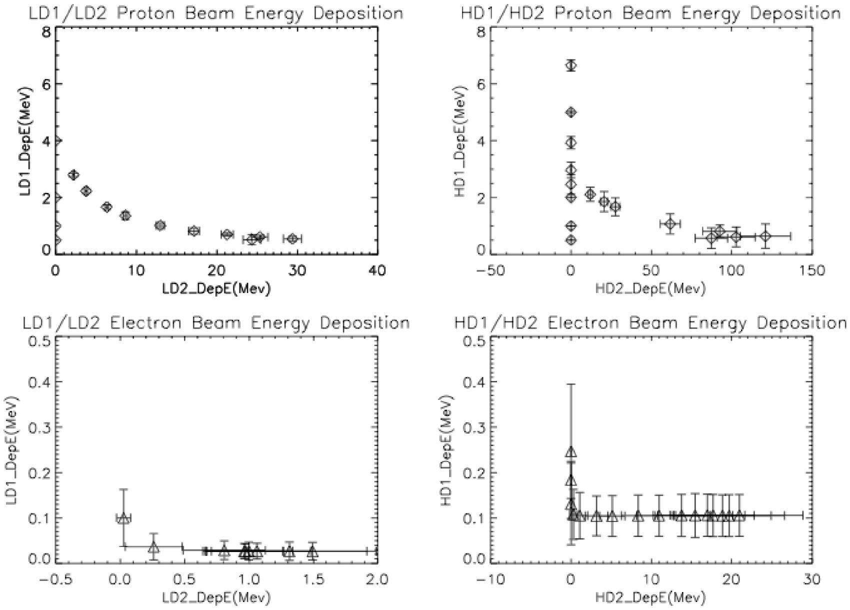

Figure 13 - Energy response

The preliminary results presented here will be combined with other calibration data to generate the better instrument response modeling. For future simulation works, there are two areas can be further refined: the instrument geometry and material modeling can be build in more realistic setup; the input particle beam parameters should be modified to reflect more realistic space environments, we can use existing experimental data such as CREME96 to generate better results.

References

1. Andrew Hoover, Marc Kippen, Mark Wallace, The General Response Simulation System (GRESS) User's Guide, 2007.
2. M. Wuest, D.S. Evans and R. Von Steiger, Calibration of Particle Instruments in Space Physics, 2007.

Angles-Only Orbit Determination For Electro-Optical Sensors

Richard Linares

Graduate Student, University at Buffalo

Abstract

This paper studies the problem of determining a resident space object's (RSOs) orbit from astrometric data. Solar radiation and atmospheric drag disturbance forces are modeled and used in the estimator. Two scenarios are used to simulate synthetic data for two different RSOs orbits, a geosynchronous transfer orbit and a low earth orbit scenario. Data samples are generated over a ten day period when the RSO is over the observation ground site, not in shadow, and the sky is dark enough for optical measurements. An Unscented Kalman Filter is applied to this problem and the orbit determination accuracy is shown using electro-optical measurements. The results are discussed and the two scenarios are compared.

Keywords: Nonlinear Filtering, Orbit Determination, Ballistic Coefficient Estimation

---

1. Introduction

In recent years space situational awareness, which is concerned with collecting and maintaining knowledge of all objects orbiting the Earth, has gained much attention. The U.S. Air Force collects the necessary data for space object catalog development and maintenance through a global network of radars and optical sensors. Due to the fact that a limited number of sensors are available to track a large number of resident space objects (RSOs), the sparse data collected must be exploited to the fullest extent. Various sensors, such as radars, exist for RSO state estimation, which typically includes position, velocity, and a non-conservative force parameter, B^*, analogous to a ballistic coefficient. This work models both the ballistic coefficient and the SRP albedo area-to-mass ratio while designing an estimator to estimate the orbits of a Low Earth Orbit (LEO) and Geostationary Transfer Orbit (GTO) RSO.

Deep space optical surveys of near geosynchronous (GEO) objects have identified a class of high area-to-mass ratio (HAMR) objects Schildknecht (2007). The exact characteristics of these objects are not well known and their motion pose a collision hazard with GEO objects due to the SRP induced, large variations of inclination and eccentricity. HAMR objects can also be influenced drag forces since the area-to-mass ratio is important in the magnitude of drag disturbances. by These objects are typically non-resolved and difficult to track due to dim magnitude and dynamic mismodeling. Therefore, characterizing the large population of HAMR objects in geostationary orbit is required to allow for a better understanding of their origins, and the current and future threats they pose to the active SO population.

Estimating the dynamic characteristics of a HAMR object using light curve and astrometric data can allow for area-to-mass parameters to be observable. It has been shown that the SRP albedo area-to-mass ratio, $\frac{C_r\mathcal{A}}{m}$, is observable from angles data Kelecy and Jah (2011) through the dynamic mismodeling of SRP forces. Reference Kelecy and Jah (2011) conducts a study with simulated and actual data to quantify the error in the estimates of $\frac{C_r\mathcal{A}}{m}$ and good performance is found using data spanning over a number of months. Also Ref. Linares et al. (2010, AIAA-2009-6293) shows that orbital, attitude and shape parameters can be recovered with sufficient accuracy using a multiple-model adaptive estimation approach coupled with an unscented Kalman filter. This approach works reasonably well but requires that the area-to-mass ratio is known *a priori*.

Email address: `linares2@buffalo.edu` (Richard Linares)

Los Alamos Space Weather Summer School 2012

Filtering algorithms for state estimation, such as the extended Kalman filter (EKF),Jazwinski (1970) the Unscented Kalman filter (UKF)Julier et al. (2000) and particle filtersGordon et al. (1993) are commonly used to both estimate hidden (indirectly observable) states and filter noisy measurements. The basic difference between the EKF and the UKF results from the manner in which the state distribution of the nonlinear models is approximated. The UKF, introduced by Julier and Uhlmann,Julier et al. (2000) uses a nonlinear transformation called the unscented transform, in which the state probability density function (pdf) is represented by a set of weighted sigma points. When the sigma points are propagated through the nonlinear system, the posterior mean and covariance are obtained up to the second order for any nonlinearity. The EKF and UKF assume that the process noise terms are represented by zero-mean Gaussian white-noise processes and the measurement noise is also represented by zero-mean Gaussian random variable. Furthermore both approaches assume that the *a posteriori* pdf is Gaussian in a linear domain. This is true given the previous assumptions but under the effect of nonlinear measurement functions and system dynamics the initial Gaussian state uncertainty may quickly become non-Gaussian. Both filters only provide approximate solutions to the nonlinear filtering problem, since the *a posteriori* pdf is most often non-Gaussian due to nonlinear effects. The EKF typically works well only in the region where the first-order Taylor-series linearization adequately approximates the non-Gaussian pdf. The UKF provides higher-order moments for the computation of the *a posteriori* pdf without the need to calculate Jacobian matrices as required in the EKF. The orbital dynamics and measurement models used for RSO orbit determination are highly nonlinear; thus, the UKF is used to provide a numerical means of estimating the states of the RSO.

This work studies the problem of orbit determination from angles measurements using an UKF. Two examples are investigated, the first is a LEO orbit and the second is a highly eccentric GTO orbit. Simulations are shown to highlight the filter performance in both cases. The organization of the paper is as follows, first a review of the UKF is provided. Following this astrometric observations are discussed and then a dynamic force model is provided. Solar Radiation Pressure and drag force models are then discussed and finally simulation examples are provided followed by a conclusion.

2. Unscented Transformation

The UKF, introduced by Julier and Uhlmann, Julier et al. (2000) uses a nonlinear transformation called the scaled unscented transformation, in which the state probability distribution is represented by a set of weighted sigma points, which are used to parameterize the true mean and covariance of the state distribution. When the sigma points are propagated through the nonlinear system, the posterior mean and covariance is obtained up to second order for any nonlinearity.

Consider the following nonlinear system and measurement model:

$$\mathbf{x}_{k+1} = \mathbf{f}(\mathbf{x}_k) + \mathbf{z}_k \tag{1a}$$

$$\tilde{\mathbf{y}}_k = \mathbf{h}(\mathbf{x}_k) + \mathbf{v}_k \tag{1b}$$

where $\mathbf{z}_k$ and $\mathbf{v}_k$ are zero-mean Gaussian noise processes with covariances $\mathbf{Q}$ and $\mathbf{R}$, respectively. The state vector is redefined in the UKF approach by augmenting the state vector to include noise variables, where the augmented state vector is defined by $\mathbf{x}_k^a = [\mathbf{x}_k^T\ \mathbf{z}_k^T\ \mathbf{v}_k^T]^T$ and the augmented state vector has dimension $N_a = N + q + l$. All random variables in the UKF are assumed to be Gaussian random variables. Therefore one can think of a joint distribution for the random variables, equivalent to the distribution of $\mathbf{x}_k^a$, defining a multivariate Gaussian distribution given by $w(\mathbf{x}_k^a) = w(\mathbf{x}_k, \mathbf{z}_k, \mathbf{v}_k)$. Then the joint distribution is approximated by $w(\mathbf{x}_k, \mathbf{z}_k, \mathbf{v}_k) \sim \mathcal{N}(\mathbf{x}_k^a, \mathbf{P}^a)$. The mean augmented vector $\mathbf{x}_k^a$ can written as $\mu^a = [\boldsymbol{\mu}^T\ \mathbf{0}_{l\times1}^T\ \mathbf{0}_{q\times1}^T]^T$, where $\boldsymbol{\mu}$ is the state estimate. The covariance matrix, $\mathbf{P}^a$, for the joint distribution can be written as

$$\mathbf{P}^a = \begin{bmatrix} \mathbf{P} & \mathbf{P}^{xz} & \mathbf{P}^{xv} \\ \mathbf{P}^{zx} & \mathbf{Q} & \mathbf{P}^{zv} \\ \mathbf{P}^{vx} & \mathbf{P}^{vz} & \mathbf{R} \end{bmatrix} \tag{2}$$

Then the distribution is approximated as a set of symmetric selected scaled sigma points. The sigma points are selected such that they are zero-mean, but if the distribution has mean $\boldsymbol{\mu}$, then simply adding $\boldsymbol{\mu}$ to each of the points yields a symmetric set of $2N_a$ points having the same covariance as the initial Gaussian distribution Julier et al. (2000). The sigma points are selected to be along the principal axis direction of the Gaussian distribution $w(\mathbf{x}_k^a)$ or along the eigenvector directions of $\mathbf{P}_k^a$. Then the augmented state vector and covariance matrix is constructed by using the following sigma points

$$\boldsymbol{\sigma}_k \leftarrow 2N_a \text{ columns from } \sqrt{(n_a+\lambda)\mathbf{P}_k^a} \tag{3a}$$

$$\chi_k^a(0) = \boldsymbol{\mu}_k \tag{3b}$$

$$\chi_k^a(i) = \boldsymbol{\sigma}_k(i) + \boldsymbol{\mu}_k \tag{3c}$$

Therefore given an $N_a \times N_a$ covariance matrix $\mathbf{P}_k^a$, a set of $2N_a$ sigma points can be generated from the columns of the matrices $\sqrt{(N_a+\lambda)\mathbf{P}_k^a}$, where $\sqrt{M}$ is shorthand notation for a matrix Z such that $M = Z\,Z^T$. Using the notation of the augmented state vector the sigma point vector can be written as

$$\chi_k^a(i) = \begin{bmatrix} \chi^x(i) \\ \chi^z(i) \\ \chi^v(i) \end{bmatrix} \tag{4}$$

Then, given that these points are selected to represent the distribution of the augmented state vector, each sigma point is given a weight that preserves the information contained in the initial distribution:

$$W_0^{mean} = \frac{\lambda}{N+\lambda} \tag{5a}$$

$$W_0^{cov} = \frac{\lambda}{N+\lambda} + (1-\gamma^2+\xi) \tag{5b}$$

$$W_i^{mean} = W_i^{cov} = \frac{\lambda}{2(N+\lambda)} \tag{5c}$$

where $\lambda = \gamma^2 N_a + \kappa - N_a$ includes scaling parameters. The constant parameter controls the size of the sigma point distribution and should be a small number $0 \leq \gamma \leq 1$, and κ provides an extra degree of freedom that is used to fine-tune the higher-order moments; $\kappa = 3 - N_a$ for a Gaussian distribution, also ξ is a third parameter that further incorporates higher-order effects by adding the weighting of the zeroth sigma point to the calculation of the covariance; note $\xi = 2$ is the optimal value for Gaussian distributions.

3. Astrometric Observation Model

Consider observations made by a optical site which measures azimuth and elevation to an RSO. The common terminology associated with this observation is given by, $\mathbf{d}^I$ is the position vector from the observer to the RSO, $\mathbf{r}^I$ is the position of the RSO in inertial coordinates, $\mathbf{R}^I$ is the radius vector locating the observer, α and δ is the right ascension and declination of the RSO, respectively, θ is the sidereal time of the observer, λ is the latitude of the observer, and ϕ is the east longitude from the observer to the RSO. The fundamental observation is given by

$$\mathbf{d}^I = \mathbf{r}^I - \mathbf{R}^I \tag{6}$$

In non-rotating equatorial (inertial) components the vector $\mathbf{d}^I$ is given by

$$\mathbf{d}^I = \begin{bmatrix} x - \|\mathbf{R}^I\|\cos(\theta)\cos(\lambda) \\ y - \|\mathbf{R}^I\|\sin(\theta)\cos(\lambda) \\ z - \|\mathbf{R}^I\|\sin(\lambda) \end{bmatrix} \tag{7}$$

The conversion from the inertial to the observer coordinate system (Up-East-North) is given by

$$\begin{bmatrix} \rho_u \\ \rho_e \\ \rho_n \end{bmatrix} = \begin{bmatrix} \cos(\lambda) & 0 & \sin(\lambda) \\ 0 & 1 & 0 \\ -\sin(\lambda) & 0 & \cos(\lambda) \end{bmatrix} \begin{bmatrix} \cos(\theta) & \sin(\theta) & 0 \\ -\sin(\theta) & \cos(\theta) & 0 \\ 0 & 0 & 1 \end{bmatrix} \mathbf{d}^I \tag{8}$$

The angle observations consist of the azimuth, az, and elevation, el. The observation equations are given by

$$\text{az} = \tan^{-1}\left(\frac{\rho_e}{\rho_n}\right) \tag{9a}$$

$$\text{el} = \sin^{-1}\left(\frac{\rho_u}{\|\mathbf{d}^I\|}\right) \tag{9b}$$

The az and el angles are used to defined the location of the RSO in the local sky and is used to determine if the RSO is over the horizon by defining a minimum el angle. For the simulations considered in this paper observations are required to satisfy el $>$ 20 Degs. In most cases angle observations are reported in right ascension and declination angles

$$\text{RA} = \tan^{-1}\left(\frac{\mathbf{d}^I(2)}{\mathbf{d}^I(1)}\right) \tag{10a}$$

$$\text{DEC} = \sin^{-1}\left(\frac{\mathbf{d}^I(3)}{\|\mathbf{d}^I\|}\right) \tag{10b}$$

When the RSO is over the horizon, sky is dark, and the RSO is not eclipsed by earth Eq. 10 is used to calculate angle observations of the RSOs.

4. Orbital and Attitude System Model

In this paper the position and velocity of an Earth orbiting RSO are denoted by $\mathbf{r}^I = [x \; y \; z]^T$ and $\mathbf{v}^I = [v_x \; v_y \; v_z]^T$, respectively. The equations of motion of the RSO are given by

$$\ddot{\mathbf{r}}^I = -\frac{\mu}{r^3}\mathbf{r}^I - \mathbf{a}_{J_2} + \mathbf{a}^I_{\text{srp}} + \mathbf{a}^I_{\text{drag}} \tag{11}$$

where μ is the gravitational parameter of the Earth, $r = \|\mathbf{r}^I\|$, $\mathbf{a}_{J_2}$ is the gravitational perturbation due to non-symmetric distribution of mass along the lines of latitude of the Earth and $\mathbf{a}^I_{\text{srp}}$ represents the acceleration perturbation due to SRP, which will be discussed in detail in the following section. The acceleration due to the J_2 effect is given by

$$\mathbf{a}_{J_2} = \frac{3}{2} J_2 \left(\frac{\mu}{r^2}\right)\left(\frac{R_\oplus}{r}\right)^2 \begin{bmatrix} \left(1 - 5\left(\frac{z}{r}\right)^2\right)\frac{x}{r} \\ \left(1 - 5\left(\frac{z}{r}\right)^2\right)\frac{y}{r} \\ \left(3 - 5\left(\frac{z}{r}\right)^2\right)\frac{z}{r} \end{bmatrix} \tag{12}$$

where $J_2 = 1.082\,626\,683 \times 10^{-3}$ is the coefficient for the second zonal harmonic and $R_\oplus = 6,378.137$ km is the mean equatorial radius of the Earth.

5. Solar Radiation Pressure

For higher altitude objects ($\geq$ 1,000 km) SRP represents the primary non-conservative perturbation acting on RSOs. Because SRP depends upon the RSO's position and orientation, the position and attitude dynamics are thus coupled. The acceleration due to SRP is computed as a function of the total solar energy impressed upon exposed RSO surfaces that are reflected, absorbed and reradiated. The rate at which radiant energy is incident on an element of area $d\mathcal{A}$ is a function of angle between the normal to $d\mathcal{A}$, $\mathbf{u}_n$, and the Sun direction $\mathbf{u}_{\text{sun}}$. The power of incident radiant energy is given by

$$P_I = \frac{\Phi_{\text{sun,tot}}}{(d/d_0)^2}\left(\mathbf{u}_n \cdot \mathbf{u}_{\text{sun}}\right) d\mathcal{A}, \tag{13}$$

where $\Phi_{\text{sun,tot}}$ is the average incident radiant flux density from the Sun at 1 AU, given by $\Phi_{\text{sun,tot}} = 1{,}367\ \text{W/m}^2$. Therefore the energy flux at any distance d is given by $\Phi_{\text{sun,tot}}/(d/d_0)^2$ where $d_0 = 1$ AU. The reflected radiation will have the following diffuse and specular power:

$$P_D = C_{\text{diff}} \frac{\Phi_{\text{sun,tot}}}{(d/d_0)^2} \left(\mathbf{u}_n \cdot \mathbf{u}_{\text{sun}}\right) d\mathcal{A} \tag{14a}$$

$$P_S = C_{\text{spec}} \frac{\Phi_{\text{sun,tot}}}{(d/d_0)^2} \left(\mathbf{u}_n \cdot \mathbf{u}_{\text{sun}}\right) d\mathcal{A}, \tag{14b}$$

where the incident solar radiant energy is accounted for in three terms: the absorbed energy, C_{abs}, the specularly reflected energy C_{spec}, and the diffusely reflected energy, C_{diff}, which yields

$$C_{\text{abs}} + C_{\text{spec}} + C_{\text{diff}} = 1. \tag{15}$$

The elemental force on $d\mathcal{A}$ can be written in three terms: incident force, $\mathbf{dF}_I$, specular reflection force, $\mathbf{dF}_S$, and diffuse reflection force, $\mathbf{dF}_D$. The incident force accounts for force due to the three terms C_{abs}, C_{spec}, and C_{diff}, since for each term the radiant particle is at least brought to rest before being absorbed or reflected. Therefore, $\mathbf{dF}_I$ accounts for the transfer in momentum to bring a radiated particle to rest. The force term for diffuse and specular reflectance accounts for the momentum transfer due to reflection. The momentum contribution due to incident energy is in the opposite direction of the normal, given by

$$\mathbf{dF}_I = -\frac{P_I}{c}\mathbf{u}_n. \tag{16}$$

The force exerted by specularly reflected energy is in the direction of specular reflection which is given by reflecting the vector $\mathbf{u}_{\text{sun}}$ about an axis defined by the direction $\mathbf{u}_n$. Then the force exerted by specular reflection is given by

$$\mathbf{dF}_S = \frac{P_S}{c}\left[2\left(\mathbf{u}_n \cdot \mathbf{u}_{\text{sun}}\right)\mathbf{u}_n - \mathbf{u}_{\text{sun}}\right]. \tag{17}$$

Diffusely reflected energy will reflect equally in all directions and the resulting force will be in the normal direction due to symmetric components canceling out. For surfaces obeying Lambert's cosine law of diffuse emission the diffuse term will be Ashikmin and Shirley (2000)

$$\mathbf{dF}_D = \frac{2}{3}\frac{P_D}{c}\mathbf{u}_n, \tag{18}$$

where the factor $\frac{2}{3}$ accounts for the portion of energy that is reflected in the normal direction. Then the force on an element of area is given by

$$\mathbf{dF} = \mathbf{dF}_I + \mathbf{dF}_S + \mathbf{dF}_D. \tag{19}$$

The force acting on a body due to solar radiation pressure can be determined by integrating over the Sun exposed surface area, given by

$$\mathbf{F} = \int_{\text{sun}} \left(\mathbf{dF}_I + \mathbf{dF}_S + \mathbf{dF}_D\right). \tag{20}$$

For a spherical body this integral is calculated over the Sun exposed area. The result is given by

$$\mathbf{F} = -\frac{\Phi_{\text{sun,tot}}}{c(d/d_0)^2}\mathcal{A}\left[1 + \frac{2}{3}C_{\text{diff}}\right]\mathbf{u}_{\text{sun}}. \tag{21}$$

This equation can be rewritten in terms of albedo

$$\mathbf{F} = -\frac{\Phi_{\text{sun,tot}}}{c(d/d_0)^2}C_r\mathcal{A}\mathbf{u}_{\text{sun}}, \tag{22}$$

where $C_r = 1 + \frac{2}{3}C_{\text{diff}}$.Finally the acceleration can be written as

$$\mathbf{a}_{srp}^{I} = -\frac{\Phi_{\text{sun,tot}}}{c(d/d_0)^2}\frac{C_r\mathcal{A}}{m}\mathbf{u}_{\text{sun}}, \tag{23}$$

where SRP albedo area-to-mass ratio is defined by $\alpha = \frac{C_r\mathcal{A}}{m}$.

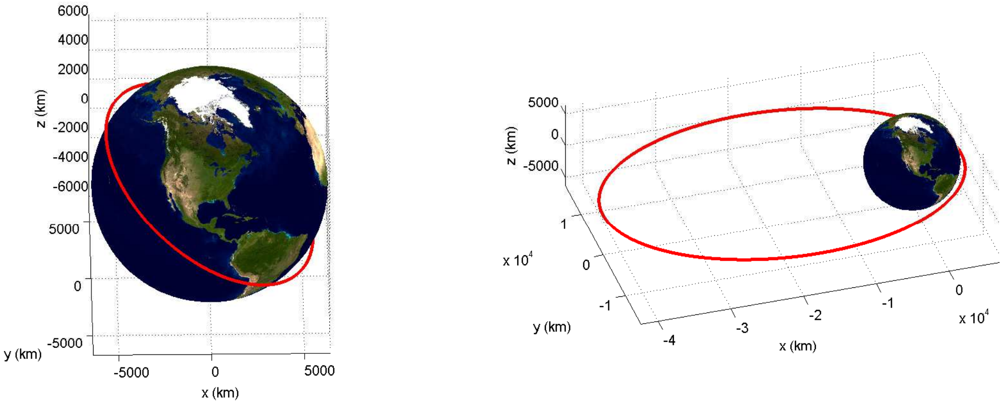

(a) Scenario 1

(b) Scenario 2

Figure 1: Orbits Considered in both Scenarios

6. Atmospheric Drag

In this section, discussed a very simple but instructive atmospheric drag model. The planar equations of motion for a LEO object affected by nonconservative atmospheric drag forces are given byVallado (2007)

$$\mathbf{a}^{I}_{drag} = -\frac{1}{2}\frac{C_d\mathcal{A}}{m}\rho\mathbf{v}^2_{rel}\frac{\mathbf{v}_{rel}}{|\mathbf{v}_{rel}|} \tag{24a}$$

$$\rho = \rho_0 e^{-\frac{(r-R_{\bigoplus})}{h}} \tag{24b}$$

where C_d is the coefficient of drag, A is the cross-sectional area, m is the mass of the object, and ρ is the atmospheric density at a given altitude. The atmospheric density model is assumed to be an exponential model with reference density ρ_0. It is also worth noting that the $\mathbf{v}_{rel}$ is not the velocity state vector, but rather the velocity relative to the Earth's atmosphere. For simulation purposes, the value of the ballistic coefficient, $\beta = \frac{C_d\mathcal{A}}{m}$, is chosen to be 1.4 which is consistent with a HAMR objectT. Schildknecht (2008).

7. Simulation Results

Two simulation scenarios are presented to show the performance of the UKF in determining the orbit of an RSO angles observations. For the first scenarios the RSO is in a Low Earth Orbit with orbital elements given by $a = 6778.0$ km, $e = 0$, $i = 0$ deg, $\omega = \Omega = 0.0$ deg and $M_0 = 119.6798$ deg. The second scenario is geosynchronous Transfer orbit with orbital elements given by $a = 24582.00$ km, $e = 0.72429$, $i = 0$ deg, $\omega = \Omega = 0.0$ deg and $M_0 = 91.065$ deg. The simulation epoch is 15-March-2010 at 04:00:00 GST.

Angle observations are simulated using the Maui Ground Based-Electro-Optical Deep Space Surveillance sensor as the ground station (20.71° North, 156.26° West, 3,058.6 m altitude). Measurements are corrupted by zero-mean Gaussian white noise with standard deviations of 1 arc-seconds on the right ascension observation, 1 arc-seconds on the declination observation and 0.1 for the brightness magnitude. Observations are available every 20 seconds throughout the 10 days long simulation when RSO is over the horizon, sky is dark, and the RSO is not eclipsed by earth.

7.1. Scenario 1

The First scenario considered a LEO RSO. The observation time intervals can be seen from Figure 3, as the RSO becomes visible for el angles greater then 20 Degs. Figure 2 shows the observation geometry and since the first scenario considers a LEO orbit, observations are only possible for short portions of the orbit as seen in figure 7. From

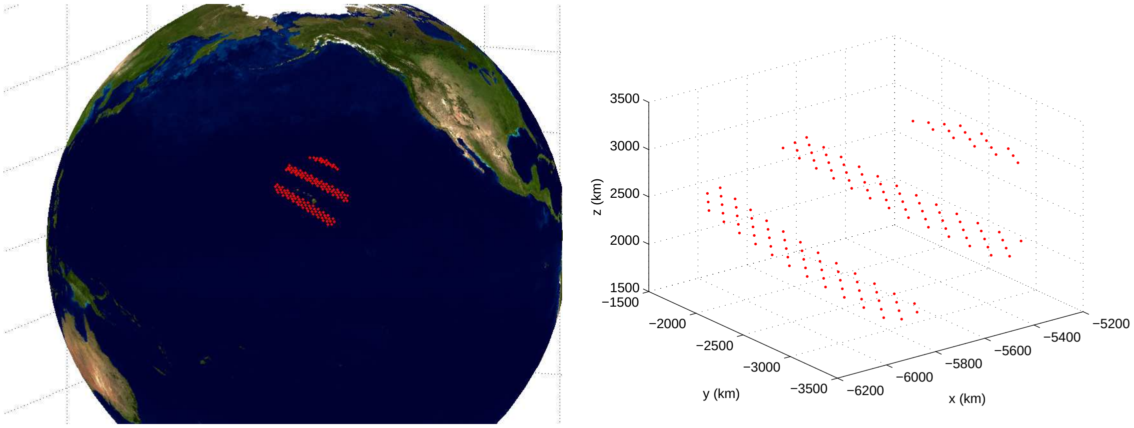

(a) Pass of RSO Over the Ground Site

(b) Orbital Position During Observations

Figure 2: Scenario 1 Passes of RSO Over Ground Site and portions of orbit that are observed.

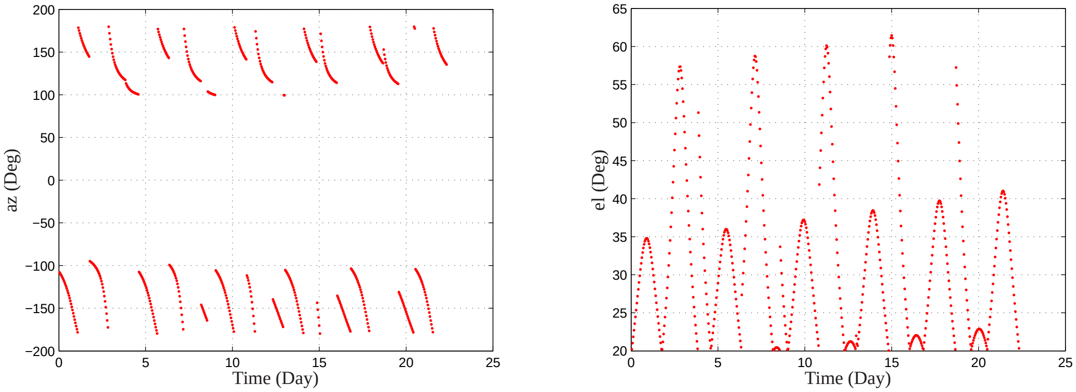

(a) Az Measurements

(b) El Measurements

Figure 3: Scenario 1 Az and El Measurement Satisfying El Constriants

Figure 7 we see the observable portions of the orbit plotted in Earth Centered Earth Fixed coordinated and although the RSO makes many pass over the ground site the individual observations tracks are small and do not cover a large portion of the RSOs orbit. Figure 4 shows the position variance for range, in-track, and cross-track directions over time. From this figure we can see the range directions has the highest variance and therefore highest uncertainty. This is due to the fact that the angles measurement are not very sensitive to range since they measure the RSO's location in the sky and not the distance to the observer.

7.2. Scenario 2

The second scenario considered a GTO RSO. The observation time intervals can be seen from Figure 5, as the RSO becomes visible for el angles greater than 20 Degs. Figure 7 shows the observation geometry and since the second scenario considers a GTO orbit observations are sampled for a larger portion of the RSO's orbit and since the RSO has a more eccentric orbit, larger variations in range are observed as seen in figure 7.2. From Figure 7.2 we see the observable portions of the orbit plotted in earth centered earth fixed coordinates and the RSO make fewer passes as compared to the LEO scenario. Figure 6 shows the position variances for range, in-track, and cross-track directions over time. The difference between the in-track and cross-track versus the range uncertainty is not as great as the LEO

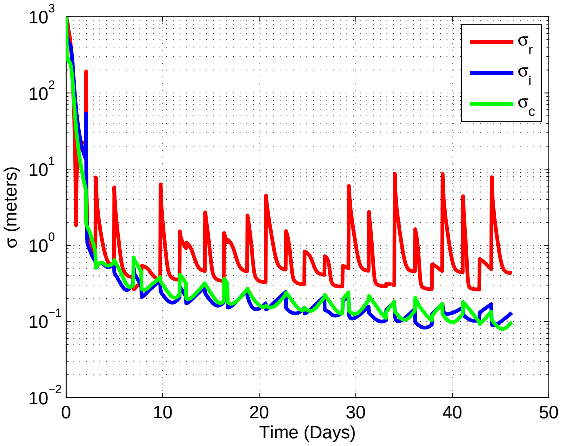

Figure 4: Range, In-Track, and Cross-Track Variances Over Time for Scenario 1

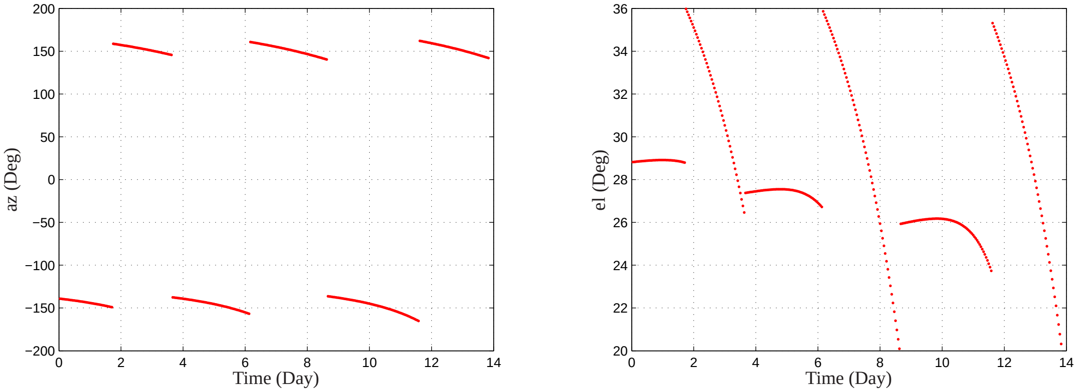

(a) Az Measurements

(b) El Measurements

Figure 5: Scenario 1 Az and El Measurement Satisfying El Constriants

scenario and this is due to the fact the the GTO scenario has a higher eccentricity and therefore large range variation in range.

8. Conclusion

This paper presented an Unscented Kalman filter for angles only orbit determination. Two scenarios were studied, the first considered a LEO orbit and the second considered a GTO orbit. For LEO orbit there are more observation opportunities but the observation tracks are over short portions of the RSO's orbit. For GTO orbit the observation opportunities are less but the tracks span large portions of the orbit. The GTO orbit have larger range variations since they typically have large eccentrics, needed to transfer a payload form LEO to GEO, and this creates greater observability in range. Finally good filter performance was shown in both scenarios and future work will considered the estimation of the SRP albedo area-to-mass ratio and the ballistic coefficient along with the RSO's positions states.

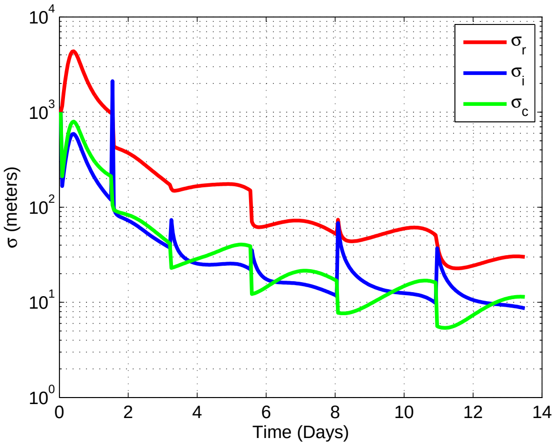

Figure 6: Range, In-Track, and Cross-Track Variances Over Time for Scenario 2

9. Acknowledgement

This work was supported through the Vela Fellowship from Los Alamos National Laboratory. The author wishes to thank Michael A. Shoemaker and David Palmer for many useful conversations related to this work.

References

Ashikmin, M., Shirley, P., 2000. An Anisotropic Phong Light Reflection Model. Technical Report UUCS-00-014. University of Utah. Salt Lake City, UT.

Gordon, N.J., Salmond, D.J., Smith, A.F.M., 1993. Novel approach to nonlinear/non-gaussian bayesian state estimation, in: IEE Proceedings, Part F - Communications, Radar and Signal Processing, Seattle, WA. pp. 107–113.

Jazwinski, A.H., 1970. Stochastic Processes and Filtering Theory. Academic Press, San Diego, CA. chapter 8.

Julier, S.J., Uhlmann, J.K., Durrant-Whyte, H.F., 2000. A new method for the nonlinear transformation of means and covariances in filters and estimators. IEEE Transactions on Automatic Control AC-45, 477–482.

Kelecy, T., Jah, M., 2011. Analysis of high area-to-mass ratio (hamr) geo space object orbit determination and prediction performance: Initial strategies to recover and predict hamr geo trajectories with no a priori information. Acta Astronautica 69, 551–558.

Linares, R., Crassidis, J.L., Jah, M., Kim, H., 2010, AIAA-2009-6293. Astrometric and photometric data fussion for orbit, attitude, and shape estimation, in: AIAA Guidance, Navigation and Control Conference, Chicago, IL.

Schildknecht, T., 2007. Optical Surveys for Space Debris. Astronomy and Astrophysics Review 14, 41–111.

T. Schildknecht, R. Musci, T.F., 2008. Properties of the high area-to-mass ratio space debris population at high altitudes. Advances in Space Research 41, 1039–1045.

Vallado, D.A., 2007. Fundamentals of Astrodynamics and Applications. Microcosm.

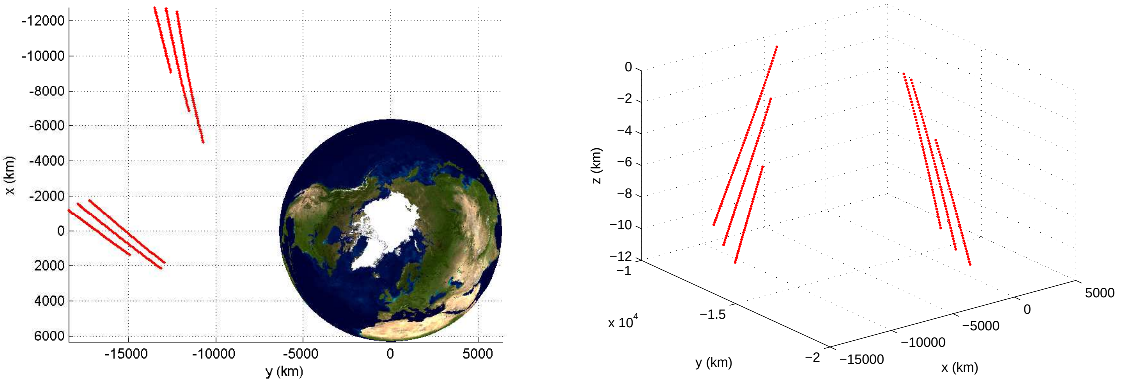

(a) Pass of RSO Over the Ground Site (b) Orbital Position During Observations

Figure 7: Scenario 1 Az and El Measurement Satisfying El Constraints

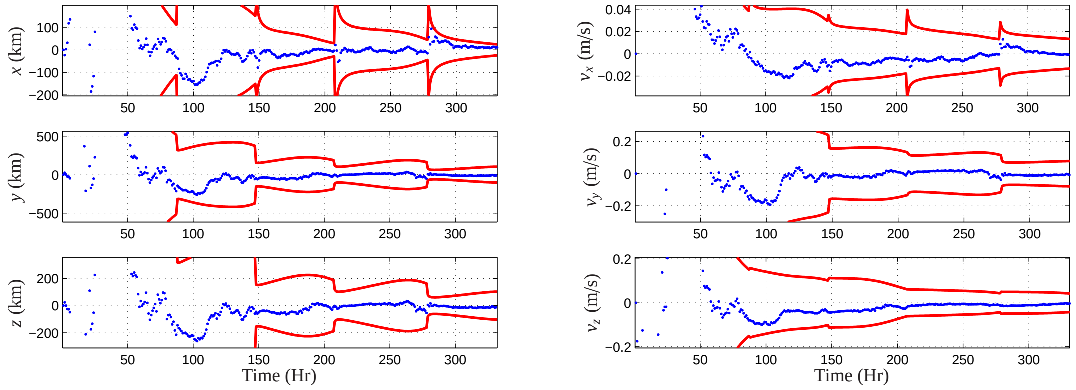

(a) Position Errors (b) Velocity Errors

Satellite Drag Coefficient Modeling

Piyush M. Mehta

The University of Kansas, 1530 W 15th Street, Lawrence KS 66045

Balu Nadiga

Los Alamos National Laboratory, Los Alamos NM

Michael Shoemaker

Los Alamos National Laboratory, Los Alamos NM

Abstract

Atmospheric density and drag coefficient are the two largest sources of error in calculating the aerodynamic forces on a satellite in an orbit between 150 and 1000 km. Conjunction analysis uses a constant drag coefficient to predict the orbit for most satellites. This use of a constant drag coefficient can quickly introduce orbit prediction errors on the order of hundreds of meters to a kilometer. To accurately determine and predict the orbit path of a satellite, both density modeling and drag coefficient modeling need to be improved. This research concentrates on modeling drag coefficient. The computational Direct Simulation Monte Carlo (DSMC) code DS3V (Direct Simulation Three-Dimensional Visual Program) is used to compute drag coefficients. The effectiveness of DS3V in simulating quasi-specular and partial energy accommodation gas-surface interactions is examined using analytical solutions for a sphere and cylinder. The sensitivity of drag coefficient to various input parameters is also examined. Result validate the ability of DS3V to simulate quasi-specular and partial energy accommodation gas-surface interactions and also show that developing drag coefficient models using the DSMC technique is highly feasible.

Keywords: Direct Simulation Monte Carlo, drag, DS3V, modeling, gas-surface interactions

---

1. Introduction

1.1. Drag Theory

Atmospheric drag is a major factor in predicting the orbit of a satellite in the extreme upper atmosphere. Equation 1 describes the theoretical model used for satellite drag calculations.

$$\vec{a}_{drag} = -\frac{1}{2}\rho\frac{C_D A}{m}v_{rel}^2\frac{\vec{v}_{rel}}{|\vec{v}_{rel}|} \tag{1}$$

Where $\vec{a}_{drag}$ is the acceleration due to drag, ρ is the atmospheric density, C_D is the satellite drag coefficient, A is the satellite drag area, m is the mass of the satellite, and $\vec{v}_{rel}$ is the relative velocity of the satellite with respect to the atmosphere. For satellites with compact shapes, like spherical and cylindrical satellites, the atmospheric density and the drag coefficient are the biggest sources of error. For non-primitive satellites with complex geometries, the drag area adds a certain level of uncertainity in modeling accelerations due to drag. Neutral wind in the atmosphere is also a cause of uncertainity in the calculation of aerodynamics forces. Winds on the order of 1km/s have been observed at high latitudes during strong geomagnetic storms (Marcos et al., 2007). However, for the purpose of this study the neutral winds have been neglected.

Email addresses: `pmehta@ku.edu` (Piyush M. Mehta), `balu@lanl.gov` (Balu Nadiga), `shoemaker@lanl.gov` (Michael Shoemaker)

Los Alamos Space Weather Summer School 2012

1.2. Atmospheric Density Models

Atmospheric density and satellite drag coefficient are two unknowns in a single equation, as seen in Equation 1, and are therefore intertwined and cannot be easily separated. Typically, density models have been updated by using spherical calibration spheres at different altitudes and using a constant drag coefficient for these spheres to fit densities to observed orbital data. This use of a constant drag coefficient induces errors in the density estimates derived from these empirical density models.

The High Accuracy Satellite Drag Model (HASDM) developed by the Air Force Space Battle Lab estimates and predicts a dynamically varying global density field using a dynamic calibration of atmosphere (DCA) algorithm to solve for the real-time phases and amplitudes of the diurnal and semidiurnal variation of the upper atmospheric density (Storz et al., 2002). HASDM uses objects with compact shapes and drag coefficients that vary with altitude to derive density corrections using orbital drag data. The use of drag coefficients that vary with altitude fail to account for density variations along the orbit of the satellite.

Wright (2003) and Wright and Woodburn (2004) recently developed a technique for real-time estimation of atmospheric density and ballistic coefficient as a part of the orbit determination process. Wright's technique for simultaneously estimating real-time atmospheric density and ballistic coefficient provides an advantage over the standard techniques of estimating only ballistic coefficient or drag coefficient individually. The density and ballistic coefficient corrections are modeled as exponential Gauss-Markov processes, which determine the density correction at any given time step as a function of corrections from previous time steps. The technique was recently validated and successfully used by McLaughlin et al. (2011) for CHAMP and GRACE satellites.

The state-of-the-art empirical density models show good statistical agreement with densities derived from actual spacecraft data during quiet times but are limited in advancing our understanding of the physical processes in the upper atmosphere. The physics based Global Ionosphere-Thermosphere Model (GITM) (Basis of the IMPACT project, www.impact.lanl.gov) enables us to answer important physics questions regarding the coupling between space weather, upper atmospheric density, and orbital drag by accurately describing the energy deposition and cooling during space weather events. However, the model is allowed to evolve using physical relationship and phenomenon using the initial and boundary conditions. Therefore, it is important to validate the model by comparing the model output (total density, constituent densities, and atmospheric translational temperature) with trusted empirical models.

1.3. Projected Drag Area

The projection area, A, for a satellite is a function of the geometry, and the attitude of the satellite relative of the free-stream. This area remains constant for satellite with primitive geometries such as a sphere or a cylinder flying in an arrow orientation. However, most satellite in low-Earth orbit (LEO) do not have primitive but have complex geometries and require attitude data for accurate estimation of drag area. Since the drag coefficient of a sphere and a cylinder in arrow orientation is insensitive to projected drag area, the validation for the DS3V code is done using spherical and cylindrical satellites.

1.4. Drag Coefficient

The drag coefficient of a spacecraft in LEO is a strong function of the way the free-stream molecules interact with the surface of the spacecraft, the orientation of the spacecraft relative of the atmosphere, spacecraft geometry, the velocity of the spacecraft relative to the atmosphere, the chemical composition of the atmosphere, the atmospheric temperature at the spacecraft location, and the surface properties of the spacecraft. In the realm of spacecraft dynamics and orbit determination, the drag coefficient can be referred to in three distinct ways: (i) the physical drag coefficient, (ii) the fitted drag coefficient, and (iii) the fixed drag coefficient. The physical drag coefficient is determined by the exchange of momentum by the free-stream atmospheric molecules with the spacecraft surface (Moe et al., 2012). On the other hand, fitted drag coefficients are estimated as part of an orbit determination process and fixed drag coefficient is a constant value of C_D. Fitted drag coefficients are specific to the atmospheric model used and carry along the limitations of the atmospheric model and also frequently absorb other force model errors. Throughout this document, the term drag coefficient will refer to physical drag coefficient, unless stated otherwise.

1.4.1. Energy-Accommodation Coefficient

Drag coefficient of a satellite is a strong function of how the incident free-stream molecules interact with the surface of the spacecraft. An important parameter that describes this interaction is the energy accommodation coefficient. Energy accommodation is defined as the fraction of the kinetic energy lost by the molecules incident on the spacecraft surface before reemission. The formal definition of energy accommodation is given later in Equation 2.

Measurements from pressure gauges and mass spectrometers flown on satellites have shown that surfaces of satellites orbiting in LEO are covered with a layer of adsorbed atomic oxygen and its reaction products (Moe et al., 1969; Hedin et al., 1973; Moe et al., 1998). Molecules striking contaminated surfaces have been observed to have high energy accommodation coefficients and be reemitted with a diffuse (Maxwellian) angular distribution (Stickney and Hurlbut, 1963; Kostoff et al., 1967).

Empirically determined energy accommodation coefficients as a function of altitude for solar-maximum and solar-minimum conditions for satellites orbiting in LEO are provided by (Moe et al., 1995; Bowman et al., 2005; Pardini et al., 2010). Recently, a semi-empirical model for satellite energy accommodation coefficients was developed (Pilinski et al., 2010). Since the empirical NRLMSISE-00 density model was used to map average atmospheric properties as a function of altitude, the energy accommodation model developed by (Pilinski et al., 2010) can be used only with the empirical NRLMSISE00 density model and brings with it the model errors in the number density of atomic oxygen and the free-stream atmospheric temperature. Because the focus of this study is validation of the DS3V code, the energy accommodation coefficient was varied over its entire range from 0 to 1, and hence is not tied to a specific model.

1.4.2. Gas-Surface Interaction (GSI) Models

Free-stream molecules that interact with a clean spacecraft surface are reflected in a specular way. However, satellite surfaces in LEO are predominantly contaminated with atomic oxygen. A free-stream molecule, when interacting with a contaminated surface, gets adsorbed by the layer of atomic oxygen, attains equilibrium with the surface, and is reemitted with a Maxwellian or diffuse distribution. As the altitude of the satellite increases, the number density of oxygen decreases and that of helium increases. Helium has a lower energy accommodation than atomic oxygen. Therefore, the increase of helium in the atmosphere results in a low overall energy-accommodation, and results in the molecules being reemitted with a Gaussian distribution about an angle between the surface normal and the specular angle. Such a reflection is called a quasi-specular reemission first introduced by (Schamberg, 1959). Figure 1 shows the picture representation of a diffuse (Maxwellian) or a quasi-specular reflection distribution.

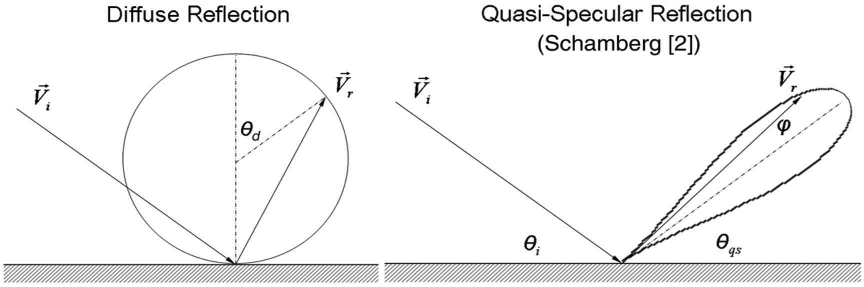

Figure 1: Gas-Surface Interaction Models

1.4.3. Spacecraft Surface Temperature

The spacecraft surface temperatures for a typical surface material (aluminum, solar array, etc.) can be estimated using the equations outlined in Brown (2002). The surface temperature can vary widely depending on the exposure of the spacecraft to the sun. Aluminum was used for surface temperature calculations for the purpose of this study. Temperatures calculated for an aluminium sphere using equations in Brown (2002) yielded temperatures of 465 K in sunlight and 183 K in darkness.

1.5. Direct Simulation Monte Carlo

The Direct Simulation Monte Carlo, DSMC, technique was developed and first applied by Bird (1994) in 1963. The Monte Carlo method is a generic numerical method for a variety of mathematical problems based on computer generation of random number. DSMC is the Monte Carlo method for simulation of dilute gas flows at the molecular level. DSMC is, to date, the basic numerical method in the kinetic theory of gases and rarefied gas dynamics. The DSMC method uses a cell and particle approach to track a system of representative molecules, while probabilistically selecting candidates for inter-molecular collisions. Every simulated molecule represents W molecules of real gas, where W is the statistical weight of a simulated molecule. The statistical weight typically lies in the range of 10^{12} to 10^{20} real molecules per every simulated molecule.

The computational domain is divided into small cells and molecules in each cell are tracked independently. The position coordinates and velocity components of the simulated molecules are stored in the memory of the computer and are modified with time as the molecules are concurrently tracked through representative collision and boundary interactions within the computational domain. At any given time, collision probabilities are calculated and collisions are carried out only between molecules in the same cell. The motion of the molecules and the collisions between them are decoupled over small time steps. The time step is much smaller than the mean collision time and a typical cell dimension is much smaller than the local mean free path (Bird, 2006).

The satellite or spacecraft geometry is inserted into flow field as a surface mesh. The mesh format differs from one program to another. Molecules are inserted into the flow field at the local boundary temperature through the inflow boundaries using a Maxwellian distribution in velocity. In typical DSMC simulations, like the flow over a satellite or a vehicle in the Earths atmosphere, the computational domain is part of a larger flow environment. The boundaries of the computational domain are therefore set to be transparent or as part of the free-stream. Molecules are allowed to leave and enter the computational domain while varying the number of simulated molecules with time.

1.5.1. DS3V

The DS3V (Direct Simulation Three-Dimensional Visual Program) was used to model the interactions of simulated molecules with parameterized surfaces and intermolecular collision dynamics. In spite of the computationally demanding nature of DS3V, it was chosen for three main reasons: (i) it is freely available on the Internet (www.gab.com.au), (ii) it is highly reliable and has been widely used, and (iii) it is very user friendly (Graphical User Interface). Figure 2 shows a screenshot of the 3-Dimensional DSMC program DS3V developed by (Bird, 1994).

The only computational parameter specified by the user is the initial number of megabytes to be used for storage. The size of the cells used to discretize the computational domain is set as a function of this initial number of megabytes defined by the user. The program sets all other computational variables automatically. However, an optional menu is available should the user choose to define the computational parameters.

DS3V does not allow the user to explicitly specify a value of accommodation coefficient. The default is complete accommodation. Therefore, in order to simulate partial energy accommodation, the temperature of the spacecraft surface is set equal to the kinetic temperature of the reemmitted molecules. This forces an assumption of single reflection of individual molecules. This mean that, once a molecule interacts with the surface of the spacecraft, it travels a large distance before colliding with another incoming molecule and looses any chance of re-interacting with the surface. Single reflections are dominant in free molecular flow (FMF) for simple convex geometries. However, caution needs to be taken when dealing with concave and complex geometries. Pilinski et al. (2011) showed that the difference in drag coefficients computed for concave geometries using single and multiple reflections is less than 1%.

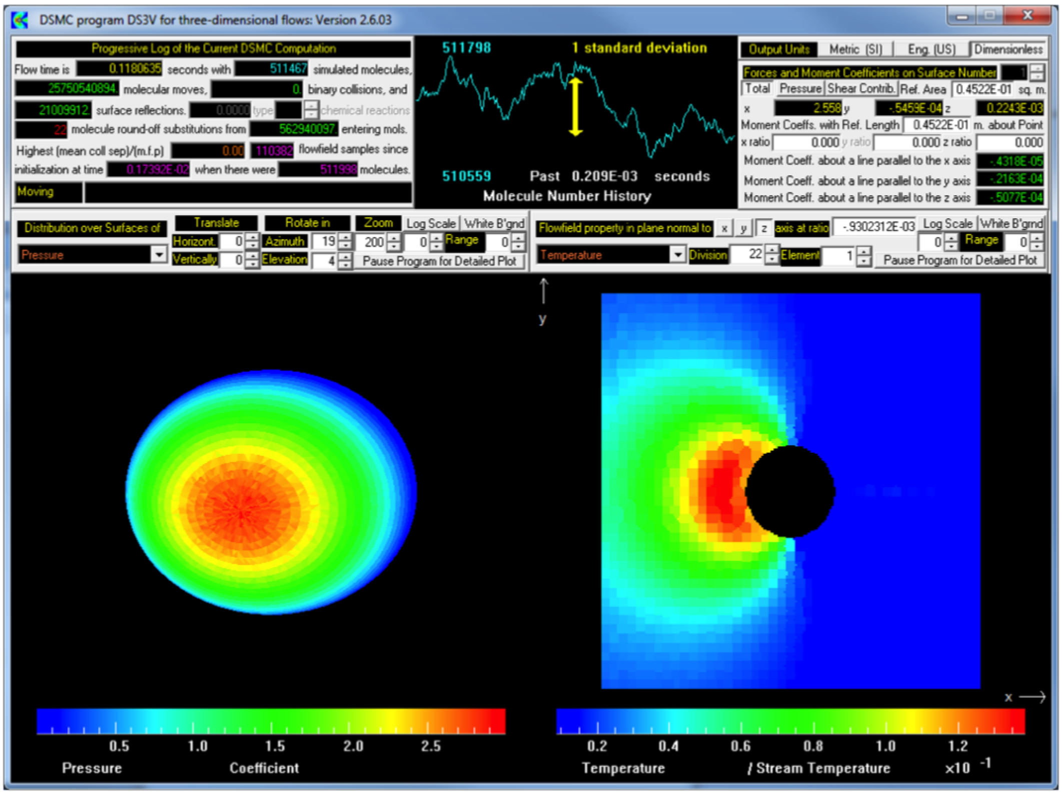

DSMC program DS3V for three-dimensional flows: Version 2.6.03

Progressive Log of the Current DSMC Computation

Flow time is 0.1180635 seconds with 511467 simulated molecules,
25750540894. molecular moves, 0. binary collisions, and
21009912. surface reflections. 0.0000 type chemical reactions
22 molecule round-off substitutions from 562940097. entering mols.
Highest (mean coll sep)/(m.f.p) 0.00 110382 flowfield samples since
initialization at time 0.17392E-02 when there were 511998 molecules.
Moving

Forces and Moment Coefficients on Surface Number 1
Ref. Area 0.4522E-01 sq. m.
x 2.558 y -.5459E-04 z 0.2243E-03
Moment Coeffs. with Ref. Length 0.4522E-01 m. about Point
x ratio 0.000 y ratio 0.000 z ratio 0.000
Moment Coeff. about a line parallel to the x axis -.4318E-05
Moment Coeff. about a line parallel to the y axis -.2163E-04
Moment Coeff. about a line parallel to the z axis -.5077E-04

Distribution over Surfaces of: Pressure
Translate: Horizont. 0, Vertically 0
Rotate in: Azimuth 19, Elevation 4
Zoom 200
Range 0 0

Flowfield property in plane normal to z axis at ratio -.9302312E-03
Temperature
Division 22 Element 1
Range 0 0

Figure 2: Screenshot of the DS3V module

2. Closed Form Analytical Equations

The energy accoommodation coefficient, α, is formally defined as:

$$\alpha = \frac{T_{k,i} - T_{k,r}}{T_{k,i} - T_w} \tag{2}$$

where $T_{k,i}$ is the kinetic temperature of the incoming molecules, $T_{k,r}$, is the kinetic temperature of the reemitted molecules, and T_w is the energy the reemitted molecules would have if they attained thermal equilibrium with the spacecraft surface before emission. The kinetic temperature of the incident molecules can be given as:

$$T_{k,i} = \frac{mv_{rel}^2}{3k_b} \tag{3}$$

where m is the mean molecular mass of the atmosphere at the satellite location, v_{rel} is the spacecraft relative velocity, and k_b is the Boltzmann's constant. The kinetic temperature of the reflected molecules for a monatomic species if given as:

$$T_{k,r} = T_{k,i}(1 - \alpha) + \alpha T_w \tag{4}$$

The expected errors in applying Equation 4 to diatomic molecules in less than 1%. The speed ratio s is defined as the ratio of the satellite speed to the most probable thermal speed of the ambient molecules.

$$s = v_{rel}\beta \tag{5}$$

$$\beta = \sqrt{\frac{m}{2k_b T_\infty}} \tag{6}$$

where T_∞ is the free-stream atmospheric temperature. The error function, erf() is defined as:

$$erf(s) = \frac{2}{\sqrt{\pi}} \int_0^s exp(-t^2)dt \tag{7}$$

Equation 8 defines the analytical solution for the drag coefficient of a sphere for a quasi-specular gas-surface interaction model with complete accommodation (α=1), originally derived by Schamberg (1959) and re-derived by Bird (1994). In case of partial accommodation simulation with DS3V, ($\alpha \neq$1), the surface temperature T_w is replaced by the kinetic temperature of the reflected molecules, $T_{k,r}$, for the appropriate value of the accommodation coefficient. T_∞ is the thermal temperature of the ambient gas irrespective of its bulk motion.

$$C_{D,sphere} = \frac{2s^2+1}{\sqrt{\pi}s^3} exp(-s^2) + \frac{4s^4+4s^2-1}{2s^4} erf(s) + \frac{2(1-\epsilon)\sqrt{\pi}}{3s}\sqrt{\frac{T_w}{T_\infty}} \tag{8}$$

Equation 9 defines the analytical solution for the drag coefficient of a cylinder for a diffuse GSI with complete accommodation deduced by Sentman (1961).

$$C_{D,cylinder} = \frac{4}{\sqrt{\pi}s}\frac{L}{D}[(2+\frac{1}{s^2})erf(s) + \frac{2}{\sqrt{\pi}s}e^{-s^2} + \frac{\sqrt{\pi}}{s}\sqrt{\frac{T_w}{T_\infty}} \tag{9}$$

3. Results

Sensitivity studies were performed to understand the variation of drag coefficient with the different input parameters. Sensitivity studies were performed using the following reference values: an atmospheric temperature of 1157 K, a surface temperature of 300 K, a relative atmospheric speed of 7590 m/s, and a molecular mass of 11.35 atomic mass units. Different input parameters were varied one at a time in the range observed in low-Earth orbits while keeping the other fixed at the above mentioned reference values. Figure 3 shows that the drag coefficient can vary by 2-3% as a function of spacecraft surface temperature between day and night cycles.

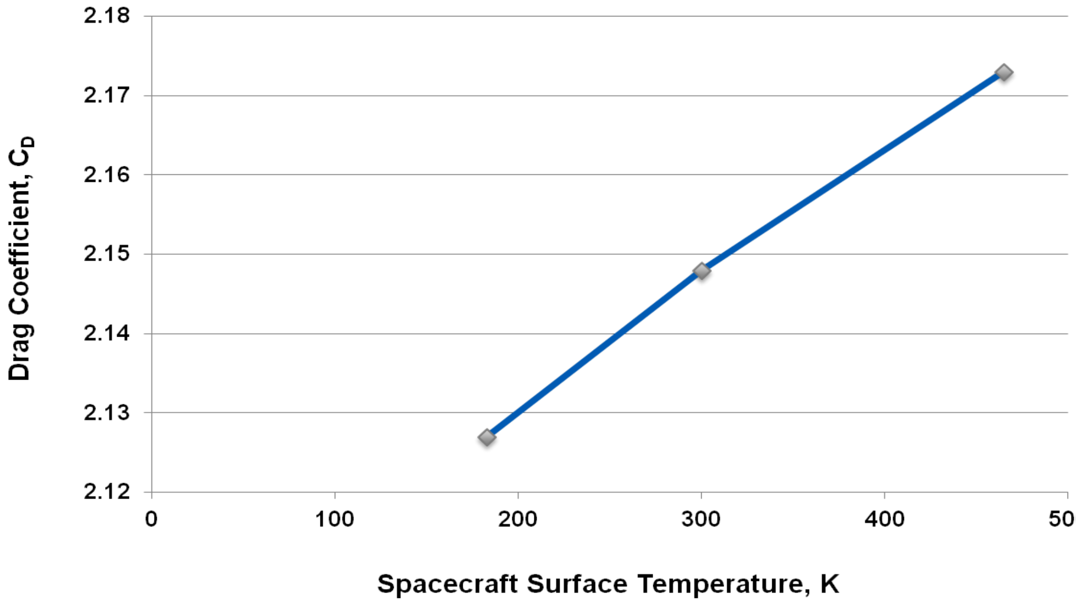

Figure 3: Variation of drag coefficient of a sphere with spacecraft surface temperature

Figure 4 and Figure 5 show the variation of the drag coefficient with free-stream atmospheric temperature and the spacecraft relative velocity respectively. Results shows strong correlation of the drag coefficient to both the free-stream atmospheric temperature as well as spacecraft relative velocity.

Although gas-surface interactions below 500 km in altitude are dominantly diffuse in nature, the ability of the DS3V code to simulate quasi-specular interactions was examined using a sphere for possible use at higher altitudes in the future. Figure 6 shows that the DS3V does well in simulation quasi-specular gas surface interactions.

Figure 7 shows the ability of DSMC to compute the drag coefficient for sphere as a function of accommodation coefficient and the sensitivity of drag coefficients to energy-accommodation. The results show that the computed drag coefficients start to diverge from the analytical solution as accommodation coefficient goes down. This is an expected result since as accommodation coefficient decreases, more and more of the adsorption effect is being incorporated through a constant uniform surface temperature.

Figure 8 shows the ability of DSMC to compute the drag coefficient for a cylinder as a function of the accommodation coefficient. The results again show that the computed drag coefficients start to diverge from the analytical solution as accommodation coefficient goes down. However, according to the energy-accommodation model of Pilinski, accommodation coefficients vary from 0.9 to 1 at altitudes below 500 km. Therefore, it can be concluded that DSMC performs well in explicitly computing drag coefficients for satellites at altitudes with partial accommodation.

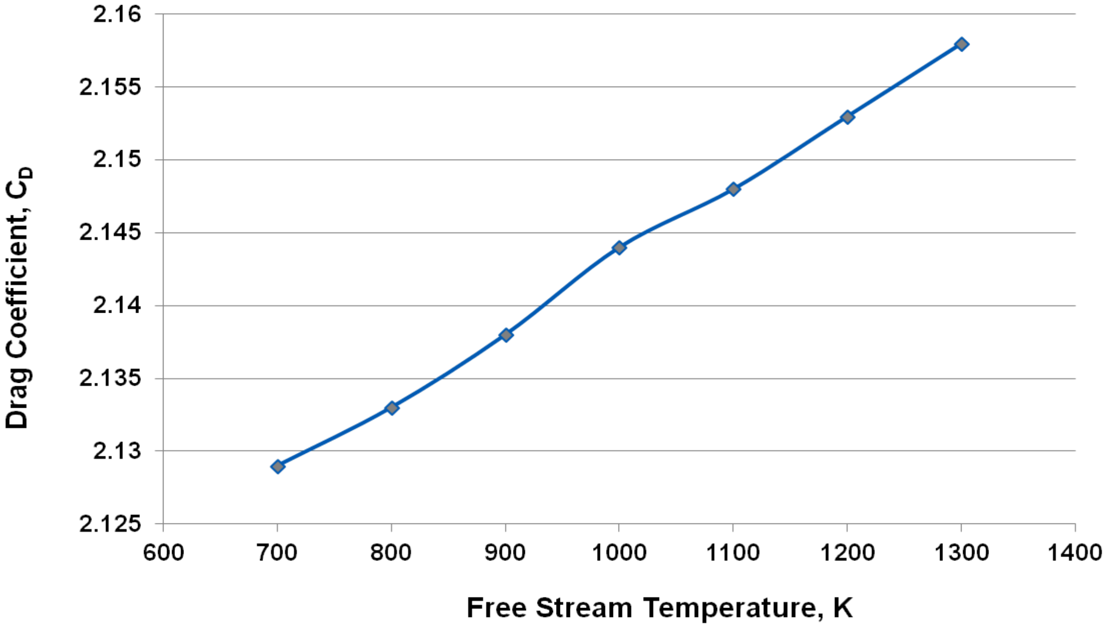

Figure 4: Variation of drag coefficient of a sphere with free-stream temperature

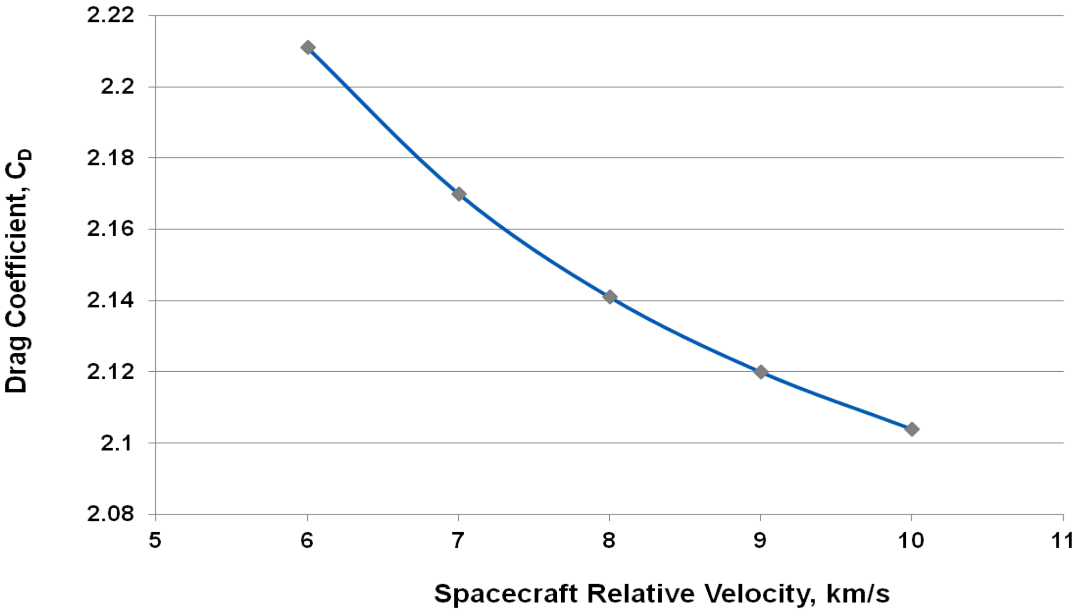

Figure 5: Variation of drag coefficient of a sphere with spacecraft relative velocity

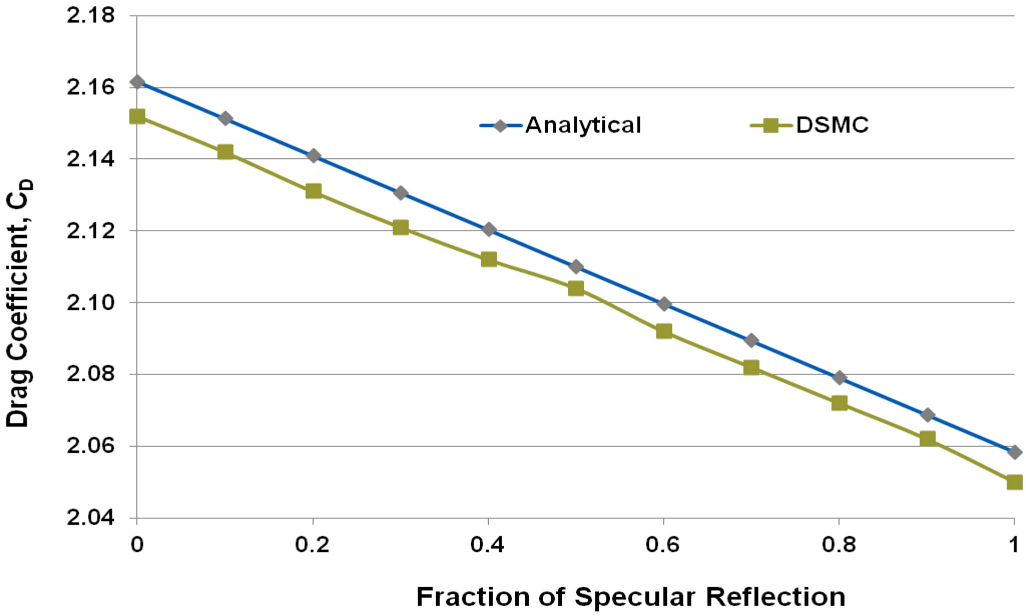

Figure 6: Ability of DS3V to simulate quasi-specular reflections

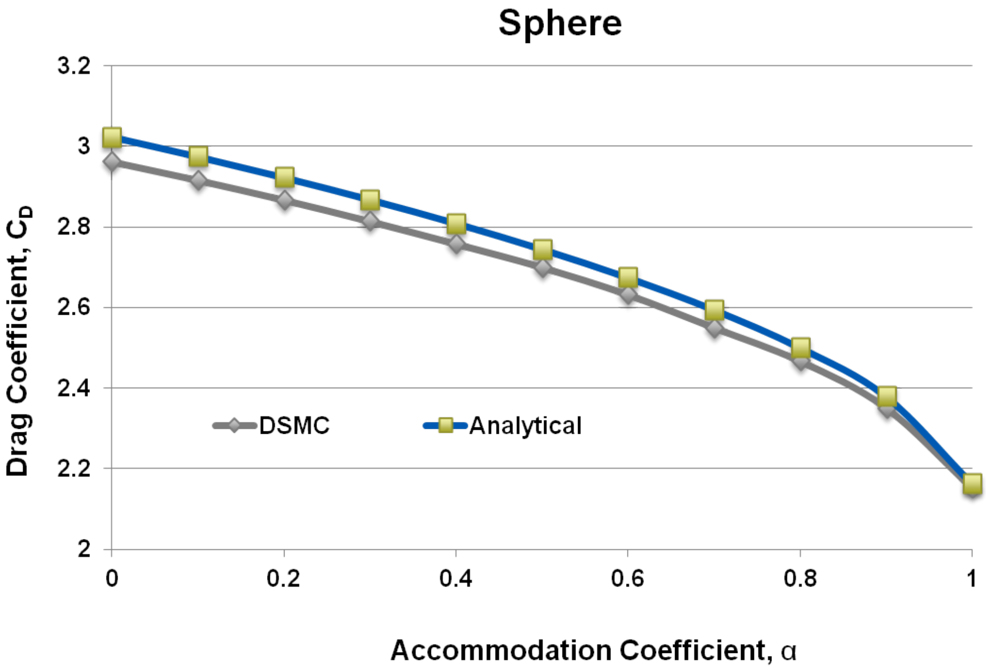

Figure 7: Variation of drag coefficient of a sphere with accommodation coefficient

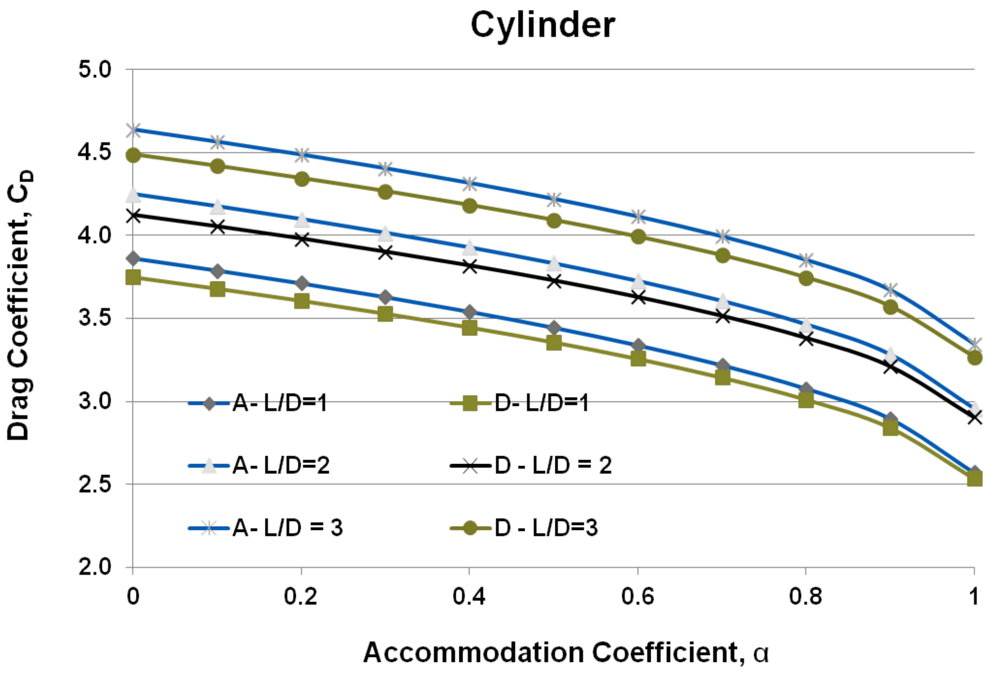

Figure 8: Variation of drag coefficient of a Cylinder in arrow orientation with accommodation coefficient (Legend: A=Analytical, D=DSMC)

4. Conclusions

The effectiveness of the Direct Simulation Monte Carlo (DSMC) technique and the ability of the DS3V code in computing drag coefficients for satellites in low-Earth orbit has been successfully examined. Results show a small difference in drag coefficients for a sphere and a cylinder computed using analytical equations and the DSMC technique. Therefore, the DS3V code, inspite its limitations, does well in explicitly computing drag coefficients.

For future work, the DS3V needs to be validated using complex geometries like CHAMP and GRACE. Once validated, the technique can be used to develop drag coefficient models for simple as well as complex geometry satellites. This will allow for accurate density derivation for assimilation into density models as well as reduced satellite conjunction errors.

5. Acknowledgements

The author would like to thank the Los Alamos National Laboratory, the selection committe and all other parties involved for the opportunity to be a part of the Space Weather summer school. The author would also like to thank the funding sources, namely, the Los Alamos Institute of Geophysics and Planetary Physics (IGPP), the Laboratory Directed Research and Development Office (LDRD) and the Center for Information Science and Technology for the prestigious Vela fellowship. Special thank to Balu Nadiga and Mike Shoemaker, for their guidance and the insightful conversations and to all the faculty that lectured on the cool and interesting topics.

6. Bibliography

Bird, G. A., Molecular Gas Dynamics and the Direct Simulation of Gas Flows, Oxford Science Publication, New York, 1994.

Bird, G. A., Visual DSMC Program for Three-Dimensional Flows: The DS3V Program Users Guide, G.A.B Consulting Pty Ltd, Version 2.5, October 2006.

Bowman, B. R., Moe, K., Drag coefficient variability at 175-500 km from the orbit decay analysis of spheres, Paper AAS 2005-257, American Astronautical Society Publications Office, San Diego, CA, 2005.

Brown, C. D., Elements of Spacecraft Design, AIAA Education Series, American Institute of Aeronautics and Astronautics, Inc., Reston VA, 2002.

Hedin, A. E., Hinton, B. B., Schmitt, G. A., Role of gas-surface interactions in the reduction of Ogo 6 neutral particle mass spectrometer data, Geophys. Res. 78, 4651-4668, 1973.

Kostoff, R.N. Anderson, J.B., Fenn, J.B. Measurements of momentum accommodation of gas molecules at surfaces. In H. Saltsburg, J. N. Smith, and M. Rogers, editors, Fundamentals of Gas-Surface Interactions, Symposium, San Diego, Dec. 1966, pages 512521. Academic Press, New York., 1967.

Marcos, F.A., Burke, W.J., Lai, S.T., ”Thermospheric Space Weather Modeling,” AIAA 2007-4527, 38th AIAA Plasmadynamics and Lasers Conference, Miami, FL, 25-28 June, 2007.

McLaughlin, C. A., Hiatt, A., and Lechtenberg, T., Precision Orbit Derived Total Density, Journal of Spacecraft and Rockets, Vol. 48, No. 1, January-February, 2011, pp. 166-174.

Moe, M. M., Moe, K., The roles of kinetic theory and gas-surface interactions in measurements of upper-atmospheric density. Planet. Space Sci. 17(5), 917-922, 1969.

Moe, M.M., Wallace, S. D., Moe, K. Recommended drag coefficients for aeronomic satellites, in The Upper Mesosphere and Lower Thermosphere, AGU Monograph 87, American Geophysical Union, Washington, 1995.

Moe, K., Moe, M. M., and Wallace, S. D., Improved Satellite Drag Coefficient Calculations from Orbital Measurements of Energy Accommodation, Journal of Spacecraft and Rockets, Vol. 35, No. 3, 1998, pp. 266-272.

Moe, K., Moe, M. M., and Doornbos, E., Outstanding Issues related to Thermospheric Measurements and Modeling, ($http : //spaceweather.usu.edu/files/uploads/PDF/Outstanding_Issues.pdf$), 2012.

Pardini, C., Anselmo, L., Moe, K., Moe, M. M., Drag and energy accommodation coefficients during sunspot maximum, Adv. Space Res., 45, 638-650, 2010.

Pilinski, M., Argrow, B., and Palo, S., Semi-Empirical Model for Satellite Energy Accommodation Coefficients, Journal of Spacecraft and Rockets, Vol. 47, No. 6, November-December 2010, pp. 951-956.

Pilinski, M., Argrow, B., and Palo, S., Drag Coefficients of Satellites with Concave Geometries: Comparing Models and, Journal of Spacecraft and Rockets, Vol. 48, No. 2, March-April 2011, pp. 312-325.

Schamberg, R. A., New Analytic Representation of Surface Interaction for Hyperthermal Free Molecular Flow, Rand Corporation, TR RM-2313, 1959.

Sentman, L. H., Free Molecule Flow Theory and its Application to the Determination of Aerodynamic Forces, Lockheed Missile and Space Co. Sunnyvale, CA, TR LMSC-448514, AD 265-409, 1961.

Stickney, R. E. and Hurlbut, F. C., in Rarefied Gas Dynamics, Third Symposium, Academic Press, N.Y., 1963.

Storz, M.F., Bowman, B.R., and Major Branson, J.I., High Accuracy Satellite Drag Model, AIAA 2002-4886, AIAA/AAS Astrodynamics Specialist Conference and Exhibit, Monterey, CA, 5-8 August 2002.

Wright, J. R., Real-Time Estimation of Local Atmospheric Density, Advances in the Astronautical Sciences, Vol.114, AAS 03-164, Univelt, 2003, pp. 927-950.

Wright, J. R., and Woodburn, J., Simultaneous Real-Time Estimation of Atmospheric Density and Ballistic Coefficient, Advances in the Astronautical Sciences, Vol. 119, AAS 04-175, Univelt, 2004, pp. 1155-1184.

Determining Source Rate Parameters of Energetic Electrons in the Outer Radiation Belt using a Kalman Filter

Quintin Schiller

Laboratory for Atmospheric and Space Physics, University of Colorado, 1234 Innovation Dr., Boulder, CO 80303

Humberto Godinez

Los Alamos National Laboratory, Los Alamos, NM 87544

Abstract

Data assimilation methods are becoming increasingly popular to describe the observationally sparse environment in Earth's magnetosphere. As energetic electrons pose a number of hazards to manned and unmanned spacecraft, the outer radiation belts are an especially high profile candidate for data assimilation techniques. Energetic electron diffusion can be simplified with a Fokker-Plank equation, which also allows for the ability to include loss or source terms. We use a one-dimensional radial diffusion model and a conventional Kalman filter (CKF) to describe the energetic electron PSD for the full radial range of the outer radiation belt. Additionally, we augment the state vector to include the magnitude of a Gaussian-shaped local acceleration term. The result of the analysis is an estimate of electron PSD, as well as a time-dependent heating rate for specified location and width. To further constrain the source rate parameters, such as the location and width of the acceleration region, additional analysis is performed using the observational residual vector (or innovation vector) by quantifying the root mean square (RMS) of the vector in a location-width parameter space. We prove the functionality of the innovation vector RMS method with three identical twin experiments, in which the method proves robust and is able to reproduce the synthesized source rate parameters and PSD. We then apply the method to real spacecraft observations, consisting of a five satellite Phase Space Density (PSD) dataset (three LANL-GEO, one GPS, and POLAR) for constant first and second adiabatic invariants, $\mu = 2083[\mathrm{MeV/G}]$ and $\mathrm{K} = 0.03\ [\mathrm{G}^{\frac{1}{2}}\mathrm{R_E}]$. In a data denial experiment, we show that the intensity of local heating is robust to removing satellites from the dataset. Using the satellite observations we estimate the PSD and full source rate term (including amplitude, location, and extent of the local heating) for the entire period. Finally, we attempt to find a correlation between the plasmapause location and the location of local heating. However, a concrete correlation will require further investigation.

---

1. Introduction

The outer electron radiation belt, or outer Van Allen belt, is a donut-shaped region in near-earth space populated by relativistic electrons which are trapped in Earths magnetosphere. The belt is restricted to a region between 3∼7 Earth radii ($\mathrm{R_E}$), with peaks in flux just inside of geosynchronous orbit (GEO), or near 5 $\mathrm{R_E}$.

The energetic electrons pose a number of hazards to manned and unmanned spacecraft(1) and overlap commonly used orbits, such as low-Earth, Global Positioning System (GPS), and GEO. The system is extremely dynamic and undergoes continuous change by various complex and not fully-understood processes, such as localized heating (source), loss, and radial transport(18).

Yet, each individual process is difficult to quantify its unique contribution to the net electron flux. Spacecraft that make in-situ observations to measure the total electron flux cannot observe individual processes that occur, and thus cannot distinguish which processes contribute to the total electron flux. In short, the balance between all three

---

Email addresses: `quintin.schiller@colorado.edu` (Quintin Schiller), `hgodinez@lanl.gov` (Humberto Godinez)

Los Alamos Space Weather Summer School 2012

processes is not well understood. Further complications arise from the restricted, single-point in-situ measurements taken by spacecraft. The measurements have limited temporal and spatial coverage, resulting in an undersampled system, and often the measurements have large uncertainties associated with them.

Attempts to model the electron radiation belt have been met with limited success. The limitations are due to inaccurate estimates of the source, loss, and transport processes occurring in the system. Improvements on, for example, the source term, would lead to drastic improvements on the overall understanding of the system. However, current models are missing accurate and realistic source terms. Our objective in this paper is to use data assimilation techniques to provide a concrete estimate of the source term. Specifically, we use a conventional Kalman filter (briefly described in Sections 2 and 3) to estimate the magnitude, location, and width of a Gaussian source term to best match observational data. We then verify the functionality of our method in Section 4, and use the approach with real satellite data in Section 5.

2. Model

We use a one-dimensional Fokker-Plank equation to describe radial diffusion in L for the energetic electron population in the outer radiation belts in phase space density (PSD) coordinates (for further discussion of phase space and PSD coordinates, see Chen et al.; 2005; 2006 (7; 8)

$$\frac{\delta f}{\delta t} = L^2 \frac{\delta}{\delta L}\left(\frac{D_{LL}}{L^2}\frac{\delta f}{\delta L}\right) - \frac{f}{\tau} + S$$

where $D_{LL}(L,t)$ is the radial diffusion coefficient, $\tau(L,t)$ is the loss timescale, and $S(L,T)$ is the source rate. We assume a Gaussian form for the source rate

$$S = Ae^{-\frac{(L-L_C)^2}{\sigma^2}}$$

where the source location is centered at L_C and has width σ and amplitude A. A Gaussian source term such as this exists over all values in L and does not introduce artificial discontinuities which might arise in a step-like source function.

We select a Kp dependent diffusion coefficient (6)

$$D_{LL}(Kp, L) = 10^{(0.506Kp-9.325)}L^{10}$$

where Kp is an proxy for geomagnetic activity. We select three L-dependent loss timescales

Loss Mechanism	Region	Location	Loss Timescale
Plasmaspheric Hiss	Inside Plasmasphere	$\mathrm{L} < \mathrm{L}_{PP}$	$\tau = 8$ days (17)
Chorus Waves, etc.	Outside Plasmapause	$\mathrm{L_{PP}} \leq \mathrm{L} < \mathrm{L_{MAX}}$	$\tau = \frac{3}{\mathrm{Kp}}$ (17; 30)
Magnetopause Shadowing	Outside Last Closed Drift Shell	$\mathrm{L} > \mathrm{L_{MAX}}$	$\tau = \frac{1}{2}\times$Drift Period (=10 min.)

where $\mathrm{L_{PP}}$ corresponds to the location of the plasmapause ($\mathrm{L_{PP}(Dst)} = -1.57\log_{10}(\mathrm{min}_{-24,0}\mathrm{Dst})$; where $\mathrm{min}_{-24,0}\mathrm{Dst}$ represents the minimum Dst value from the past 24 hours(23)) and $\mathrm{L_{MAX}}$ corresponds to the last closed drift shell as described in Koller and Morley [2010](16), $\mathrm{L_{MAX}(Dst)} = 6.07\times10^{-5}\mathrm{Dst}^2 + 0.0436\mathrm{Dst} + 9.37$. The inner and outer boundaries, L=2 and L=10, are set to $1\times10^{-16}\left(\frac{\mathrm{c}}{\mathrm{MeV\,cm}}\right)^3$.

To solve the Fokker-Plank equation we use the Crank-Nicolson method (9), which is unconditionally stable and 2nd order accurate and does not need to satisfy the Courant condition (24). We select a ΔL of 0.25, comprising 32 grid points from $2\leq \mathrm{L} \leq 10$. The initial condition is a Gaussian fit to the average of the first 20 hours of GEO data.

The resulting PSD is, in reality, a balance between radial transport, source, and loss for a specific first and second adiabatic invariant (μ and K respectively) combination. For a discussion on adiabatic invariants, such as μ and K, see Roederer [1970] (26). While we assume particular loss and diffusion timescales for this analysis, our results for both the source term and for the PSD are convolved with the balance all three processes: diffusion, loss, and source. Neither the actual observations, nor the model as we present it, can distinguish between the various processes at work, but only the net result of all processes in combination. Furthermore, the source rate term in our model can have a negative value. In this case, the parameterized loss is insufficient to describe the PSD and the model uses a negative source rate to supplement the loss. When the source rate has a positive value, it may indicate an enhancement of acceleration mechanisms or a suppression of loss processes.

3. Kalman Filter

For a description of the Kalman filter, we turn the reader to Kalman [1960] (14), where the methodology of the filter is detailed. Furthermore, for relevant applications of the Kalman filter in studies of the radiation belts, we point the reader toward papers by Bourdarie(4; 5), Daae(10), Koller(15), Kondrashov(17), Maget(19), Naehr and Toffoletto(20), Ni(21; 22), Reeves(25), and Shprits(28; 29).

Important variables are 1) The state vector, x. The first 32 components of the state vector are PSD from L=2 to L=10. The 33rd component is A, the amplitude parameter of the source term as described in Equation 2. As the model, Equation (1), is linear in S, we simply augment the state vector with the amplitude parameter, A. 2) The model covariance propagating matrix, $\mathbf{Q}$. This variable represents degradation in the accuracy of the model as time progresses without observations to update the state vector. For our case, we use $\mathbf{Q} = \varepsilon_m \mathbf{I} \times \left[x_i^f - x_i^a\right]$, where ε_m is the uncertainty of the model. While ε_m is very difficult to quantify, we ambiguously set it to 300%, as we are far less confident in the model than the observations, and 300% is 10× the model uncertainty (see below). f and a represent where in the Kalman filter the state vector is taken from, f representing the forecast step, and a representing the analysis step. i stands for the time step of operation and $\mathbf{I}$ is the identity matrix. The value of the model covariance propagating matrix, $x_i^f - x_t^a$, is a good representation of how well the model's forecast reproduces the observations at the next time step. Large (small) values indicate poor (good) performance, and the confidence in the model will decrease (increase). 3) The observation covariance matrix, $\mathbf{R}$, which is defined as $\mathbf{R} = \varepsilon_o \mathbf{I} \times y_i$, where y is the observation vector and consists of the observations available for time step i. Analysis done by Koller et al. [2007] describes the uncertainty in the observations for a similar dataset to be 30% of the measured PSD (15), thus we choose 30% for ε_o, the uncertainty of the observations.

The augmented state vector is capable of estimating electron PSD and the intensity of local heating for a region with specified, and non-changing, location and width. However, these terms are physically dynamic and change on timescales comparable to individual storms. To constrain these parameters 'offline', or outside of the Kalman filter algorithm, we employ the innovation vector (or observation residual), $\left(y_i - \mathbf{H}_i x_i^f\right)$, which represents the residual between the observations and the model forecast state. The root mean square (RMS) of the innovation vector is defined as

$$\mathrm{RMS_{INNOVATION}} = \sqrt{\frac{1}{m}\sum_{i=1}^{T}\left(y_i - \mathbf{H}_i x_i^f\right)^2}$$

where T is the total number of times steps for the period and m is the number of observations. A high (low) innovation vector RMS indicates that the model, including the source rate parameters selected, less (more) accurately predicts the actual observations. The most desirable innovation RMS is close to zero, as that establishes the location/width combination that best reproduces the satellite measurements. An example of the results for a parametric study or constant source rate parameters (amplitude, location, and width), can be seen in Figure 1. The method of our studies is to run the Kalman filter multiple times, each with a unique source location and width, and observe the innovation vector RMS. Schiller et al.(27) have previously performed work on this topic.

The filter is allowed a three day spin up period to generate a state which is not dependent on the initial conditions, and then the innovation vector analysis is performed for the subsequent day. The result is an 'online' estimate (with time resolution equal to the resolution of the filter - 120 minutes) of the source rate amplitude, and 'offline' estimates (with resolution equal to the length the filter is run for - one day) of the location and width parameters. We argue that where the global minimum is in the location-width parameter space represents the dimensions of the physical processes occurring over that period. First, we verify the method using identical twin experiments.

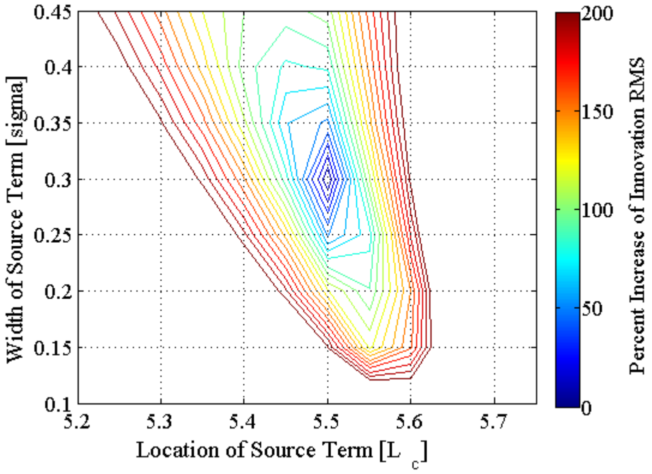

Figure 1: A model run for a simple case: a source rate term with constant amplitude, constant width (y-axis) of 0.3, and constant location of L = 5.5. The parameter space of location and width contains a large spectrum of innovation vector RMS (colored contour lines), but there is a clear minimum at width = 0.3 and location = 5.5, the correct source rate parameters for this example.

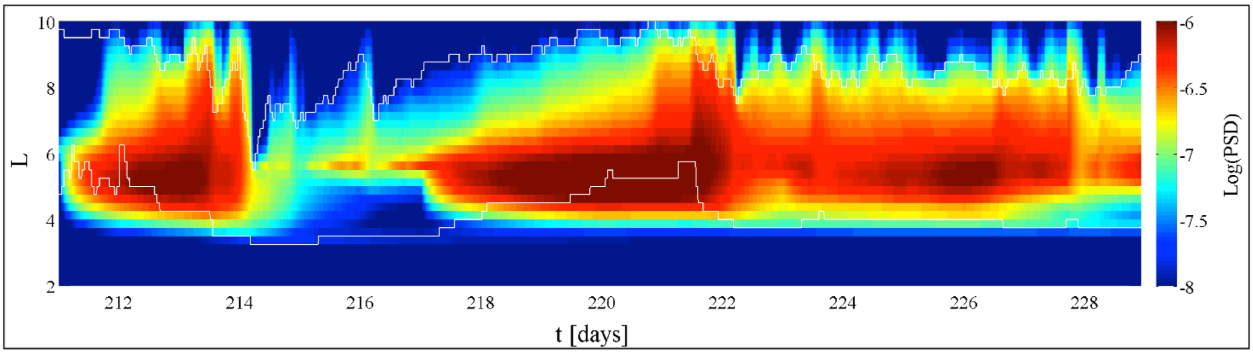

Figure 2: The synthesized data, which 'observations' are sampled from (4), and which the model estimates.

4. Identical Twin Experiments

The following identical twin experiments are a continuation of the work done by Schiller et al.(27). For this part of our study, we run identical twin experiments to prove the functionality of the model. The first step of the experiment is to synthesize a dataset to act as the 'true' data the model is trying to recreate (see Figure 2). In this case, there is a source term included which has constant amplitude, but changes in width and location every 3 days (Figure 3). Observations are taken of the 'true' data with ±10% error included (Figure 4). The observations are an attempt to recreate a hypothetical satellite in an idealized orbit flying through the radiation belts. Using the method described above, we attempt to recreate both the PSD for the full radial range as well as the amplitude, location, and width of the source term. The results can be seen in Figure 5.

We choose the source location to vary minimally, never by more than 0.4L, to verify the method works even during potentially 'worst-case' scenarios, where the filter would have difficulty distinguishing small variations in the parameters. The results confirm that our method works to estimate the amplitude of a constant source rate term, as well as accurately estimates the location and width. To determine the robustness of the method to more extreme gradients in the source term, we perform the same analysis for a source term that changes in intensity every three days by up to a factor of 3. A visualization of the synthesized term for this experiment can be seen in Figure 6, and the

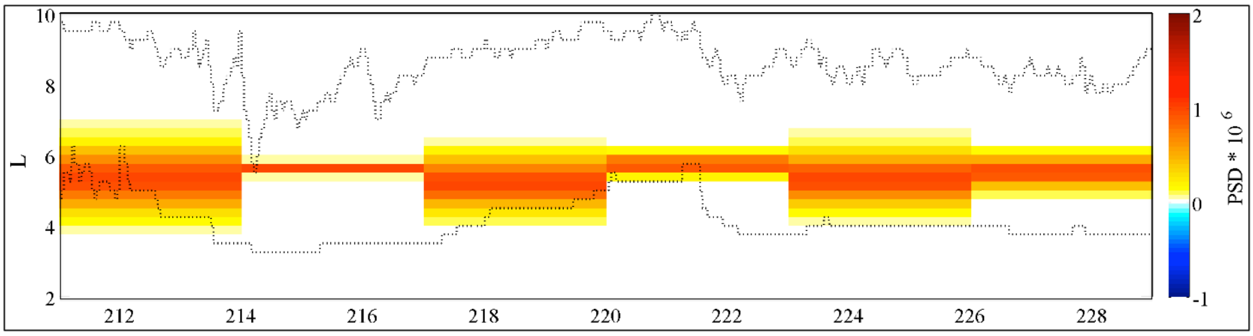

Figure 3: A visualization of the source rate. In this case, the amplitude is set to constant (1×10^{-6}) for the full period, but the location and width change every three days.

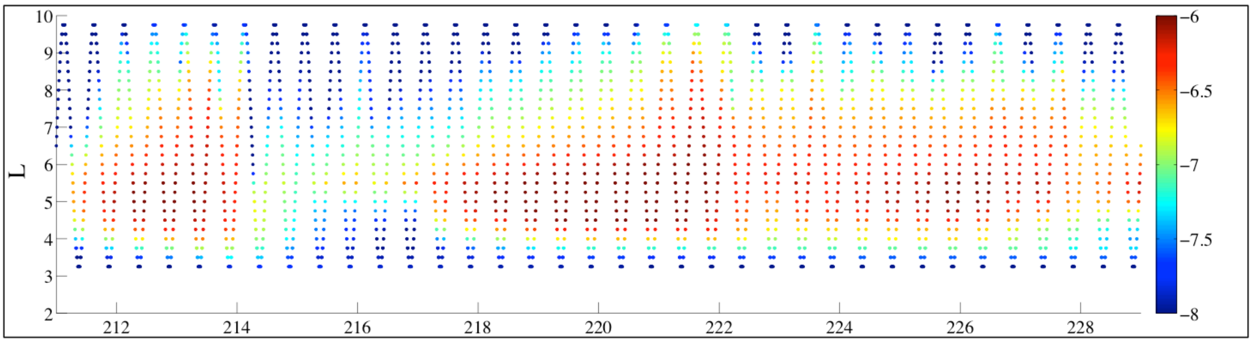

Figure 4: The sampling from the 'true' data (2), with ±10% error included, which are used as observations in the model

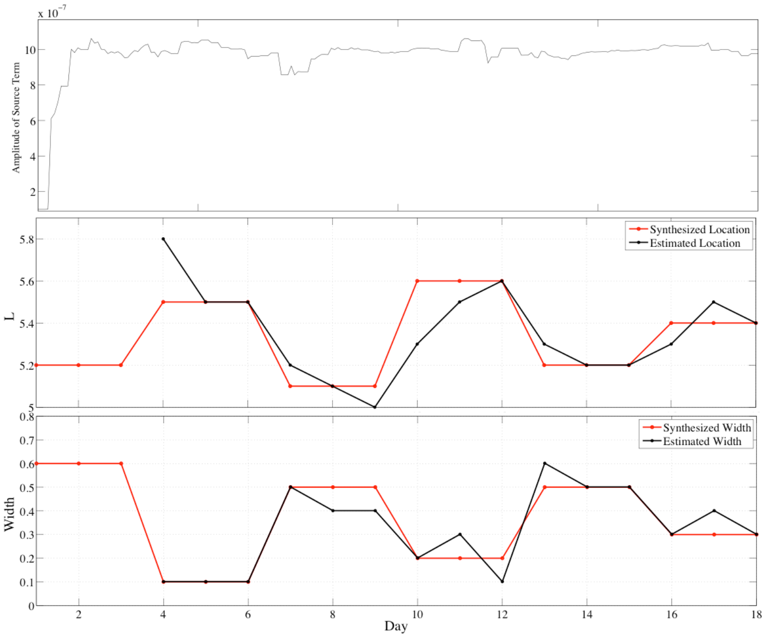

Figure 5: Results of the identical twin experiment - estimates of source rate parameters.

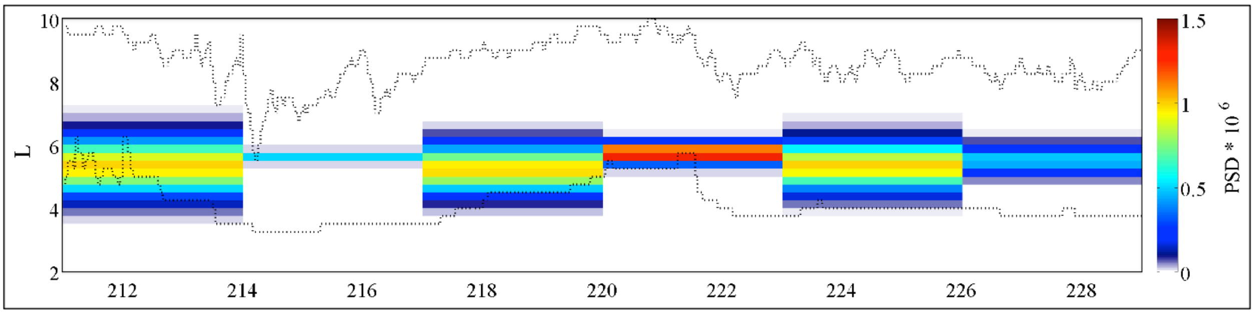

Figure 6: A visualization of the entire source term with variable amplitude. The amplitude varies from 0.5e-6 to 1.5e-6.

estimated source rate parameters can be seen in Figure 7.

The results are very similar to the previous results. However, there is ~1 day delay for the amplitude estimate to converge on the correct value. These results agree to Daae et al. [2011], who find that the model 'forgets' previous states in approximately one day. More specifically, the difference between two models with drastically different initial conditions is reduced to %15 after one day. These results confirm that the method is valid for local heating which varies in time. However, heating rate that varies by no more than a factor of three is not physical. In the next experiment, the intensity of local heating varies by two order of magnitude - a scenario that is more likely to be observed in the magnetosphere. The source rate term can be seen in Figure 8, and the estimates of the source rate parameters in Figure 9.

The results for this experiment are more scattered than previous results. Generally, the model performs well with some minor exceptions. First, it takes ~2.5 days to converge to the largest amplitude, whereas closer to one day for the others. Second, when the maximum source rate lowers by an order of magnitude, the subsequent estimate of location and width is far less accurate. This is likely due to the strong gradients which occur as the high levels of PSD diffuse radially and saturate the source term, as can be seen in Figure 10. Finally, the final period (days 16-18) is decidedly the least accurate estimate of source location and width. Similar to the second point, this is likely due to the high levels of PSD which occur in the source region during this period, which originate from the period of highest source intensity (days 10-12) and continue through days 13-15. The high PSD mask any source that is occurring, and the high PSD gradients from radial diffusion (as opposed to local heating) make it difficult for the filter to distinguish the relative contribution of local heating.

The large absolute PSD and steep PSD gradients result in poor estimates of location and width for the last period in the study. We suspect that, given a few more days for the PSD to diffuse away and be lost to the boundaries, the filter would converge to the correct values of location and width, as it did for a similar period of low source rate during days 4-6. However, despite the inaccuracies involved with estimates of source rate term parameters, the filter is able to accurately estimate the PSD for the entire period, as seen in Figure 11. These experiments prove that the method of innovation vector RMS in a parameter space is capable of reproducing not only parameters in the state vector, but also parameters estimated 'offline', such as source rate location and width.

5. Applications to Real Data

As seen in the previous section, the method estimates all three parameters for a Gaussian-shaped source rate term - amplitude, location, and width - is also capable of reproducing synthesized PSD, both for a synthesized dataset. The next step is to apply this method to real satellite observations. The observations themselves are described in the following subsection, followed by a brief study to determine the robustness of the Kalman filter to different satellite observations, and finally the results of the method applied to the satellite PSD dataset.

5.1. PSD Observations

The data used in the assimilation process is a PSD dataset provided by Yue Chen at Los Alamos National Lab(7; 8). It consists of particle measurements from five spacecraft: three LANL-GEO (97a, 1991-080, 1990-095), one

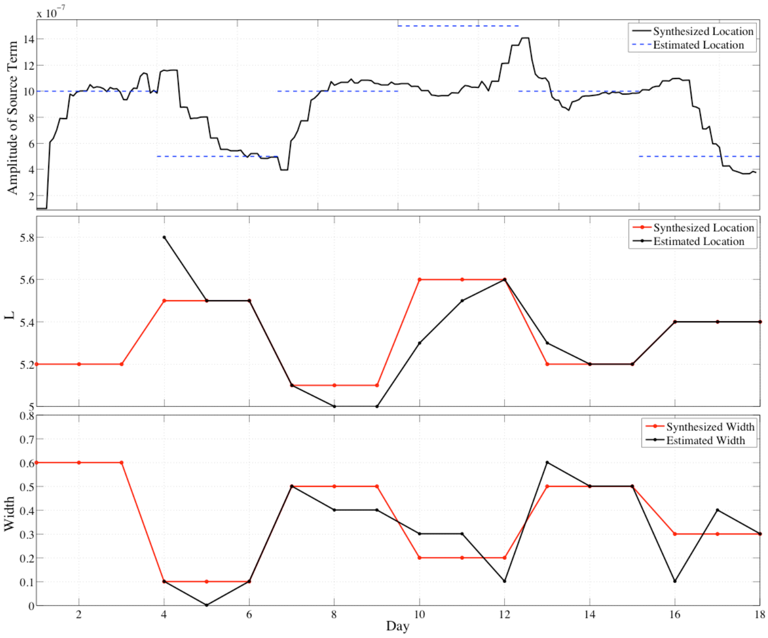

Figure 7: Estimate of source term parameters for the identical twin experiment with variable source rate amplitude as seen in Figure 6. The top panel shows the actual source rate amplitude in blue and the estimate of the parameter in black. The middle and bottom panels show the actual source term location and width, respectively, in red and the estimate of the terms in black.

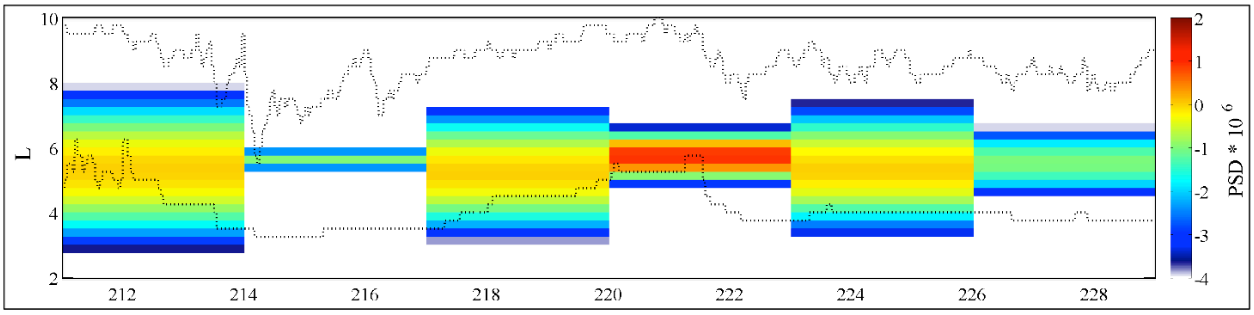

Figure 8: The entire source term with variable amplitude. The amplitude varies from 0.1e-6 to 10e-6. The label on the colorbar axis should read log$_1$0(PSD*10^6).

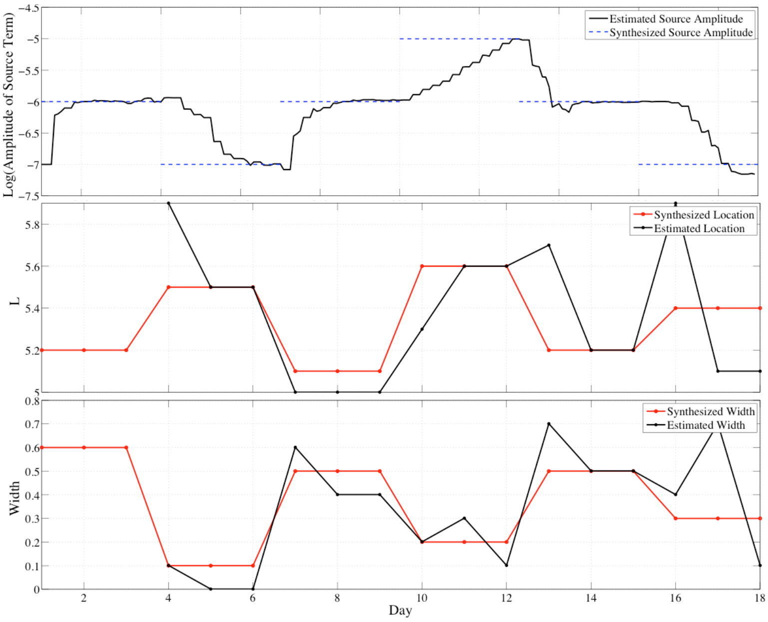

Figure 9: Estimate of source term parameters for the identical twin experiment with variable source rate amplitude as seen in Figure 6. The top panel shows the actual source rate amplitude in blue and the estimate of the parameter in black. The middle and bottom panels show the actual source term location and width, respectively, in red and the estimate of the terms in black.

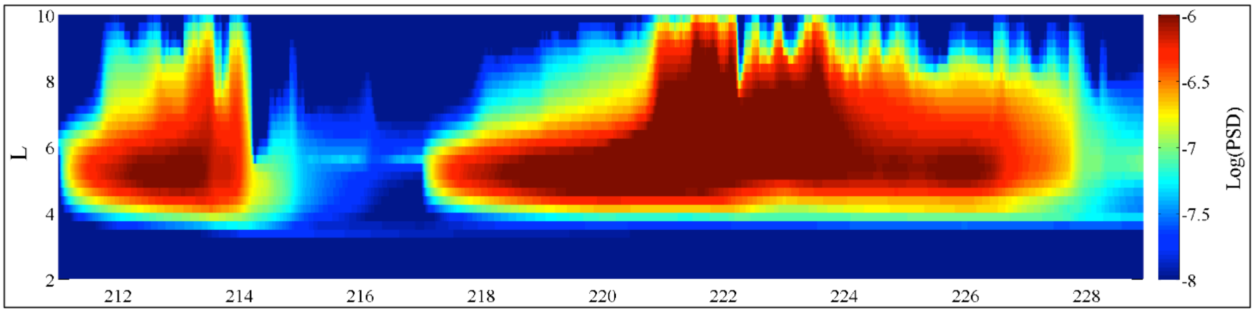

Figure 10: Synthesized data from the identical twin experiment which includes the source term which varies by two orders of magnitude.

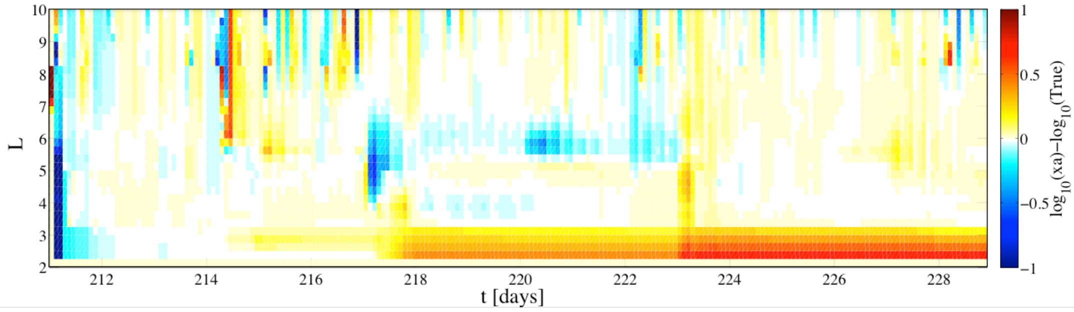

Figure 11: The difference between the log of the PSD estimate and the log of the true PSD state, with source rate from Figure 8 included.

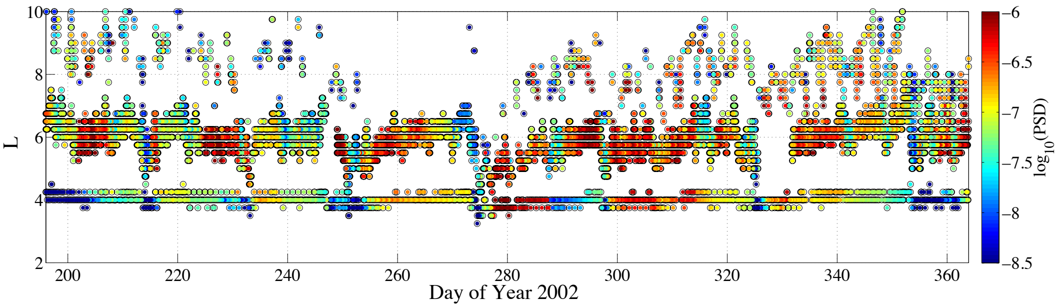

Figure 12: The full dataset in consideration, including observations from three LANL-GEO, POLAR, and a GPS spacecraft.

Global Positioning System (GPS-ns41), and POLAR. The particle detectors onborad the satellites are: LANL-GEO - Synchronous Orbit Particle Analyzer (SOPA) instrument (2), GPS - Burst Detector Dosimiter (BDD) II (11), and POLAR - Comprehensive Energetic Particle and Pitch Angle Distribution Experiment (CEPPAD) (3). In total, 87 days of data are available from June 30th to October 24th, 2002. Data from all spacecraft are averaged to the center of each discrete mesh grid point with dimensions 0.25[L] x 120[min]. The conversion from flux to PSD is done for constant first and second adiabatic invariants, $\mu = 2083[\mathrm{MeV/G}]$ and $\mathrm{K} = 0.03[\mathrm{G}^{\frac{1}{2}}\mathrm{R_E}]$ respectively, and is performed in two steps following Chen et al. [2005, 2006] (7; 8) and Hilmer et al. [2000] (12). These particles correspond to 1 MeV at GEO. The entire dataset can be seen in Figure 12.

5.2. Data Denial Experiments

A very brief study was conducted to determine the affect different satellites have on the overall PSD estimate of the state space. To conduct this experiment, a period from DOY 211 to 233, 2002 was reanalyzed with the augmented state space vector (to estimate the amplitude of the source rate term). The location was set to L=5.5, with width set to 0.3. These parameters were constant over the interval. A comparison was done between the reanalysis using all satellite observations; the reanalysis using only POLAR and GEO spacecraft (Figure 14); and the reanalysis using POLAR, the GPS spacecraft, and two of the three GEO spacecraft (Figure 13). The results for each are as expected: the larges differences in PSD occur where the data from the absent spacecraft is no longer available.

For the data denial experiment with the GEO spacecraft removed, the differences occur between the GPS observations and the magnetopause. The largest differences occur between DOY 225 and 230, during an enhancement in the radiation belts. During this time, the differences are magnified when 97A provided the only data for a particular observation time step, or when 97A observed significantly different PSD than the other GEO spacecraft for the same observation time step. This might be due to anisotropies in the electron drift population (where one GEO spacecraft will see high PSD, while other GEO spacecraft will be in regions of low PSD), localized acceleration occurring preferentially closer to one of the GEO spacecraft, injections of electrons from the tail region, or other physical or numerical causes. The variations in PSD can reach two orders of magnitude during this period of enhanced radiation belt intensities.

The experiment with data from the GPS spacecraft removed reveals similar results. The differences occur where the GPS spacecraft makes its observations, between L=4~5. The largest differences occur during the same period of enhanced radiation belt intensities - DOY 225 to 230. However, the analysis with the GEO spacecraft removed sometimes over-predicted and sometimes under-predicted the PSD. The results of the analysis with the GPS data removed show consistent under-predicting during the period before the enhancement, and consistent over-predicting during the enhancement. This suggests that the GPS data was pulling the state vector up in the days before, and pulling the state vector down during the enhancement. Variations for this experiment also ranged to two orders of magnitude.

Whereas the previous studies observed the changes in PSD from the removal of one of the satellites in the dataset, a different analysis was performed to measure the effects on the estimate of the source rate amplitude. This analysis was performed for five consecutive periods during the interval from DOY 211 to 297, 2002, each with different source location and widths (as outlined in Schiller et al. [2012]). The results of this experiment can be seen in Figure 15.

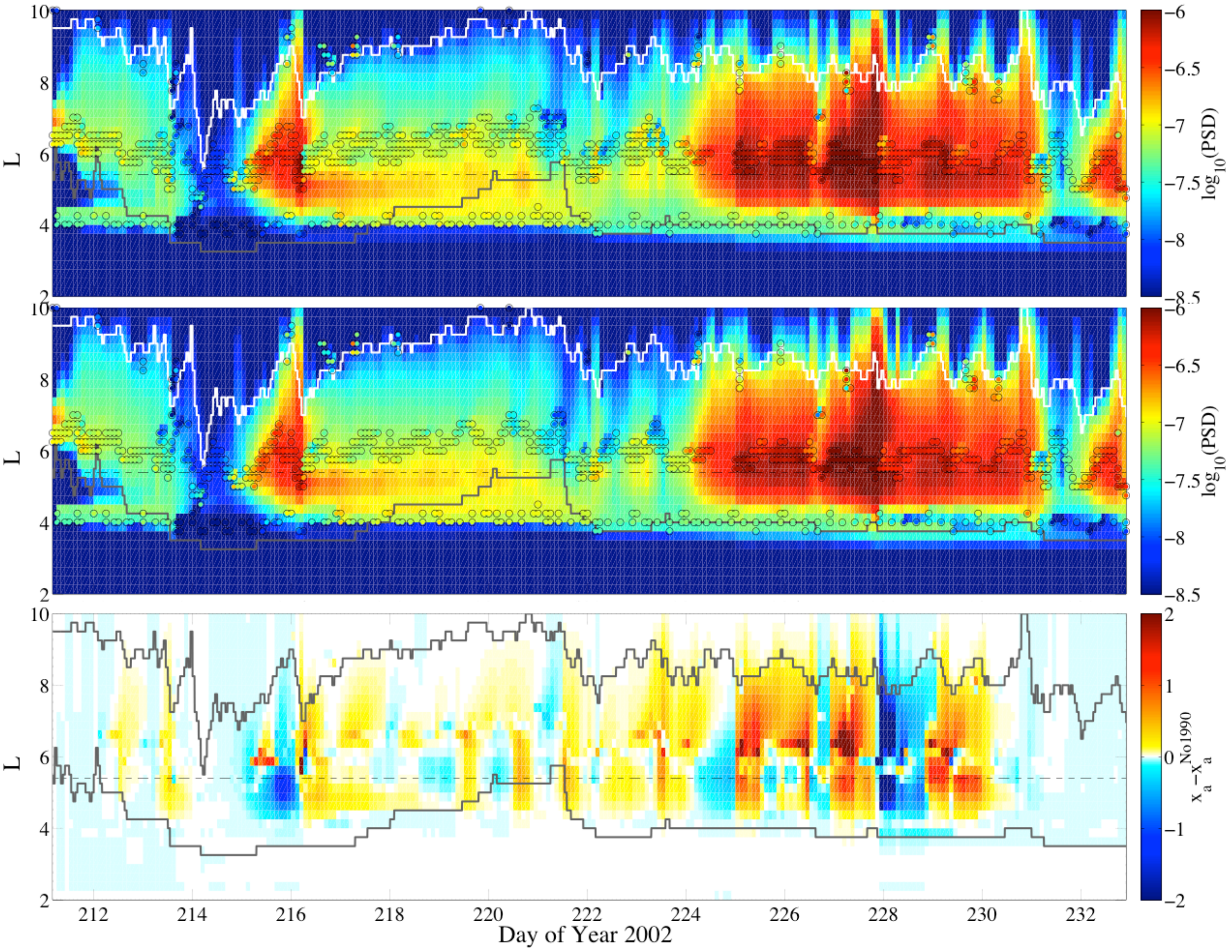

Figure 13: Top panel: Reanalysis with observations from all five spacecraft. Middle panel: Reanalysis performed with all observations except LANL-GEO 97A. Bottom panel: The log difference between the the two reanalyses. The dashed line corresponds to the location of the estimatable source term.

Despite the variations in PSD estimate, the estimate of the source rate amplitude is relatively unaffected by the removal of either dataset. The basic structure and magnitudes are preserved for all three cases. These results suggest that the PSD is sensitive to the data included in the observations, whereas the estimate of some source rate parameters is robust to data denial.

5.3. Application of Method to Real PSD Observations

We apply the methods described in the previous sections, namely Section 4, to the real dataset described in Section 5.1. The results are depicted in Figure 16. The authors warn the reader that the PSD estimate near DOY 280 may not be physical, as there are only a few examples of high energy electrons penetrating into the slot region (below L=2-3). It is likely that the high PSD in the slot region is a result of numerics, as the source location is estimated to be very low: between L=3 and L=4 for multiple days. Such a source term could numerically populate the slot region as there are no observations inside of L=4 to decrease the filters estimate of PSD there. Despite this potential issue, the reanalysis agrees strongly with the observations. The comparison between the two can be seen in Figure 18. The vast majority of the observations are recreated within a factor of two. The largest differences between the reanalysis and the observations occur near the outer boundary, where we assume all particles are lost to the magnetopause.

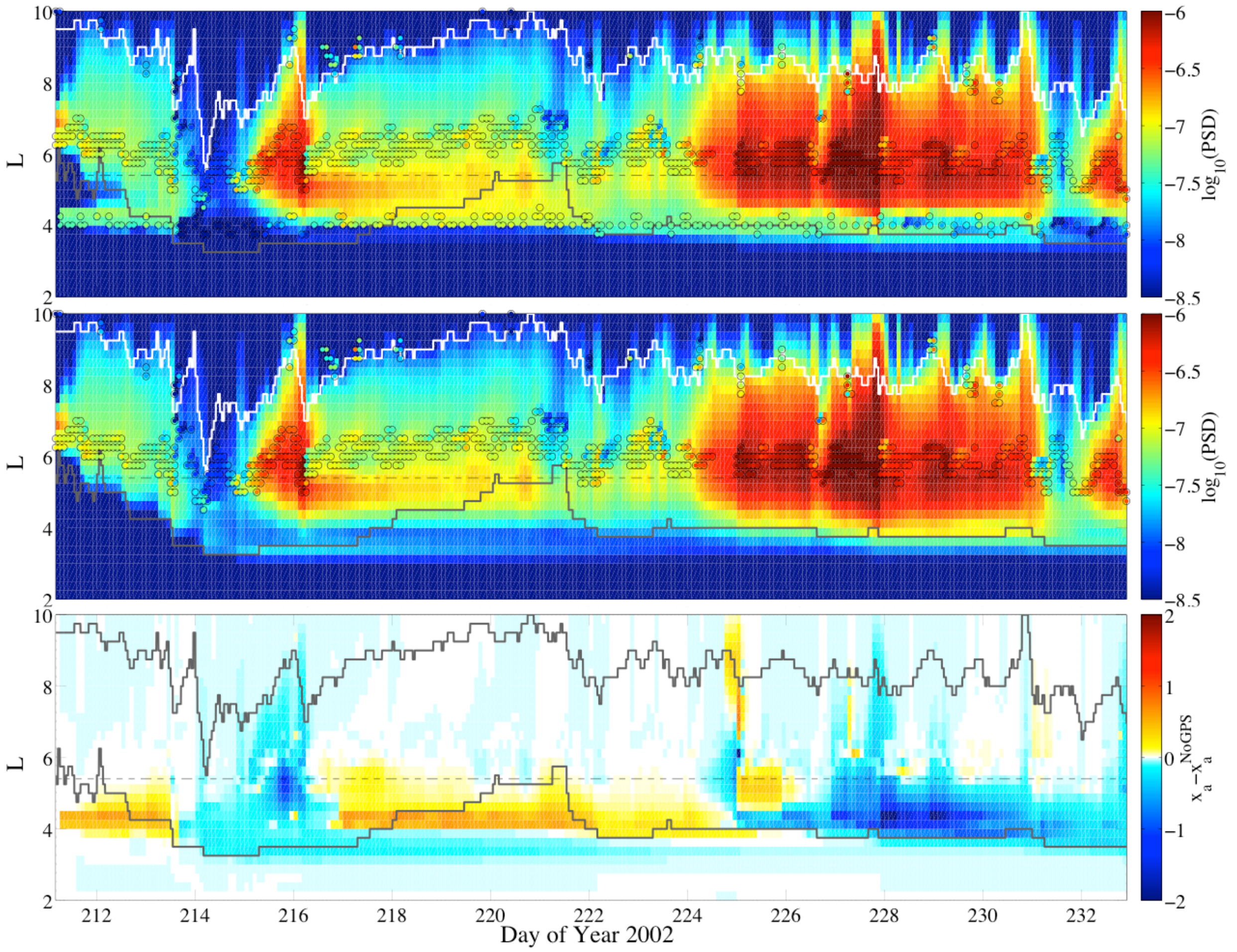

Figure 14: Top panel: Reanalysis with observations from all five spacecraft. Middle panel: Reanalysis performed with all observations except GPS. Bottom panel: The log difference between the the two reanalyses. The dashed line corresponds to the location of the estimatable source term.

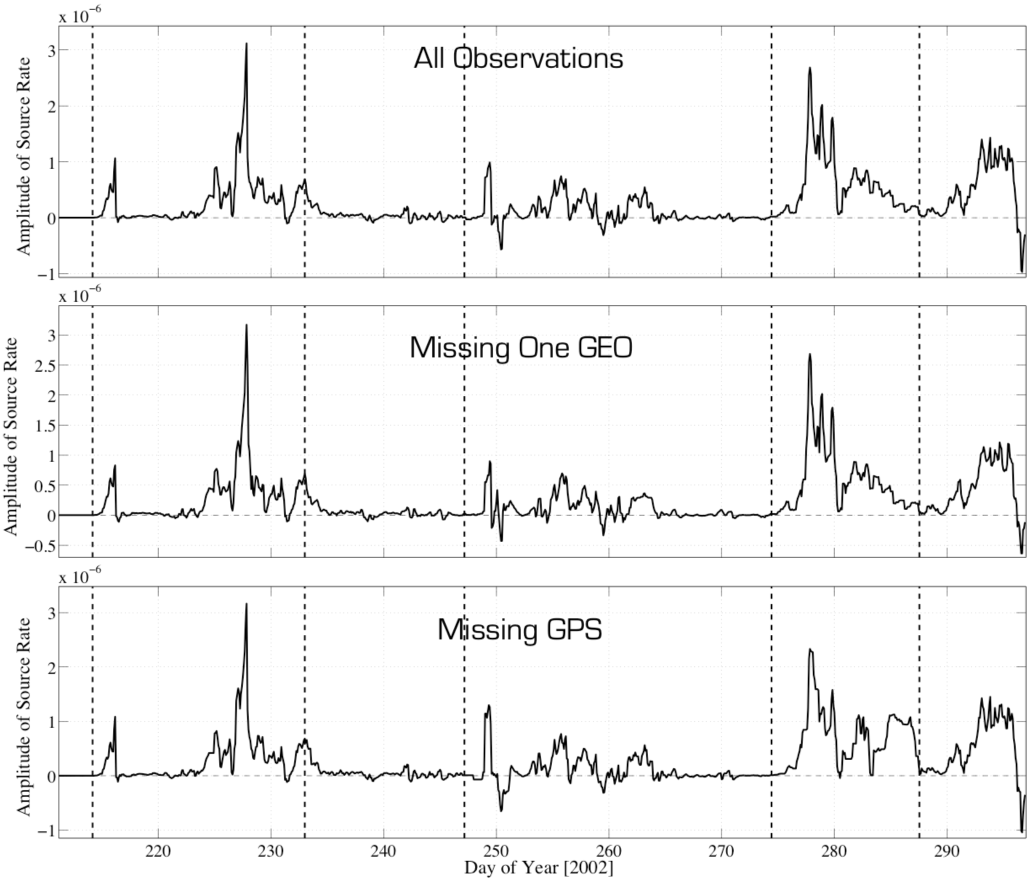

Figure 15: The estimate of the amplitude parameter for reanalysis performed with observations from all five spacecraft (top panel), all spacecraft except for one LANL-GEO (97A - middle panel), and all spacecraft except for GPS (bottom panel). The dashed line corresponds to the location of the estimatable source term.

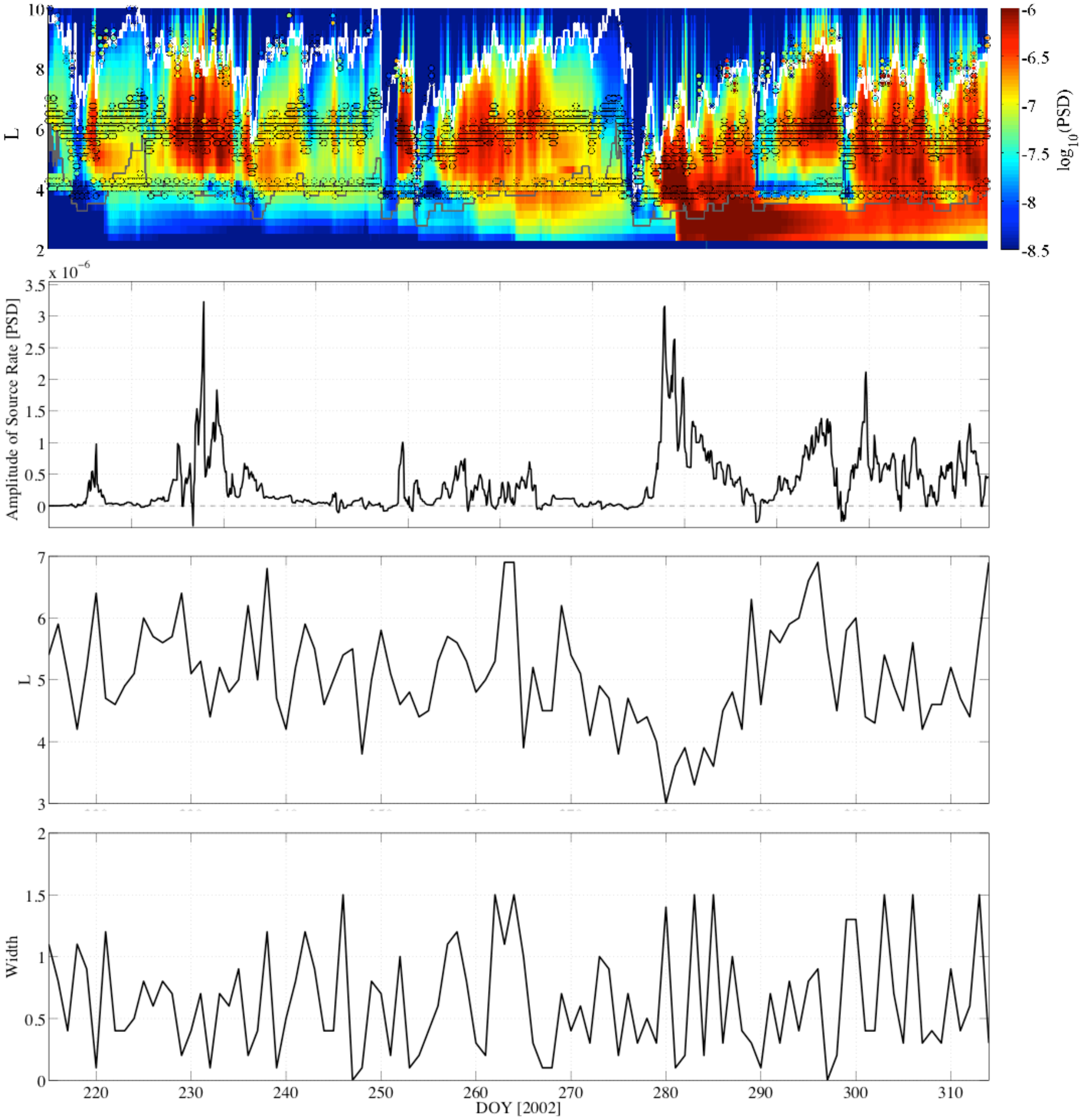

Figure 16: The results of the reanalysis and parametric study on actual observations, as depicted in Figure 12. The top panel shows the PSD estimate with observations overlain, with source term included with parameters from the following panels.. The second panel shows the estimate of the source rate amplitude given the locations and widths described in the following panels. The PSD and amplitude estimates have temporal resolution of 120 minutes, as they are 'online' estimate directly from the state vector. The third panel depicts the location parameter of the source term. The last panel represents the width parameter of the source term. The width/location combination was derived from the parametric study as described in Section 3 and performed in Section 4.

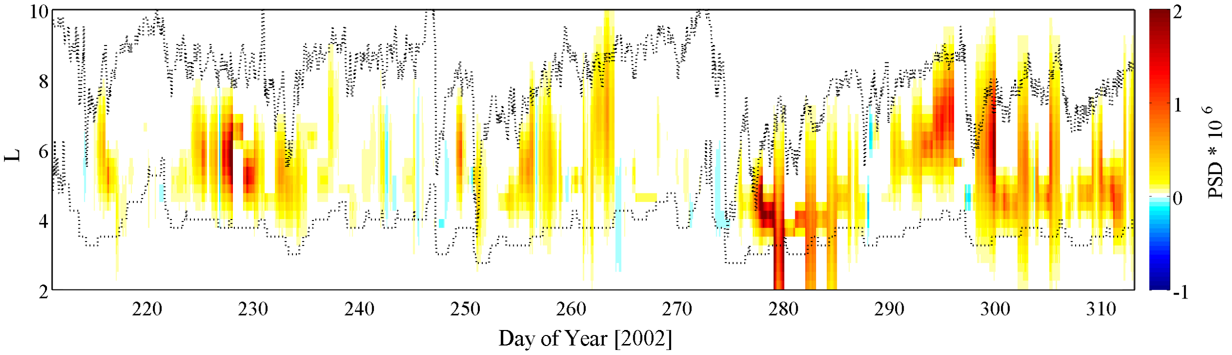

Figure 17: A visualization of the total source rate term, including location, width, and magnitude (color).

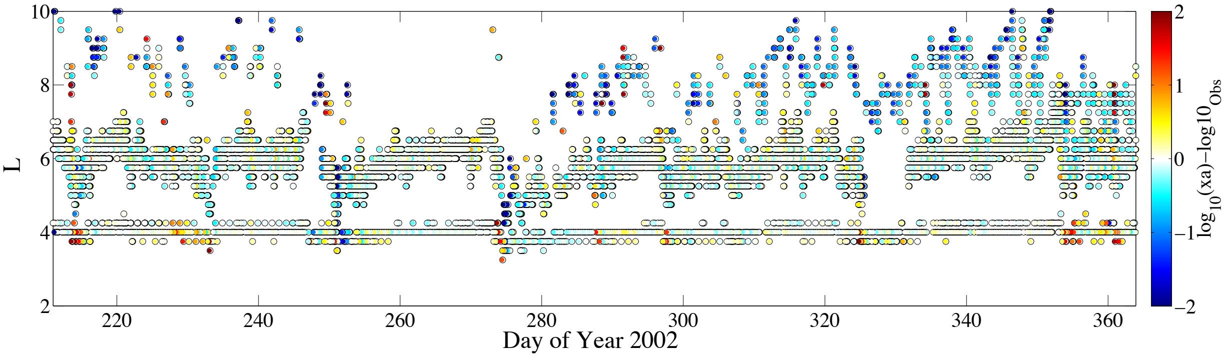

Figure 18: The differences between the log of the estimated PSD and observed PDS at each observation. White indicates a very good match, intense cooler colors an underprediction by the model, and intense warmer colors an overprediction by the model.

5.4. Attempt to Find Correlation Between Source Location and Plasmapause

Whistler mode chorus waves, for example, are believed to be a major contributor in accelerating lower energy electrons to relativistic levels [e.g. Horne et al., 2007 (13)]. These waves are also believed to occur just outside the plasmapause(13). Thus, one would expect to see a correlation between the source location (region of high chorus wave activity), and the plasmapause. The daily averaged plasmapause, from the Dst-dependent plasmapause model by O'Brien and Moldwin(23), and the estimated source location for the same period, can be seen in Figure 19 in red and black, respectively. Additionally, we calculate the correlation coefficient between the two. Since there may be some delay between the timing of local enhancements and the plasmapause location, we also calculate the correlation coefficient incorporating up to an 85 day delay. These results can be seen in Figure 20.

As can be seen in the figure, there does not seem to be any correlation, as the correlation coefficient is not higher than 0.4, except for a lag of -70 days where it is only slightly higher than 0.5. (Interestingly, there is a 27-day period to oscillations in the correlation coefficient lag. This was not unexpected, as various solar wind features can have 27-day periods [e.g. CIRs], which directly affect the configuration of the magnetosphere.) The likely reason for no apparent correlation is that we use a daily averaged plasmapause location. The daily averaging washes out any variations which occur on a smaller timescale. These variations can be significant, varying up to L=3 in a matter of hours. Thus, we conclude that the daily resolution at which we are calculating estimates of the source location is too coarse to resolve a plasmapause correlation, which likely happens on a timescale much less than a day.

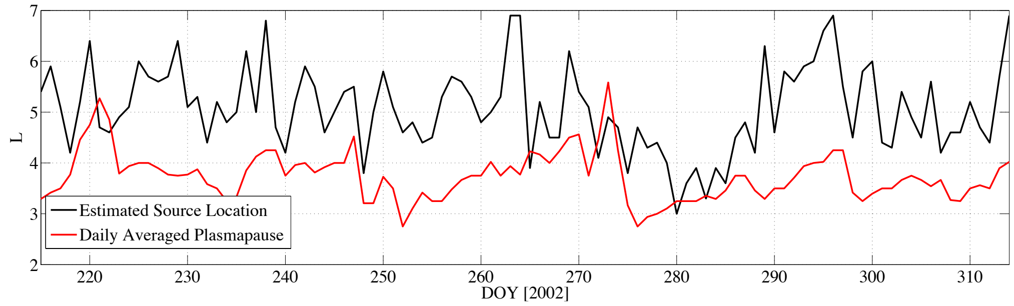

Figure 19: The location of the daily averaged plasmapause location (red) and the estimate of source region location (black).

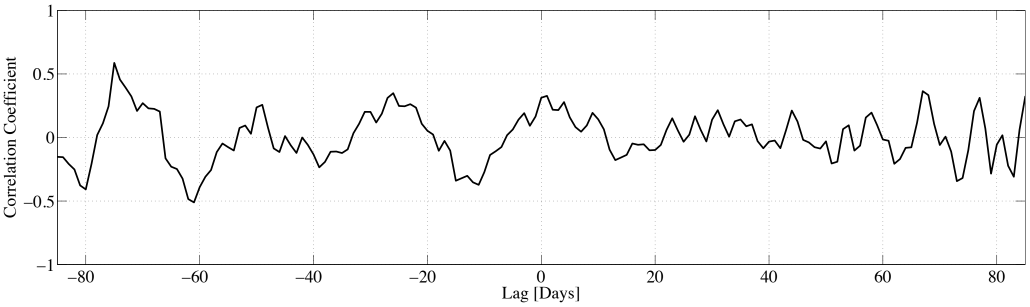

Figure 20: The correlation coefficient between the estimated source location and daily averaged plasmapause location (black and red, respectively, from Figure 19, as a function of lag between the two.

6. Summary and Conclusions

In this paper, we discuss the specifics of estimating source rate parameters in the outer radiation belt electrons using data assimilation. We assume a Gaussian-shaped source region, an assumption which should be improved upon in future studies, and attempt to estimate its radial extent, center location, and intensity.

The state vector of the model consists of the phase space density (PSD) for the full radial range and the amplitude parameter of the source rate term. These variables are estimated 'online', that is, they are direct outputs and have temporal resolution equal to the filter. The remaining source rate parameters, namely the location and width of the source region, are estimated 'offline'. To perform the offline estimation, we employ the innovation vector (or prefit observation residuals) to quantify the performance of the model to reproduce observations for a given location/width pair. We run the model over a large parameter space (often a few hundred runs), and calculate the root mean square (RMS) of the summed innovation vector. The minimum in the RMS parameter space indicates the location/width pair which best predict the observations, and thus are assumed to be the dimensions of the source region.

In the first part of our study, who's purpose is to verify the functionality of our model, we sample a synthesized dataset with a hypothetical spacecraft in an idealized orbit, which are used as the observations (a.k.a. an identical twin experiment). We then measure the performance of the model by quantifying how well the model reproduces the synthesized state. Three experiments are performed, each in increasing complexity. The model performs very well for the first two, accurately reproducing the PSD and the source rate parameters (amplitude, width, and location). The model begins to break down under the conditions imposed for the third experiment, but only when the existing PSD overwhelms the magnitude of the source rate. Overall, the method performs well in estimating PSD and all three dimensions of the Gaussian source term.

In the second part of our study, we apply this technique to actual satellite PSD observations. We first determine that PSD and source rate parameter estimation is relatively robust to the dataset. To do this, we remove one of the satellites from the observations and analyze the results. Since the satellites directly observe PSD, there are significant changes to the PSD estimate when denying a satellite's observations in the reanalysis. However, the estimate of source parameters, namely the intensity of the source region, is robust to which observations are included.

The PSD observations we use are from five satellites: POLAR, one GPS, and three LANL-GEO. We are able to estimate PSD and intensity of local heating at relatively high temporal resolution. We are also able to estimate the location and width of the source region at daily cadence. Using this method, we are able to more accurately predict observed PSD measurements. Unfortunately, we suspect that daily cadence is too coarse to perform any rigorous analysis between the location of the source region and potentially relevant regions in space (e.g. the plasmapause). We do, however, see a 27-day period in the correlation between the plasmapause and the source region, verifying that the solar wind has a strong affect on the plasmapause, the source region, or both.

References

[1] Baker, D. N., "How to Cope with Space Weather," *Science*, Vol. 297, 2002, pp. 1486-1487.

[2] Belian, R. D., G. R. Gisler, T. Gayton, and R. Christensen (1992), High Z energetic particles at geosynchronous orbit during the great solar proton event of October, 1989, *J. Geophys. Res., 97*, 16,897-16,906, doi:10.1029/94JA03066.

[3] Blake, J. B., et al. (1995), Comprehensive energetic particle and pitch angle distribution experiment on POLAR, *Space Sci. Rev., 71*, 531-562, doi:10.1007/BF00751340.

[4] Bourdarie, S., R. H. W. Friedel, J. Fennell, S. Kanekal, and T. E. Cayton (2005), Radiation belt representation of the energetic electron environment: Model and data synthesis using the Salammb radiation belt transport code and Los Alamos geosynchronous and GPS energetic particle data, Space Weather, 3, S04S01, doi:10.1029/2004SW000065.

[5] Bourdarie, S., A. Sicard-Piet, R. H. W. Friedel, T. P. OBrien, T. Cayton, B. Blake, D. Boscher, and D. Lazaro (2009), Outer electron belt specification model, IEEE Trans. Nucl. Sci., 56(4), 22512257, doi:10.1109/ TNS.2009.2014844.

[6] Brautigam, D. H., and J. M. Albert (2000), Radial diffusion analysis of outer radiation belt electrons during the October 9, 1990, magnetic storm, J. Geophys. Res., 105, 291310, doi:10.1029/1999JA900344.

[7] Chen, Y., R. H. W. Friedel, G. D. Reeves, T. G. Onsager, and M. F. Thomsen (2005), Multisatellite determination of the relativistic electron phase space density at geosynchronous orbit: Methodology and results during geomagnetically quiet times, J. Geophys. Res., 110, A10210, doi:10.1029/ 2004JA010895.

[8] Chen, Y., R. H. W. Friedel, and G. D. Reeves (2006), Phase space density distributions of energetic electrons in the outer radiation belt during two Geospace Environment Modeling Inner Magnetosphere/Storms selected storms, J. Geophys. Res., 111, A11S04, doi:10.1029/2006JA011703.

[9] Crank, J., and P. Nicolson (1947), A practical method for numerical evaluation of solutions of partial differential equations of the heat-conduction type, Math. Proc. Cambridge Philos. Soc., 43, 5067, doi:10.1017/ S0305004100023197.

[10] Daae, M., Y. Y. Shprits, B. Ni, J. Koller, D. Kondrashov, and Y. Chen (2011), Reanalysis of radiation belt electron phase space density using various boundary conditions and loss model, Adv. Space Res., 48, 13271334, doi:10.1016/j.asr.2011.07.001.

[11] Feldman, W., W. Aiello, D. Drake, and M. Herrin (1985), the BDD II: An improved electron dosimeter for the Global Positioning System, *LANL Tech. Rep. LA-10453-MS*, Los Alamos Natl. Lab., Los Alamos, N.M.

[12] Hilmer, R., G. Ginet, and T. Cayton (2000), Enhancement of equatorial energetic electron fluxes near L = 4.2 as a result of high speed solar wind streams, J. Geophys. Res., 105, 23,31123,322, doi:10.1029/1999JA000380.

[13] Horne, R. B., R. M. Thorne, S. A. Glauert, N. P. Meredith, D. Pokhotelov, and O. Santolk (2007), Electron acceleration in the Van Allen radiation belts by fast magnetosonic waves, Geophys. Res. Lett., 34, L17107, doi:10.1029/2007GL030267.

[14] Kalman, R. E. (1960), A new approach to linear filtering and prediction problems, J. Basic Eng., 82, 3545, doi:10.1115/1.3662552.

[15] Koller, J., Y. Chen, G. D. Reeves, R. Friedel, T. E. Cayton, and J. A. Vrugt (2007), Identifying the radiation belt source region by data assimilation, J. Geophys. Res., 112, A06244, doi:10.1029/2006JA012196.

[16] Koller, J., and S. K. Morley (2010), Magnetopause shadowing effects for radiation belt models during high-speed solar wind streams, Abstract SM13A-1787 presented at 2010 Fall Meeting, AGU, San Francisco, Calif., 1317 Dec.

[17] Kondrashov, D., Y. Shprits, M. Ghil, and R. Thorne (2007), A Kalman filter technique to estimate relativistic electron lifetimes in the outer radiation belt, J. Geophys. Res., 112, A10227, doi:10.1029/2007JA012583.

[18] Li, X., and M. A. Temerein (2001), The electron radiation belt, *Space Sci. Rev., 95*, 569-580, doi:10.1023/A:1005221108016.

[19] Maget, V., S. Bourdarie, D. Boscher, and R. H. W. Friedel (2007), Data assimilation of LANL satellite data into the Salammb electron code over a complete solar cycle by direct insertion, Space Weather, 5, S10003, doi:10.1029/2007SW000322.

[20] Naehr, S. M., and F. R. Toffoletto (2005), Radiation belt data assimilation with an extended Kalman filter, Space Weather, 3, S06001, doi:10.1029/2004SW000121.

[21] Ni, B., Y. Shprits, T. Nagai, R. Thorne, Y. Chen, D. Kondrashov, and H.-J. Kim (2009a), Reanalyses of the radiation belt electron phase space density using nearly equatorial CRRES and polar-orbiting Akebono satellite observations, J. Geophys. Res., 114, A05208, doi:10.1029/2008JA013933.

[22] Ni, B., Y. Shprits, R. Thorne, R. Friedel, and T. Nagai (2009b), Reanalysis of relativistic radiation belt electron phase space density using multisatellite observations: Sensitivity to empirical magnetic field models, J. Geophys. Res., 114, A12208, doi:10.1029/2009JA014438.

[23] OBrien, T. P., and M. B. Moldwin (2003), Empirical plasmapause models from magnetic indices, Geophys. Res. Lett., 30(4), 1152, doi:10.1029/ 2002GL016007.

[24] Press, W. H., B. P. Flannery, S. A. Teukolsky, and W. T. Vetterling (1986), Numerical RecipesThe Art of Scientific Computing, 1st ed., Cambridge Univ. Press, New York.

[25] Reeves, G. D., Y. Chen, G. S. Cunningham, R. W. H. Friedel, M. G. Henderson, V. K. Jordanova, J. Koller, S. K. Morley, M. F. Thomsen, and S. Zaharia (2012), Dynamic Radiation Environment Assimilation Model: DREAM, Space Weather, 10, S03006, doi:10.1029/ 2011SW000729.

[26] Roederer, J. G. (1970), Dynamics of Geomagnetically Trapped Radiation, Springer, New York, doi:10.1007/978-3-642-49300-3.

[27] Schiller, Q., X. Li, J. Koller, H. Godinez, and D. L. Turner (2012), A parametric study of the source rate for outer radiation belt electrons using a Kalman filter, J. Geophys. Res., 117, A09211, doi:10.1029/2012JA017779.

[28] Shprits, Y. Y., D. Kondrashov, Y. Chen, R. Thorne, M. Ghil, R. Friedel, and G. Reeves (2007), Reanalysis of relativistic radiation belt electron fluxes using CRRES satellite data, a radial diffusion model, and a Kalman filter, J. Geophys. Res., 112, A12216, doi:10.1029/2007JA012579.

[29] Shprits, Y., M. Daae, and B. Ni (2012), Statistical analysis of phase space density buildups and dropouts, J. Geophys. Res., 117, A01219, doi:10.1029/2011JA016939.

[30] Shprits, Y. Y., R. M. Thorne, G. D. Reeves, and R. Friedel (2005), Radial diffusion modeling with empirical lifetimes: Comparison with CRRES observations, Ann. Geophys., 23, 14671471, doi:10.5194/angeo- 23-1467-2005.

Data-driven Modeling of Substorm Growth Phase Magnetic Field

Chao Yue

Department of Atmospheric and Oceanic Sciences, University of California, Los Angeles, CA, USA

Sorin Zaharia

Space Science and Applications, Los Alamos National Laboratory, Los Alamos, NM, USA

Chih-Ping Wang

Department of Atmospheric and Oceanic Sciences, University of California, Los Angeles, CA, USA

Larry Lyons

Department of Atmospheric and Oceanic Sciences, University of California, Los Angeles, CA, USA

Tung-Shin Hsu

Department of Earth and Space Sciences, University of California, Los Angeles, CA, USA

Vassilis Angelopoulos

Department of Earth and Space Sciences, University of California, Los Angeles, CA, USA

Tsugunobu Nagai

Tokyo Institute of Technology, Earth and Planetary Sciences I2-5, Tokyo 152-8551, Japan

Abstract

The plasma and magnetic field structure during the substorm growth phase is crucial to understanding development and initiation of substorms. In this study, we first established empirically the plasma sheet pressure distributions by fitting the Geotail and THEMIS pressure for the growth phase of isolated substorms (at least 240 min from previous onset). Nonlinear least square fitting was achieved with a high correlation coefficient of 0.82. We then computed the 3-D magnetic field in force balance with the fitted pressure. The pressure P shows strong dawn-dusk asymmetry with higher P in the post-midnight sector at $r > 10$ RE, but P becomes higher in the pre-midnight sector inside r ~10 RE. These features are consistent with previous observational studies. The radial pressure gradient along midnight is at least a factor of 2 larger than the previously observed quiet-time gradient for Kp=1. The force-balanced magnetic field lines are more stretched compared with those of quiet-time and of T89 for Kp=3, and are twisted azimuthally toward dawn close to Earth and toward dusk further away from the Earth. The westward tail current peaks near midnight in the tail and the peak moves towards dusk with decreasing radial distance from the Earth inside r ~10 RE. The corresponding field-aligned current (FAC) pattern has region-1 sense FACs in the tail plasma sheet and region-2 FACs closer to the Earth. The region-2 FACs are rotated from their quiet-time picture, upward current dominating the midnight-to dawn MLTs and downward current from dusk to noon MLTs.

Keywords: magnetospheric equilibrium, force balance, substorm growth phase, 3-D magnetic field model

---

Email addresses: `yuechao@atmos.ucla.edu` (Chao Yue), `szaharia@lanl.gov` (Sorin Zaharia), `cat@atmos.ucla.edu` (Chih-Ping Wang), `larry@atmos.ucla.edu` (Larry Lyons), `thsu@igpp.ucla.edu` (Tung-Shin Hsu), `vassilis@ucla.edu` (Vassilis Angelopoulos), `nagai@geo.titech.ac.jp` (Tsugunobu Nagai)

Los Alamos Space Weather Summer School 2012

1. Introduction

The substorm is one of the most interesting and complex phenomena in space physics. It is a process of storage and sudden release of energy in the Earth's magnetosphere. Its development has generally been categorized into three phases: growth, expansion, and recovery. During the growth phase, the auroral oval expands equatorward, the aurora and electrojet gradually intensify, the magnetotail field lines become stretched as the solar wind energy is stored there. The cross-tail current sheet during the growth phase thins and the current is intensified compared to quiet time (e.g., *Sergeev et al.*, 1990, 2011; *Sanny et al.*, 1994). In order to understand the development and initiation of substorms, one needs to know the plasma and magnetic field structure during the substorm growth phase. However current models [either empirical or magnetohydrodynamic (MHD)] are unable to accurately describe the magnetic field during the growth phase. This is because empirical models, such as Tsyganenko 96 magnetic field model (T96) (*Tsyganenko*, 1995; *Tsyganenko and Stern*, 1996), were obtained from statistical averages and work well only for quiet/not too disturbed times. On the other hand, global MHD models, such as the Block Adaptive Tree Solar Wind Roe Upwind Scheme (BATS-R-US) (*Powell et al.*, 1999), have difficulty reproducing realistic magnetospheric configurations during specific events. To solve this problem, a first principle calculation of magnetospheric equilibrium with prescribed initial and boundary conditions can be utilized to study the specific magnetic field configurations during the growth phase as the quasistatic equilibrium is valid then (*Voigt and Wolf*, 1988). In the equilibrium, the magnetic field satisfies (approximate) force balance with plasma pressure. *Cheng* (1995); *Zaharia et al.* (2004); *Zaharia* (2008) solved the 3 dimensional (3D) plasma equilibrium problem by solving the single-fluid force balance equation $J \times B = \nabla \cdot P$ in terms of Euler potentials. Their method is capable of dealing with plasma pressure anisotropy (*Zaharia et al.*, 2004, 2006), thus is especially suitable for calculations in the near-Earth magnetosphere. In this report, we describe initial results of the plasma and magnetic field configurations during the growth phase obtained from the 3-D force balance equilibrium model with a particular pressure choice - namely, the input plasma pressure for the model is a nonlinear data fit of isotropic pressure observed by the Time History of Events and Macroscale Interaction during Substorms (THEMIS) and Geotail probes.

2. Data set and methodology

In this study, we choose isolated substorm events, which are defined here as the time interval between two consecutive substorm onsets being larger than 4 hours. For plasma pressure, we use observations from GEOTAIL (1995-2005) and THEMIS (2007-2010). We first binned the observed pressure near the equatorial plane into a $1R_E$x$1R_E$ grid in the X-Y plane (X from -30 to 15 R_E and Y from -20 to 20 R_E) for substorm growth phase (defined here as the 0-15 min period before a substorm onset). It should be noted that we neglect the pressure anisotropy in the THEMIS data, and only assume the pressure being isotropic. Using the linear correlation between magnetosphere plasma pressure and the solar wind dynamic pressure (P_{dyn}), we then normalized the plasma pressure to the value corresponding to P_{dyn}= 3 nPa. To obtain analytic spatial distributions of the normalized plasma pressure (P_{obs}), we fitted the pressure with a formula with 11 parameters as below: $P_{fit} = e^{b_1 \cdot R}[b_2 + b_3 \cdot \sin\phi + b_4 \cdot (\sin\phi)^2 + b_5 \cdot (\cos\phi)^2] + R^{b_6}[b_7 + b_8 \cdot \sin\phi + b_9 \cdot (\sin\phi)^2 + b_{10} \cdot (\cos\phi)^2] + b_{11}$ By using the nonlinear least square fitting from Matlab's Optimization Toolbox, we obtain b_ι from the minimization of the difference between P_{obs} and P_{fit}. With the fitting pressure as an input to the 3-D equilibrium magnetic field model (*Zaharia et al.*, 2004; *Zaharia*, 2008), we obtained the force balanced magnetic field configuration, as well as the plasma beta and current density. Finally, we compared these quantities to those during quiet time, the Tsyganenko 89 magnetic field model (T89), and observations. Here the quiet time pressure is the empirical Spence-Kivelson pressure (*Spence and Kivelson*, 1993):

$P_{sk} = 89 \cdot e^{-0.59 \cdot |R|} + 8.9 \cdot R^{-1.53}$ where R is the radial distance to the Earth in R_E.

3. Model results and comparison with observations

3.1. *The pressure fitting*

As shown in Figure 1, the observed equatorial pressure is larger at dusk at $R < 8\ R_E$, while the pressure is lower at dusk at $R > 8\ R_E$. Similar asymmetries are found in the fitted model pressure. The asymmetry at $R > 8\ R_E$ is consistent with the pressure profile obtained from low altitude DMSP satellite (*Wing et al.*, 2007). The dawn-dusk pressure asymmetry is likely due to asymmetries in electric and magnetic drifts. The electric drift is not dawn-dusk symmetric. It is stronger in the post midnight sector due to weaker shielding compared with the pre-midnight sector (because electron precipitation and the associated ionosphere conductivity is higher in the post mid-night sector), so all ions are pushed more toward dawn as they drift earthward, resulting in relatively higher pressure in the post-midnight sector. Closer to the Earth, increasing magnetic drift brings higher energy ions toward dusk, causing higher pressure in the pre-midnight sector at smaller radial distance. The model pressure is highly correlated with the observed pressure with a correlation coefficient = 0.82, indicating the model pressure can well represent the observed pressure.

3.2. Comparison of model pressure and computed plasma beta between the growth phase and quiet time

Figure 2 shows that the plasma pressure and pressure gradient decrease with increased radial distance from the Earth. Meanwhile the pressure during the substorm growth phase is larger than during quiet time outside X $\sim$ -7R_E and the pressure gradient is larger beyond $\sim$-12 R_E. Figure 3 shows comparisons between the growth phase equatorial pressure on the left and the quiet time P_{SK} on the right. Note that the empirical P_{SK} only depends on radial distance, therefore the quiet time pressure is dawn-dusk symmetric. Figure 4 shows the 3D force balanced pressure along midnight for the growth phase and quiet time from the equilibrium model. Plasma pressure decreases with the increased distance from the Earth, and is larger in the center plasma sheet than at the lobes at the same radial distance, which is consistent with observations. The plasma beta (β_p) increases with increasing radial distance inside our model domain. Compared with quiet time, the pressure, the pressure gradient, and β_p during the growth phase are larger and the high β_p region ($\beta_p > 1$) is closer to the Earth. Figure 5 shows the comparisons of the equatorial distributions of p between the growth phase and quiet time. Compared with quiet time, the equatorial high β_p region is further earthward and has a maximum value (greater than 100) around X $\sim$ -14 R_E during substorm growth phase.

3.3. Comparison of force balanced magnetic field with observation and T89

As can be seen in Figure 6, during the growth phase the equatorial magnetic field in the tail is much smaller than both the quiet time and T89 field. The left plot of Figure 7 shows that the equatorial magnetic field at midnight during the growth phase is almost the same with T89 model (KP=3) inside X $\sim$ -11 R_E, but is slightly smaller outside X $\sim$ -11R_E. Both the force-balanced and the T89 magnetic fields are similar to the observed field. The right plot of Figure 7 shows the dawn-dusk asymmetry of the force-balanced magnetic field in comparison with the dawn-dusk symmetric T89 field. The dawn-dusk asymmetry in magnetic field is opposite to the pressure dawn dusk asymmetry discussed in Section 3.1, since under force balance the equatorial magnetic field is smaller in the region of higher pressure. Figure 8 shows the 3-D magnetic field lines during substorm growth phase and quiet time. The magnetic field lines near midnight are twisted towards dawn closer to Earth and toward dusk further away from Earth during substorm growth phase. There is no such twist in the quiet time field lines since the quiet time pressure P_{SK} is dawn-dusk symmetric. Figure 9 shows that the force-balanced magnetic field value is similar to observations. There is a B minimum around $\sim$ -17R_E, similar to the T89 model which shows a minimum B at R $\sim$ -15R_E. The existence of a minimum B in the tail plasma sheet has been inferred from observation (*Saito et al.*, 2010, 2011).

3.4. Current density during the growth phase and quiet time

As shown in Figure 10, the azimuthal current is strongly dawn-dusk asymmetric at $R < 10$ R_E with higher current density near dusk, resembling a partial ring current. In the tail, the current density peaks near midnight. The complex current geometry is also seen in data based B-field modeling, e.g., TS07D model (*Tsyganenko and Sitnov*, 2007; *Sitnov et al.*, 2008). During quiet time, the current intensity is much smaller than that during substorm growth phase. Figure 11 shows the azimuthal current at midnight during growth phase and quiet time. During the growth phase, the azimuthal current density is much stronger compared with that of quiet time, and its maximum value in the central plasma sheet is at around X = -10R_E to -15R_E. In addition, the cross-tail current sheet becomes thinner during the growth phase. Figure 12 shows that there are typical region-1 (R1) and region-2 (R2) field-aligned currents (FACs) (*Iijima and Potemra*, 1976) during quiet time, and the intensity of the R1 FACs is much higher than the R2 FACs. During the growth phase, both the R1 and R2 FACs intensify and the FAC system rotates ~90 degree westward. In addition, the FACs move to lower latitude, which is typical during the growth phase.

4. Summary and Future work

The plasma and magnetic field structure during the substorm growth phase is the key to understanding the development of a substorm and triggering of the substorm expansion phase. The magnetic field configuration is particularly important since it is crucial to determining the connection between the processes occurring within the magnetosphere and ionosphere during the substorm. In this study, by using empirical plasma pressure profiles established from THEMIS and GEOTAIL observations during isolated substorm growth phase and a 3-D force balance magnetic field model, we have successfully captured the main characteristics of the magnetic field configuration during substorm growth phase. Important results from the growth phase plasma and magnetic field equilibrium are: (1) The plasma pressure shows strong dawn-dusk asymmetry, which is consistent with low altitude DMSP satellite observations. (2) High correlation coefficient is obtained between observed pressure and fitted model pressure. (3) The computed magnetic field lines are more stretched than both quiet-time and T89. Field lines are also twisted in the azimuthal direction towards dawn closer to the Earth and towards dusk farther away from the Earth. (4) Much stronger cross-tail current and FACs appear compared to those in quiet time. A strong dawn-dusk asymmetry is seen in the partial ring current. The complex geometry of azimuthal current is also seen in the empirical TS07D model. Here, we binned the pressure data according to the substorm growth phase time duration with an assumption that all substorm growth phases have the same time duration. As we know, the strength of the growth phase depends on convection strength, i.e., the cross polar cap potential drop ($\triangle\Phi_{pcp}$). However, binning the data by $\triangle\Phi_{pcp}$ alone is not sufficient for accurately capturing the evolution of the plasma sheet pressure during the growth phase. Because convection strength does determine the rate of energy loading during the growth phase, it does not uniquely specify the state of energy loading, which depends on the time history as well. Therefore, a ”loading parameter” $\int \triangle\Phi_{pcp} dt$ that combines $\triangle\Phi_{pcp}$ with the duration of the IMF being southward is more appropriate. In the next step, we will try to normalize the loading parameter to the same duration of the growth phase. Then we will determine the growth phase 3D equilibrium corresponding to different strengths of this loading parameter.

References

Cheng, C. Z., Three-dimensional magnetospheric equilibrium with isotropic pressure, *Geophysics Research Letters*, *22*, 2401–2404, doi: 10.1029/95GL02308, 1995.

Iijima, T., and T. A. Potemra, Field-aligned currents in the dayside cusp observed by Triad, *Journal of Geophysics Research*, *81*, 5971–5979, doi:10.1029/JA081i034p05971, 1976.

Powell, K. G., P. L. Roe, T. J. Linde, T. I. Gombosi, and D. L. de Zeeuw, A Solution-Adaptive Upwind Scheme for Ideal Magnetohydrodynamics, *Journal of Computational Physics*, *154*, 284–309, doi:10.1006/jcph.1999.6299, 1999.

Saito, M. H., L.-N. Hau, C.-C. Hung, Y.-T. Lai, and Y.-C. Chou, Spatial profile of magnetic field in the near-Earth plasma sheet prior to dipolarization by THEMIS: Feature of minimum B, *Geophysics Research Letters*, *37*, L08106, doi:10.1029/2010GL042813, 2010.

Saito, M. H., D. Fairfield, G. Le, L.-N. Hau, V. Angelopoulos, J. P. McFadden, U. Auster, J. W. Bonnell, and D. Larson, Structure, force balance, and evolution of incompressible cross-tail current sheet thinning, *Journal of Geophysical Research (Space Physics)*, *116*, A10217, doi: 10.1029/2011JA016654, 2011.

Sanny, J., R. L. McPherron, C. T. Russell, D. N. Baker, T. I. Pulkkinen, and A. Nishida, Growth-phase thinning of the near-Earth current sheet during the CDAW 6 substorm, *Journal of Geophysics Research*, *99*, 5805–5816, doi:10.1029/93JA03235, 1994.

Sergeev, V., V. Angelopoulos, M. Kubyshkina, E. Donovan, X.-Z. Zhou, A. Runov, H. Singer, J. McFadden, and R. Nakamura, Substorm growth and expansion onset as observed with ideal ground-spacecraft THEMIS coverage, *Journal of Geophysical Research (Space Physics)*, *116*, A00I26, doi:10.1029/2010JA015689, 2011.

Sergeev, V. A., P. Tanskanen, K. Mursula, A. Korth, and R. C. Elphic, Current sheet thickness in the near-earth plasma sheet during substorm growth phase, *Journal of Geophysics Research*, *95*, 3819–3828, doi:10.1029/JA095iA04p03819, 1990.

Sitnov, M. I., N. A. Tsyganenko, A. Y. Ukhorskiy, and P. C. Brandt, Dynamical data-based modeling of the storm-time geomagnetic field with enhanced spatial resolution, *Journal of Geophysical Research (Space Physics)*, *113*, A07218, doi:10.1029/2007JA013003, 2008.

Spence, H. E., and M. G. Kivelson, Contributions of the low-latitude boundary layer to the finite width magnetotail convection model, 1993.

Tsyganenko, N. A., Modeling the Earth’s magnetospheric magnetic field confined within a realistic magnetopause, *Journal of Geophysics Research*, *100*, 5599–5612, doi:10.1029/94JA03193, 1995.

Tsyganenko, N. A., and M. I. Sitnov, Magnetospheric configurations from a high-resolution data-based magnetic field model, *Journal of Geophysical Research (Space Physics)*, *112*, A06225, doi:10.1029/2007JA012260, 2007.

Tsyganenko, N. A., and D. P. Stern, Modeling the global magnetic field of the large-scale Birkeland current system, *J. Geophys. Res.*, *101*, 27,187–27,198, 1996.

Voigt, G.-H., and R. A. Wolf, Quasi-static magnetospheric MHD processes and the ’ground state’ of the magnetosphere, *Reviews of Geophysics*, *26*, 823–843, doi:10.1029/RG026i004p00823, 1988.

Wing, S., J. W. Gjerloev, and J. R. Johnson, Substorm plasma sheet ion pressure profiles, *AGU Fall Meeting Abstracts*, p. B2, 2007.

Zaharia, S., Improved Euler potential method for three-dimensional magnetospheric equilibrium, *Journal of Geophysical Research (Space Physics)*, *113*, A08221, doi:10.1029/2008JA013325, 2008.

Zaharia, S., C. Cheng, and K. Maezawa, 3-D force-balanced magnetospheric configurations, *Annales Geophysicae*, *22*, 251–265, doi: 10.5194/angeo-22-251-2004, 2004.

Zaharia, S., V. K. Jordanova, M. F. Thomsen, and G. D. Reeves, Self-consistent modeling of magnetic fields and plasmas in the inner magnetosphere: Application to a geomagnetic storm, *Journal of Geophysical Research (Space Physics)*, *111*, A11S14, doi:10.1029/2006JA011619, 2006.

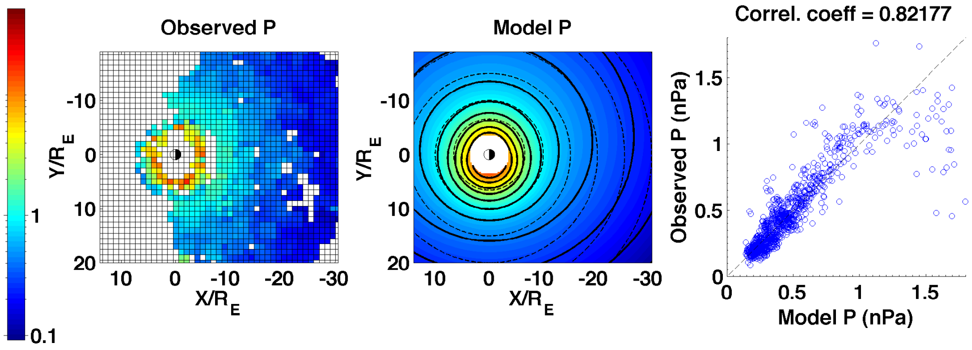

Figure 1: Comparison of observed pressure with model pressure.

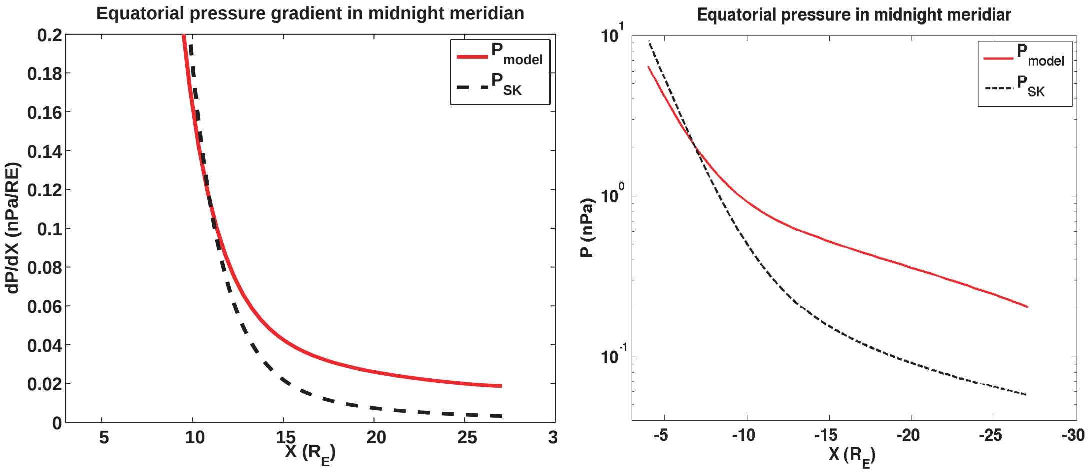

Figure 2: Comparison of midnight meridian pressure and pressure gradient at the equatorial plane.

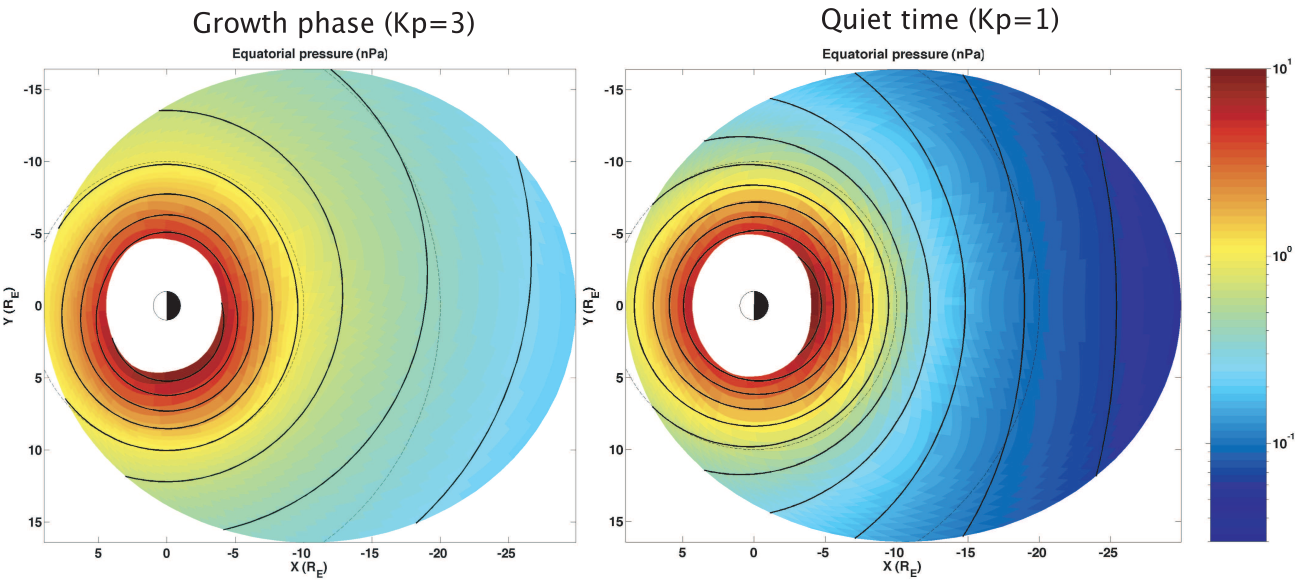

Figure 3: Comparison of pressure at the equatorial plane.

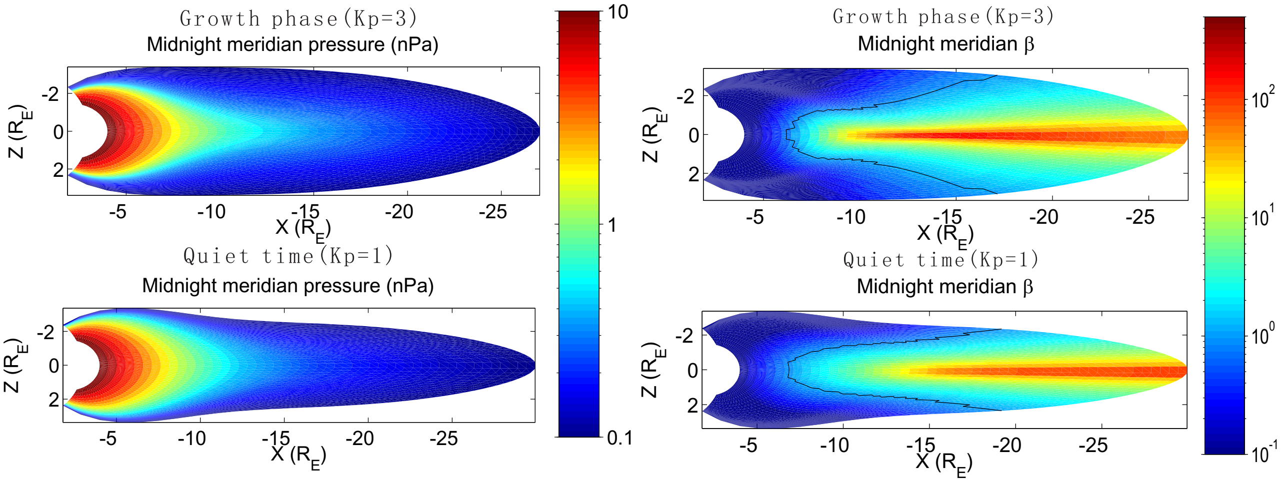

Growth phase (Kp=3)

Midnight meridian pressure (nPa)

Quiet time (Kp=1)

Midnight meridian pressure (nPa)

Growth phase (Kp=3)

Midnight meridian β

Quiet time (Kp=1)

Midnight meridian β

Figure 4: Comparison of pressure and plasma beta at midnight meridian during growth phase and quiet time. The black lines indicate the plasma $\beta_p = 1$.

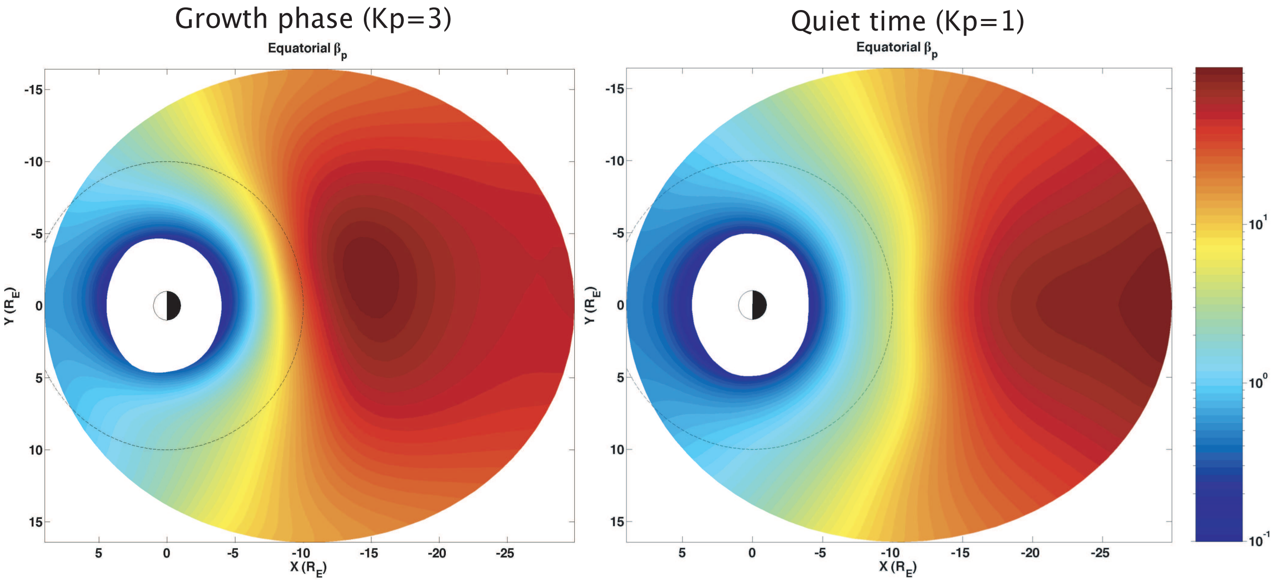

Figure 5: Comparison of plasma beta at equatorial plane during growth phase and quiet time.

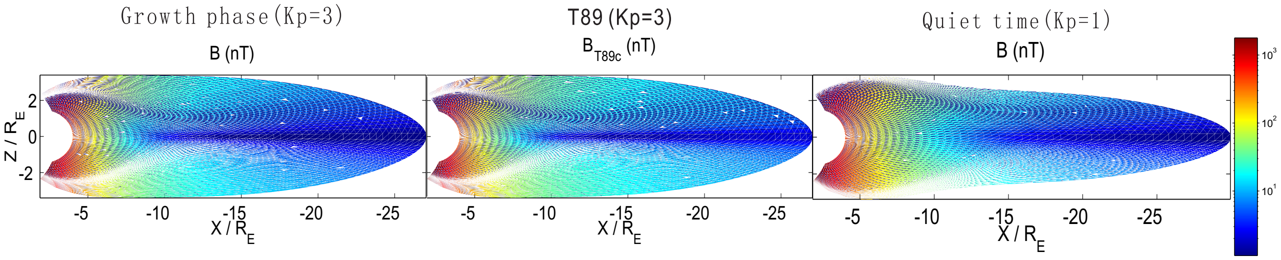

Figure 6: Comparison of B at midnight meridian between quiet time, growth phase, and T89.

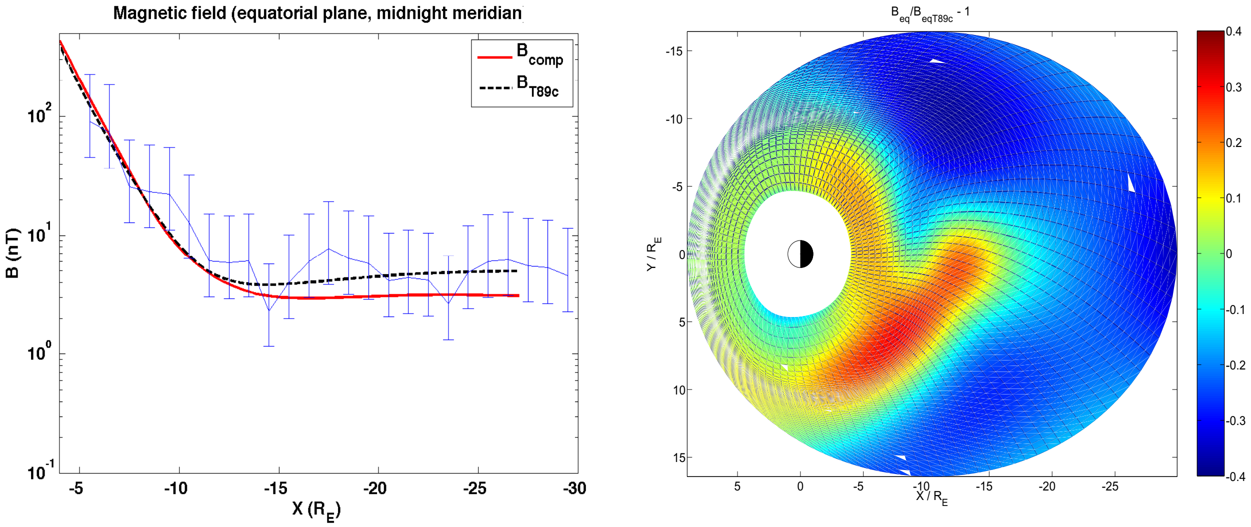

Figure 7: Comparison of growth phase B with observation and T89.

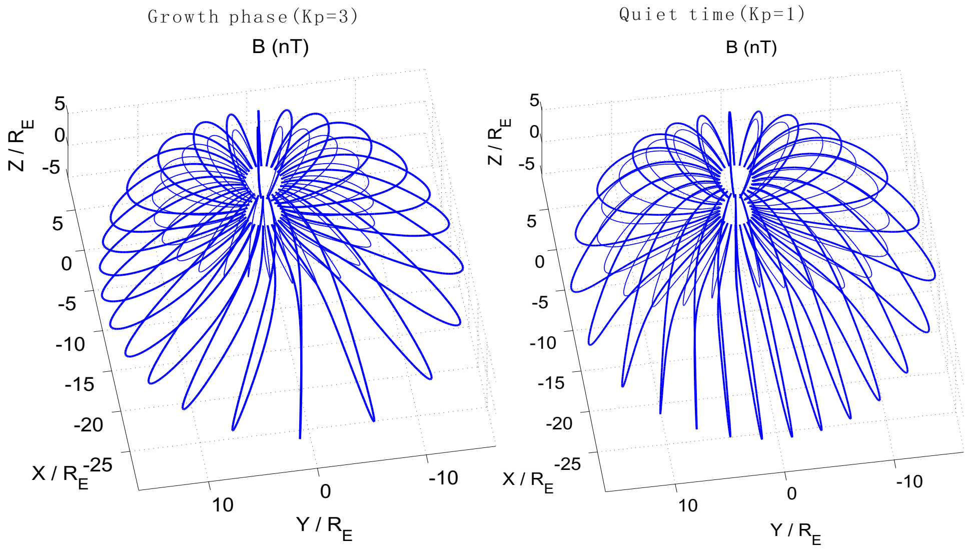

Figure 8: 3-D view of magnetic field lines during growth phase and quiet time.

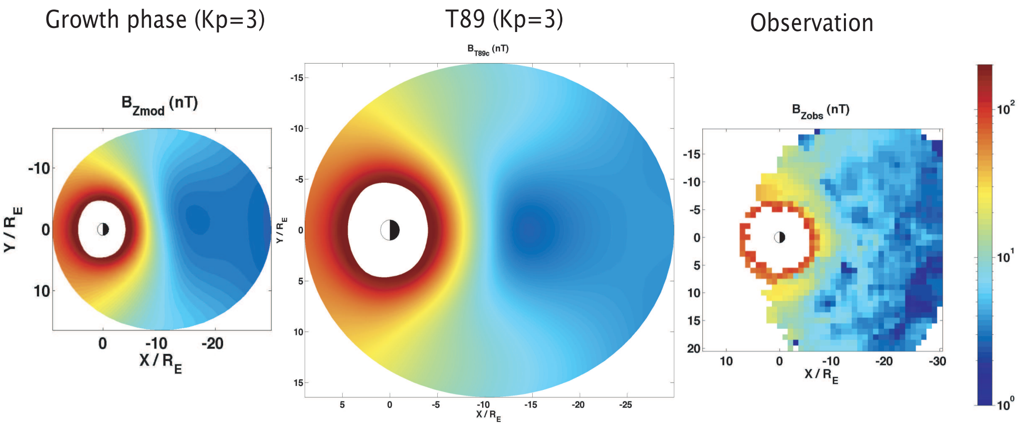

Figure 9: Comparison of B at equatorial plane with T89 and observation.

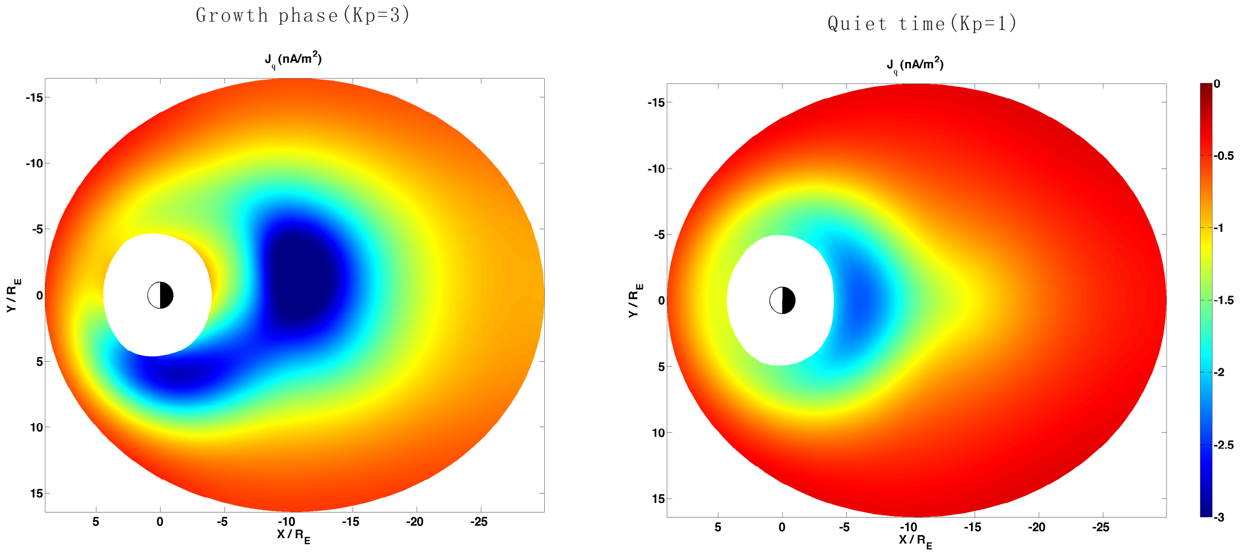

Figure 10: Comparison of azimuthal current in equatorial plane between growth phase and quiet time.

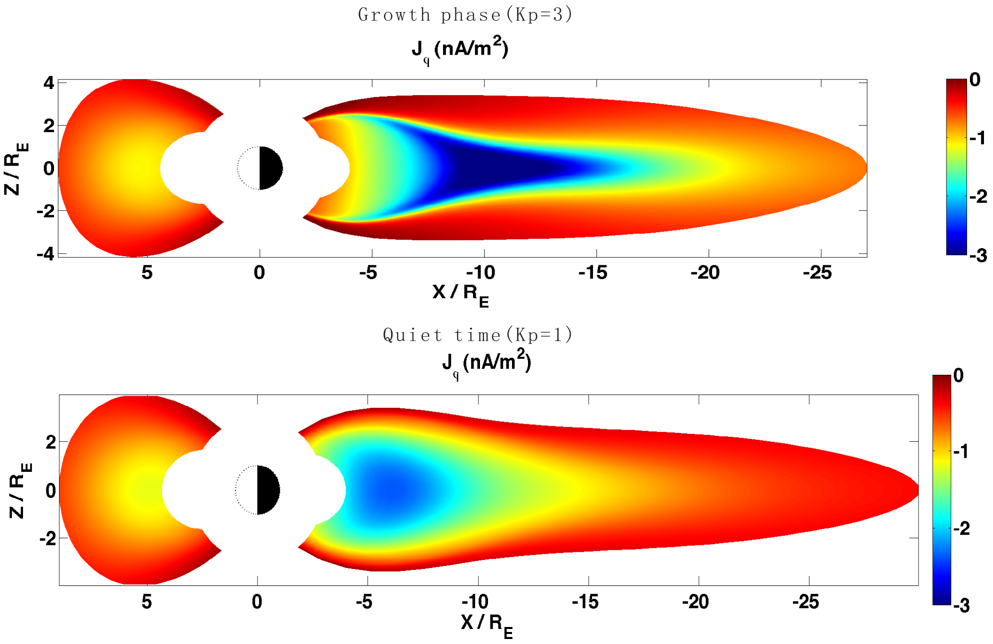

Figure 11: Comparison of azimuthal current at midnight between growth phase and quiet time.

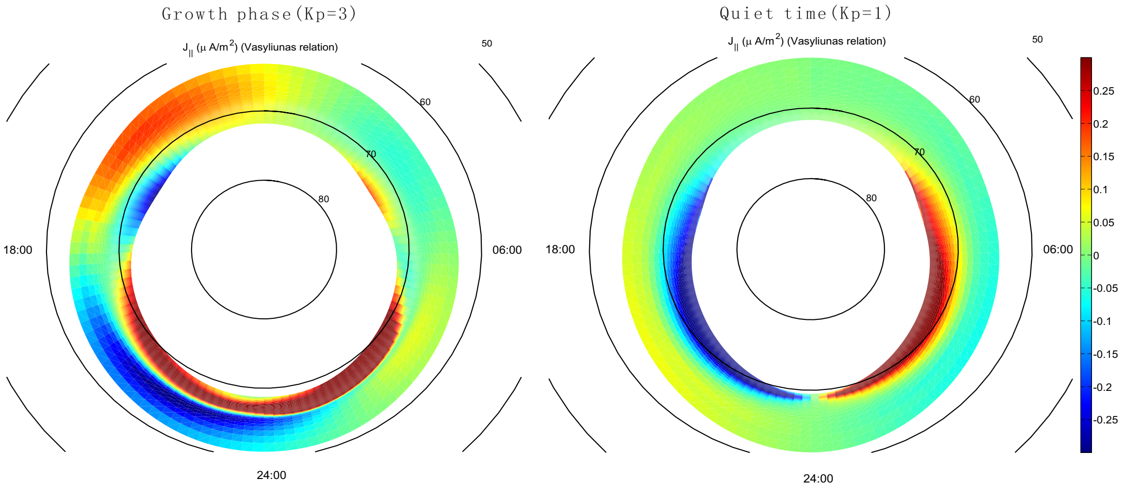

Figure 12: Comparison of field aligned current between the growth phase and quiet time.

LOS ALAMOS
SPACE WEATHER
SUMMER SCHOOL

Los Alamos
NATIONAL LABORATORY
EST. 1943

Los Alamos Space Weather Summer School
30 Bikini Atoll Rd, ISR-1, MS D466
Los Alamos, NM 87545

http://SpaceWeatherSchool.org

ISBN 978-0-9850208-2-8
90000 >
9 780985 020828